The 450 Day X-Ray Monitoring of the Changing-look AGN 1ES 1927+654

C. Ricci[1,2] , M. Loewenstein[3,4], E. Kara[5], R. Remillard[5] , B. Trakhtenbrot[6] , I. Arcavi[6,7] , K. C. Gendreau[3] ,
Z. Arzoumanian[3], A. C. Fabian[8] , R. Li[2], L. C. Ho[2,9] , C. L. MacLeod[10], E. Cackett[11] , D. Altamirano[12] , P. Gandhi[12] ,
P. Kosec[5,8], D. Pasham[5], J. Steiner[5] , and C.-H. Chan[6,13]

[1] Núcleo de Astronomía de la Facultad de Ingeniería, Universidad Diego Portales, Av. Ejército Libertador 441, Santiago, Chile; claudio.ricci@mail.udp.cl
[2] Kavli Institute for Astronomy and Astrophysics, Peking University, Beijing 100871, People's Republic of China
[3] Astrophysics Science Division, NASA Goddard Space Flight Center, 8800 Greenbelt Road, Greenbelt, MD 20771, USA
[4] Department of Astronomy, University of Maryland, College Park, MD 20742, USA
[5] MIT Kavli Institute for Astrophysics and Space Research, 70 Vassar Street, Cambridge, MA 02139, USA
[6] School of Physics and Astronomy, Tel Aviv University, Tel Aviv 69978, Israel
[7] CIFAR Azrieli Global Scholars program, CIFAR, Toronto, Canada
[8] Institute of Astronomy, University of Cambridge, Madingley Road, Cambridge CB3 0HA, UK
[9] Department of Astronomy, School of Physics, Peking University, Beijing 100871, People's Republic of China
[10] Center for Astrophysics, Harvard & Smithsonian, 60 Garden Street, Cambridge, MA 02138-1516, USA
[11] Department of Physics & Astronomy, Wayne State University, 666 West Hancock Street, Detroit, MI 48201, USA
[12] Department of Physics & Astronomy, University of Southampton, Southampton, Hampshire S017 1BJ, UK
[13] Racah Institute of Physics, Hebrew University of Jerusalem, Jerusalem 91904, Israel

Abstract

1ES 1927+654 is a nearby active galactic nucleus (AGN) that underwent a changing-look event in early 2018, developing prominent broad Balmer lines that were absent in previous observations. We have followed up this object in the X-rays with an ongoing campaign that started in 2018 May and that includes 265 NICER (for a total of 678 ks) and 14 Swift/XRT (26 ks) observations, as well as three simultaneous XMM-Newton/NuSTAR (158/169 ks) exposures. In the X-rays, 1ES 1927+654 shows a behavior unlike any previously known AGN. The source is extremely variable both in spectral shape and flux and does not show any correlation between X-ray and UV flux on timescales of hours or weeks/months. After the outburst, the power-law component almost completely disappeared, and the source showed an extremely soft continuum dominated by a blackbody component. The temperature of the blackbody increases with the luminosity, going from $kT \sim 80$ eV (for a 0.3–2 keV luminosity of $L_{0.3-2} \sim 10^{41.5}$ erg s^{-1}) to ~ 200 eV (for $L_{0.3-2} \sim 10^{44}$ erg s^{-1}). The spectra show evidence of ionized outflows and of a prominent feature at ~ 1 keV, which can be reproduced by a broad emission line. The unique characteristics of 1ES 1927+654 in the X-ray band suggest that it belongs to a new type of changing-look AGN. Future X-ray surveys might detect several more objects with similar properties.

Unified Astronomy Thesaurus concepts: Astrophysical black holes (98); X-ray quasars (1821); Active galactic nuclei (16); Supermassive black holes (1663)

Supporting material: figure set, machine-readable table

1. Introduction

Accretion onto supermassive black holes (SMBHs) is thought to play an important role in the evolution of galaxies (e.g., Kormendy & Ho 2013) and to be the mechanism allowing the SMBHs we observe in most massive galaxies (e.g., Magorrian et al. 1998) to reach masses of $M_{BH} \sim 10^6$–$10^{10} M_\odot$. While most active galactic nuclei (AGNs) in the local universe accrete at low values of the Eddington ratio[14] ($\lambda_{Edd} \lesssim 0.3$, e.g., Koss et al. 2017), periods of very rapid accretion, possibly super-Eddington, are expected to be extremely important to explain the growth of the first SMBHs (e.g., Trakhtenbrot et al. 2011; Volonteri 2012), and the vast majority of massive black holes might in fact gain most of their mass through these episodes (King 2003).

Several aspects of the accretion process are still highly debated, such as, for example, the main mechanisms triggering accretion, and why some galaxies host an AGN while others do not (e.g., Alexander & Hickox 2012). Moreover, some AGNs have been

found to show very strong variability (e.g., Rumbaugh et al. 2018; Trakhtenbrot et al. 2019b; Timlin et al. 2020), which could be associated with changes in the inflow of matter or with instabilities of the accretion disk (e.g., Kawaguchi et al. 1998). AGN variability in the optical/UV and X-rays has been directly observed over a very wide range of timescales (e.g., Sartori et al. 2018), ranging from minutes and hours (e.g., McHardy et al. 2014) up to several years (e.g., MacLeod et al. 2010). One of the most interesting aspects of this strongly variable behavior is associated with the so-called changing-look AGN. These are sources in which the optical/UV broad emission lines, produced in the broad-line region (BLR), appear or disappear (e.g., LaMassa et al. 2015; Ruan et al. 2016; Lawrence 2018). These objects are different from the X-ray changing-look AGN, which display strong variation of the line-of-sight column density (N_H, e.g., Risaliti et al. 2009; Bianchi et al. 2012a; Marinucci et al. 2016; Ricci et al. 2016), possibly related to moving clouds in the BLR (e.g., Maiolino et al. 2010) or in the torus (e.g., Markowitz et al. 2014; Buchner et al. 2019).

So far, about 20–30 changing-look AGNs have been discovered (e.g., McElroy et al. 2016; Parker et al. 2016; Krumpe et al. 2017; Yang et al. 2018; Guo et al. 2019, 2020;

---

[14] $\lambda_{Edd} = L\sigma_T/4\pi GM_{BH}m_p c$, where L is the source bolometric luminosity, σ_T is the Thomson cross section, G is the gravitational constant, m_p is the proton mass, and c is the speed of light.

Katebi et al. 2019; MacLeod et al. 2019; Oknyansky et al. 2019), but the physical mechanism behind these events is still poorly understood. Optical changing-look AGNs cannot be explained by variable obscuration, because the BLR is too large to be obscured by the clouds of the dusty torus, except maybe for a narrow range of inclination angles. Moreover, these objects do not typically show any sign of obscuration in their X-ray spectra after transitioning from Type 1 to Type 2 (e.g., Denney et al. 2014). It has been argued that the appearance (disappearance) of the broad lines could be due to an increase (decrease) of the accretion rate (e.g., Elitzur et al. 2014), possibly related to instabilities in the accretion flow (e.g., Ross et al. 2018; Stern et al. 2018). In a few objects, it has been proposed that the increase in the AGN luminosity could be due to tidal disruption events (TDEs; e.g., Komossa 2015 and references therein; Merloni et al. 2015).

1ES 1927+654 is the first accreting SMBH that was detected in the act of changing phase (Trakhtenbrot et al. 2019a). This object is a rather well-known nearby ($z = 0.019422$) AGN, showing peculiar characteristics, completely unexpected within the framework of the AGN unification model (e.g., Antonucci 1993; Urry & Padovani 1995; Netzer 2015; Ramos Almeida & Ricci 2017; Hickox & Alexander 2018). While its optical spectrum suggested a Type 2 classification (Bauer et al. 2000), in the X-rays the AGN appears completely unobscured (i.e., $N_H \simeq 10^{20}$ cm^{-2}; Boller et al. 2003b; Gallo et al. 2013), making it a member of the true Type 2 class (e.g., Panessa & Bassani 2002; Brightman & Nandra 2008; Shi et al. 2010; Bianchi et al. 2012b). Consistent with this idea, Tran et al. (2011) did not find any evidence of hidden polarized broad Hα or direct broad Paβ and Brγ lines. 1ES 1927+654 was found to have increased its flux by at least two magnitudes in the optical V band in 2018 March (AT 2018zf/ASASSN-18el, Nicholls et al. 2018; Stanek 2018) by the All-Sky Automated Survey for Supernovae (ASAS-SN; Shappee et al. 2014). From the analysis of data obtained by the Asteroid Terrestrial-impact Last Alert System (ATLAS; Tonry et al. 2018), Trakhtenbrot et al. (2019a) found that the event started on 2017 December 23. Our optical spectroscopic follow-up campaign showed the appearance of strong broad Balmer emission lines a few months after the optical flux increase (Trakhtenbrot et al. 2019a). This implies that 1ES1927+654 underwent a changing-look phase, in which the circumnuclear gas reacted to the strong increase of the optical/UV flux, illuminating the broad-line region, and creating the broad lines.

Our ongoing X-ray monitoring campaign started in 2018 May, after the detection of broad optical lines, and consists of three joint XMM-Newton/NuSTAR observations (158/169 ks in total), carried out in June (PI: N. Schartel/C. Ricci), 2018 December (PI: N. Schartel/E. Kara), and on 2019 May (PI: C. Ricci); 14 Swift/XRT observations (PI: I. Arcavi, C. Ricci, 26 ks); and 265 Neutron Star Interior Composition Explorer (NICER) observations (678 ks; see Kara et al. 2018 for a summary of the first set of observations). In the X-rays, the source shows an extremely peculiar behavior, with the X-ray corona, which is typically the source of most of the X-ray radiation in AGNs (Haardt & Maraschi 1991; Merloni & Fabian 2001; Fabian et al. 2009; Kara et al. 2016), disappearing after the optical/UV outburst (Ricci et al. 2020). In this paper, we report the detailed analysis of all X-ray observations carried out in the first ~450 days of our monitoring campaign of this puzzling object, which includes observations for a total exposure time of >1 Ms. The paper is

structured as follows: in Section 2, we describe all the X-ray data sets used and the data reduction procedures adopted. In Sections 3 and 4, we illustrate the X-ray spectral and timing analysis of XMM-Newton/NuSTAR and NICER data, respectively. In Section 5, we discuss our results, while in Section 6, we summarize our findings and present our conclusions. Throughout the paper, we adopt standard cosmological parameters ($H_0 = 70$ km s^{-1} Mpc^{-1}, $\Omega_m = 0.3$, $\Omega_\Lambda = 0.7$). Unless otherwise stated, uncertainties are quoted at the 90% confidence level.

2. X-Ray Observations

A large number of X-ray observations were performed during 2018 and 2019 to monitor 1ES 1927+654 using XMM-Newton, NuSTAR, Swift/XRT, and NICER. The distribution of these observations is shown in Figure 1, while the observation log is reported in Table 1 in Appendix A. These observations show very strong variability, both on timescales of <1 day (~1–2 orders of magnitude) and of months (up to ~4 orders of magnitude; see Figure 1 of Ricci et al. 2020). In the following, we describe the procedure adopted for the data reduction of XMM-Newton (EPIC, RGS, and OM; Section 2.1), NuSTAR (Section 2.2), and NICER (Section 2.3) observations. Given the large numbers of high-quality NICER observations, we did not focus on the short (~2 ks) Swift/XRT observations here, and we report their reduction and spectral analysis in Appendix B.

2.1. XMM-Newton

After the optical/UV outburst, XMM-Newton (Jansen et al. 2001) carried out three pointed observations of 1ES 1927+654: on 2018 June 5 (46 ks), on 2018 December 12 (59 ks), and on 2019 May 6 (52 ks). All observations were performed simultaneously with NuSTAR, and in all of them, the source was clearly detected by the EPIC/PN (Strüder et al. 2001) and MOS (Turner et al. 2001) cameras, as well as by the Reflection Grating Spectrometer (RGS; den Herder et al. 2001) and the optical monitor (OM, Mason et al. 2001). All EPIC/PN observations were carried out in small-window mode, using a thin (2018 June and December) or a thick (2019 May) filter. The June and December EPIC/MOS observations were performed in large-window mode, while the one in 2019 May was done in small-window mode. A thin filter was used for all of the EPIC/MOS exposures. During the 2018 June observation, the 0.3–10 keV EPIC/PN (MOS) net count rate of the source was 4.2 ct s^{-1} (0.72 ct s^{-1}), while during the 2018 December and 2019 May observations, it was significantly higher. In 2018 December, the net count rates were 18.9 ct s^{-1} (1.4 ct s^{-1}), and in 2019 May, they were 14 ct s^{-1} (2.6 ct s^{-1}). The EPIC/PN count rate of the 2019 May observation was lower than that of the 2018 December exposure, although the flux was higher, because of the different filter used. For comparison, during the 2011 observation (see Gallo et al. 2013), the EPIC/PN (thin filter) count rate was 5.2 ct s^{-1}.

The observation data files were reduced using the XMM-Newton Standard Analysis Software version 17.0.0 (Gabriel et al. 2004). The raw PN (MOS) data files were then processed using the EPCHAIN (EMCHAIN) task. The analysis of the background light curves in the 10–12 keV band (EPIC/PN) and above 10 keV (EPIC/MOS) of the 2018 June and 2019 May observations showed that no strong background activity was present in either PN or MOS so that we were able to use the whole exposures. Some background activity was detected
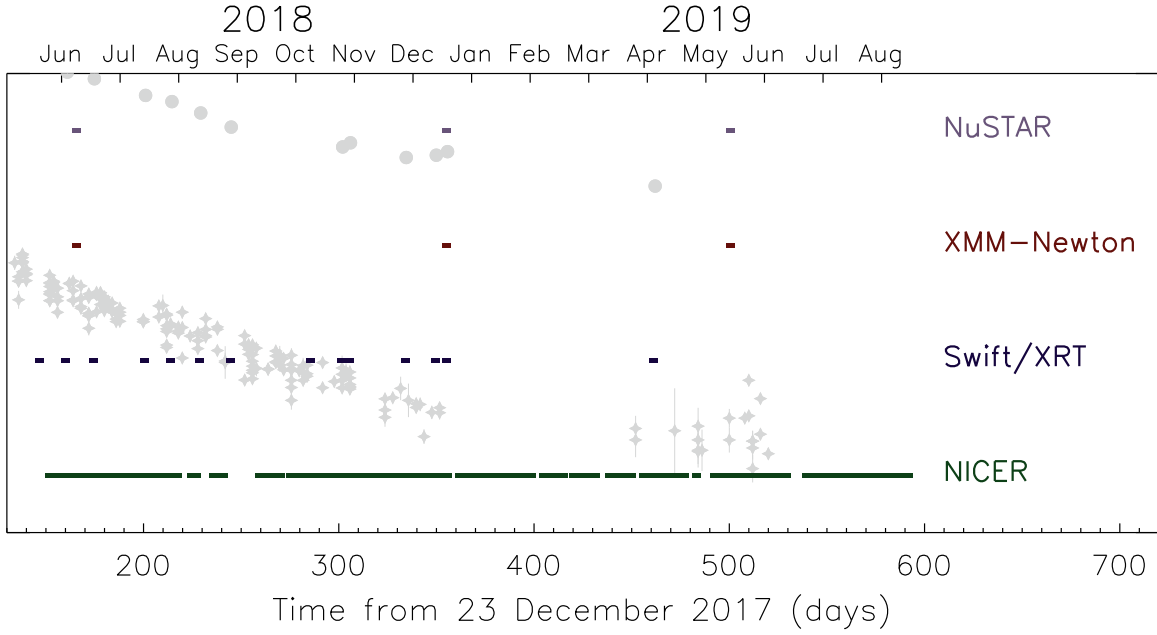
Figure 1. Schematic representation of the X-ray monitoring campaign of 1ES 1927+654 reported here, covering the period between 2018 May 17 and 2019 August 5. The time of the detection here corresponds to that reported by Trakhtenbrot et al. 2019 (2017 December 23), based on observations from the Asteroid Terrestrial-impact Last Alert System (ATLAS; Tonry et al. 2018). The light-gray stars and circles are the ATLAS/o and Swift/UVM2 magnitudes (see Trakhtenbrot et al. 2019a and Ricci et al. 2020). The complete X-ray observation log is reported in Table 1 in Appendix A.

Table 1
Spectral Parameters Obtained for the XMM-Newton 2018 June (Column 2), 2018 December (Column 3), and 2019 May (Column 4) Observations (EPIC+RGS)

	(1)	(2) 2018 Jun	(3) 2018 Dec	(4) 2019 May
(a)	N_H (10^{20} cm^{-2})	⋯	3.0 ± 0.1	$1.8^{+0.06}_{-0.08}$
(b)	N_H^W (10^{20} cm^{-2})	$2.2^{+0.6}_{-0.5}$	$\leqslant 1.1$	$\leqslant 1.1$
(c)	$\log \xi$ (erg cm s^{-1})	$2.9^{+0.1}_{-0.8}$	$1.9^{+0.7}_{-0.4}$	$2.7^{+0.2}_{-1.1}$
(d)	z	$-0.216^{+0.017}_{-0.018}$	$-0.212^{+0.006}_{-0.003}$	$-0.249^{+0.06}_{-0.013}$
(e)	Γ	$1.9^{+0.5}_{-0.7}$	3.02 ± 0.01	$2.98^{+0.08}_{-0.10}$
(f)	E_{cut}	⋯	$2.76^{+0.05}_{-0.04}$	3.3 ± 0.4
(g)	E_1 (keV)	1.01 ± 0.01	1.074 ± 0.005	$1.01^{+0.03}_{-0.05}$
(h)	σ_1 (eV)	103^{+6}_{-7}	156 ± 4	193^{+15}_{-25}
(i)	EW$_1$ (eV)	184^{+10}_{-7}	94^{+23}_{-22}	79^{+30}_{-20}
(j)	E_2 (keV)	1.73 ± 0.04	$1.92^{+0.05}_{-0.06}$	$1.95^{+0.05}_{-0.06}$
(k)	σ_2 (eV)	150^{+70}_{-50}	261^{+56}_{-46}	300^{+NC}_{-52}
(l)	EW$_2$ (eV)	460^{+228}_{-142}	78^{+18}_{-20}	149^{+31}_{-44}
(m)	C_{Nu}	⋯	0.78 ± 0.04	$0.79^{+0.04}_{-0.05}$
(n)	C_{MOS}	1.05 ± 0.01	⋯	⋯
(o)	C_{RGS}	0.92 ± 0.01	0.916 ± 0.004	0.921 ± 0.004
(p)	E_{abs1} (keV)	⋯	0.396 ± 0.002	$0.376^{+0.07}_{-0.06}$
(q)	σ_{abs1} (eV)	⋯	$0.2^{+0.2}_{-0.1}$	25^{+7}_{-5}
(r)	Strength (10^{-3})	⋯	$1.4^{+1.7}_{-0.6}$	11 ± 3
(s)	E_{abs2} (keV)	⋯	0.527 ± 0.001	⋯
(t)	σ_{abs2} (eV)	⋯	0.5 ± 0.1	⋯
(u)	Strength (10^{-3})	⋯	$3.0^{+1.0}_{-0.8}$	⋯
(v)	kT (eV)	102 ± 1	142 ± 1	160^{+4}_{-6}
(w)	$F_{0.3-10}$ (10^{-11} erg s^{-1} cm^{-2})	1.0	6.7	7.9
(x)	$L_{0.3-10}$ (erg s^{-1})	8.5×10^{42}	5.7×10^{43}	6.7×10^{43}
(y)	Stat/DOF	2943/2847	4137/3712	3916/3549

Notes. The model used included a blackbody component, a power law, two Gaussian absorption lines and two emission lines, and a neutral and an ionized absorber. The table reports the column density of the neutral absorber (a); the column density (b), ionization parameter (c), and redshift (d) of the ionized absorber; the photon index (e) and cutoff (f) of the power-law component; the energy (g), width (h), and equivalent width (i) of the first Gaussian emission line; the energy (j), width (k), and equivalent width (l) of the second Gaussian line; the cross-calibration constant of the NuSTAR/FPM (m), XMM-Newton MOS (n), and RGS (o) spectra; the energy (p), width (q), and strength (r) of the first Gaussian absorption line; the energy (s), width (t), and strength (u) of the second Gaussian absorption line; the temperature of the blackbody (v); the 0.3–10 keV flux (w) and luminosity (x); and the value of the statistic and the number of degrees of freedom (y).

around the end of the 2018 December observation, with the count rates rising to $\sim 1\,ct\,s^{-1}$ in EPIC/PN. However, due to the very high flux of the source during this observation, we did not filter out this last ~ 6 ks. As a test, we compared the spectral parameters obtained by spectra with and without this period and found them to be in very good agreement. In our data reduction, only patterns that correspond to single and double events (PATTERN $\leqslant 4$) were selected for PN, and patterns corresponding to single, double, triple, and quadruple events were selected for MOS (PATTERN $\leqslant 12$).

For the 2018 June observation, using circular regions centered on the object to extract the source spectrum, we detected pile-up in all EPIC cameras, so that we adopted an annular region with an inner (outer) radius of $6''$ ($40''$) and $5''$ ($30''$), for PN and MOS, respectively. The pile-up was considerably stronger in the 2018 December and 2019 May observations, and even using a large inner radius ($35''$), it was not possible to completely remove its effect on the MOS spectrum. Therefore, for these observations, we used only the PN camera, extracting the spectrum using an inner (outer) radius of $15''$ ($40''$). The background spectra for the different observations were extracted from circular regions with a radius of $50''$ and $60''$ for PN and MOS, respectively. These regions were located on the same CCD as the source, where no other source was present. The ARFs and RMFs were created using the ARFGEN and RMFGEN tasks, respectively. For the 2018 June observation, the source and background spectra of the two MOS cameras, together with the RMF and ARF files, were merged using the ADDASCASPEC task. In the following, we will refer to the combined spectra as the MOS spectrum. The EPIC spectra were binned to have at least 20 counts per bin, and we applied the χ^2 statistic.

NICER observed 1ES 1927+654 for ~ 7 ks during the 2018 December XMM-Newton observation. This allowed us to compare the XMM-Newton and NICER spectra and to look for the presence of any spectral artifacts related to pile-up and/or to X-ray loading in the EPIC/PN spectrum, as the observation was carried out when the source was extremely bright. In Appendix C, we report the results of our analysis, showing that the spectral parameters obtained by fitting the two data sets are consistent (See Figure C1 and Table C1). This allowed us to exclude any significant impact of pile-up and/or to X-ray loading in the EPIC/PN spectrum.

The RGS data were reduced using the RGSPROC task, and we used default source and background extraction regions. The spectra from the two detectors were combined into a single spectrum using the RGSCOMBINE task, for both the first and second order. The RGS first-order count rates were 0.26, 1.6 and $1.9\,ct\,s^{-1}$ for the 2018 June, 2018 December, and 2019 May XMM-Newton observations, respectively. The RGS spectra were binned to have at least 1 count per bin, and we applied Cash statistics (C-stat; Cash 1979; Kaastra 2017).

The OM data were reduced using the standard guidelines. Details will be reported elsewhere (R. Li et al. 2021, in preparation).

2.2. NuSTAR

The Nuclear Spectroscopic Telescope Array (NuSTAR; Harrison et al. 2013) observed 1ES 1927+654 simultaneously with XMM-Newton, with exposures of 46 ks (2018 June), 65 ks (2018 December), and 58 ks (2019 May). NuSTAR data were processed using the NuSTAR Data Analysis Software

NUSTARDAS v1.8.0 within Heasoft v6.24, using the latest calibration files (Madsen et al. 2015). The source was not detected in the 3–24 keV band during the 2018 June observation, and we recovered upper limits on the flux of $F_{3-5} \leqslant 10^{-14}$, $F_{5-10} \leqslant 6.3 \times 10^{-15}$ and $F_{10-24} \leqslant 6.3 \times 10^{-15}\,erg\,s^{-1}\,cm^{-2}$, for the 3–5 keV, 5–10 keV, and 10–24 keV bands, respectively. A clear detection up to 8 keV (11 keV) was obtained in 2018 December (2019 May), when the flux level of the source was considerably higher. Given the strong variability of the source, we tested for differences in the spectral shape and flux of the spectrum obtained from the whole observation and those extracted from a time interval coincident with the XMM-Newton observation. For the 2018 December observation, we did not find any difference in the spectral shape (see Appendix D), so that for our analysis, we considered the spectrum obtained from the whole NuSTAR exposure.

The FPMA and FPMB spectra were extracted using the NUPRODUCTS task, selecting circular regions with a radius of $50''$. The background spectra and light curves were obtained in a similar fashion, using a circular region of $60''$ radius located where no other source was detected. The 3–8 keV net count rate of the source in the 2018 December and 2019 May observations was $2.3 \times 10^{-2}\,ct\,s^{-1}$ and $4 \times 10^{-2}\,ct\,s^{-1}$, respectively. The NuSTAR FPMA/FPMB spectra were merged, as done for the spectra of the two MOS cameras (in Section 3.1). The spectra were binned to have at least 20 counts per bin, and χ^2 statistic was used for the fitting.

2.3. NICER

Our NICER (Gendreau et al. 2012, 2016; Arzoumanian et al. 2014;) observational campaign commenced on 2018 May 22 and is currently still ongoing. We report here on our analysis of data obtained through 2019 August 5 (see Table 1 in Appendix A for the full observation log). The median exposure during this interval was ~ 2 ks, with a maximum of 20.5 ks. The typical observation cadence was once per day, with the time spacing between successive observation sequences varying between 5 hr and 8.7 days. The unfiltered NICER events were first reprocessed to ensure that the 2018 November energy scale update was applied to all NICER observation sequences, and data from NICER focal plane detector modules 14 and 34 that are known to undergo episodes of increased noise were excluded. An ARF tailored to exclude these was utilized in the spectral analysis. Filtered event files were constructed by applying the NICERDAS version 5.0 standard cleaning criteria that excludes times within the NICER-specific definition of the South Atlantic Anomaly, and those with elevations with respect to Earth's limb and bright Earth below their NICERDAS version 5.0 default values.[15] Additional background-related filtering, described below, was also applied.

Although the standard cleaning eliminates much of NICER internal background, spectral analysis requires the modeling of the inevitable residual background. The NICER internal background, due primarily to the presence of optical light at low energy and energetic charged particles at high energy, depends on the orbital parameters and space weather conditions at the time when the observation was conducted and is highly variable both in magnitude and spectral shape. In order to model the background spectrum for each NICER observation

---

sequence, we utilize three background proxies extracted from the unfiltered event list. One of these is the rate of focused background events in an energy band (15–17 keV) where the telescope effective area is effectively negligible (so all events will be due to particle background), and another is the rate of unfocused events identified as having a "ballistic deficit" due to their having originated at the edges of individual detectors. The latter metric considers the same ratio of slow-chain pulse invariant (PI) to fast-chain PI values used to exclude background in standard screening to instead select background events. This rate is tightly correlated with the cutoff rigidity. A two-dimensional library of spectra was constructed, indexed by the values of these two rates, and extracted from the 2.7 Ms of NICER background field accumulated as of 2019 January 28. The background spectra for any time interval are estimated by adopting the library spectrum corresponding to the derived rates of these two proxies, and then rescaling by the ratio of the 15–17 keV rate to the average rate for that library entry to impose a "soft landing" at the edge of the bandpass. The third background proxy accounts for solar light-leak-driven optical light loading noise events and is constructed from the slow-chain count rate in the 0–0.2 keV noise band that is below the NICER nominal energy range for cleaned file events. The library described above is restricted to "nighttime" conditions (noise band rate $<200\,\mathrm{ct\,s^{-1}}$), and an additional library of "daytime" background residuals is constructed from the background fields indexed by noise band rate for rates $>200\,\mathrm{ct\,s^{-1}}$. The residual spectrum for any time interval is estimated by adopting the library daytime residual spectrum corresponding to the derived noised band rate, and then rescaling by the ratio of the 0–0.2 keV rate to the average such rate for that daytime library entry. The resulting residual daytime spectrum is added to the nighttime spectra.

We subdivide the cleaned event file good time intervals into 120 s subexposures, discarding any leftover intervals shorter than 10 s. Rates of the three background proxies are then calculated for each new interval, and daytime and nighttime background spectra identified accordingly. Intervals that have rates that fall outside of the range in the nighttime library are eliminated from the list of time intervals contributing to the source spectra. The final background spectrum for each observation sequence is then the exposure-weighted sum over these subexposures of the matched library spectra, with a background exposure time that is similarly weighted. The highly variable nature of both the source and background is reflected in the fact that the NICER observations include sequences where the source is not significantly detected above the background and those where the 0.3–3 keV signal-to-noise ratio is >1000. The quality of the match between the background spectrum estimated as described above and the total observed spectrum at energies where the background is clearly dominant varies. We eliminate some of the more poorly matched intervals from consideration by excising those where the absolute value of the net 13–15 keV rate is $>0.10\,\mathrm{ct\,s^{-1}}$. Nevertheless, the source and background spectra for each observation sequence must be carefully scrutinized, and the analysis details (number of components, bandpass used) tailored accordingly (Section 4). The final sum of the 265 source spectra exposure times is $\sim$678 ks.

3. XMM-Newton/NuSTAR Observations

In the following, we report the results obtained by the spectral analysis of the 2018 June (Section 3.1), 2018 December, and 2019 May (Section 3.2) joint XMM-Newton/NuSTAR observations of 1ES 1927+654. In Section 3.3. we report on the results obtained by applying partial covering and blurred reflection spectral models. We also discuss the X-ray and UV variability of the source (Section 3.4) and the time-resolved spectroscopy (Section 3.5) of the three observations, as well as the origin of the broad feature at $\sim$1 keV found in all XMM-Newton observations (Section 3.6).

3.1. The 2018 June Observation

Our first joint XMM-Newton/NuSTAR X-ray observations were carried out on 2018 June. The source has an extremely soft continuum, very different from that observed in the previous XMM-Newton observation, carried out in 2011 May, and from typical AGNs. After the event, in fact 1ES 1927+654 showed only a very weak power-law component, which is found to typically dominate the X-ray emission of AGNs (e.g., Mushotzky et al. 1993). Because of its extreme softness, the source was not detected by NuSTAR, and the spectral analysis was carried out using only EPIC and RGS data. We used the EPIC PN (MOS) data in the 0.3–2.8 keV (0.3–4.6 keV) range and RGS data in the 0.35–1.3 keV interval. The spectral analysis was carried out within XSPEC v12.10.0e (Arnaud 1996). In all models, we took into account Galactic absorption at the position of the source ($N_H = 6.87 \times 10^{20}\,\mathrm{cm^{-2}}$; Kalberla et al. 2005) using the TBABS spectral model (Wilms et al. 2000). A multiplicative constant (CONS in XSPEC) was added to all models to take into account any cross-calibration offset between the different instruments.

The EPIC PN and MOS spectra of this observation are shown in Figure 2(A). We started by fitting the X-ray spectrum with a simple blackbody model (CONS×TBABS×ZBB), which resulted in a chi-squared of $\chi^2 = 2483$ for 320 degrees of freedom (DOF), and left very strong residuals around 1 keV and above $\simeq$1.5 keV (see panel B). The addition of a power-law component to the model [CONS×TBABS×(ZBB+ZPO)] improved the fit ($\chi^2 = 1918$ for 318 DOF), still leaving significant residuals (panel C) between 1 and 2 keV. Similarly to what was done by Gallo et al. (2013), we also added a neutral absorber (ZTBABS in XSPEC), possibly associated with gas in the host galaxy, leaving its column density free to vary [CONS×TBABS×ZTBABS×(ZBB+ZPO)], which improved the fit ($\chi^2 = 1813$ for 317 DOF). Applying this model to the RGS spectrum also shows significant residuals (see Figure E1(B) in Appendix E) and in particular an excess around 1 keV (clearly observed also in the second-order spectrum; see the top panels of Figure E3).

To take into account the strong residuals at $\sim$1 keV, we added a Gaussian line, leaving its width and energy free to vary. This greatly improved the fit ($\chi^2 = 405$ for 314 DOF, panel D), leaving only some residuals at $\simeq$1.8 keV and around the absorption lines also observed in the RGS spectrum. We therefore added a second Gaussian, leaving both the energy and the width free to vary in the fit, which yielded a better fit ($\chi^2 = 375$ for 311 DOF). To model the absorption lines resolved in the RGS spectra, we then added a warm absorber using an XSTAR (Bautista & Kallman 2001; Kallman & Bautista 2001) table built for a blackbody with a temperature of $kT = 100$ eV, fixing the turbulent velocity to $v_\mathrm{turb} = 10^4\,\mathrm{km\,s^{-1}}$ [CONS×TBABS×ZTBABS×MTABLE{XSTAR}×(ZBB+ZPO+ZGAUSS+ZGAUSS)]. We left the redshift, ionization parameter and column density of the ionized absorber free to vary
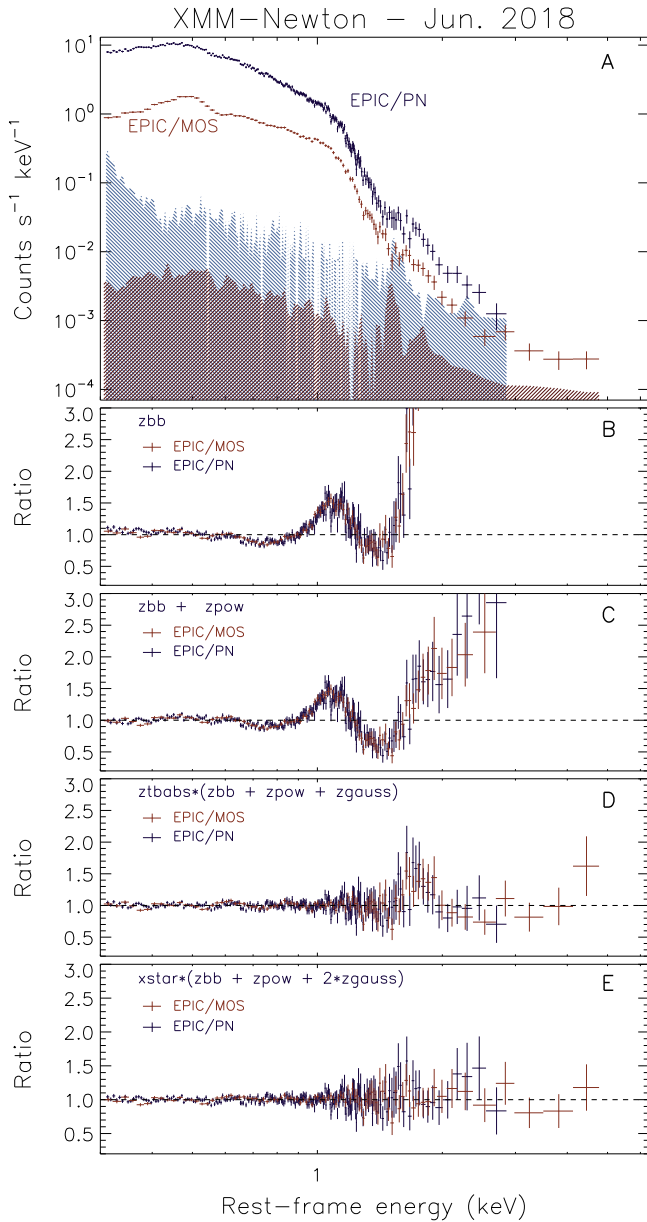
Figure 2. (A) 2018 June XMM-Newton EPIC/PN (blue) and MOS (red) spectra of 1ES 1927+654. The blue and red shaded area represent the background spectra of EPIC/PN and MOS, respectively. (B)–(E) Ratio between models and the data, sorted from the least (B) to most complex (E) model. The different models used include a blackbody component (ZBB), a power-law continuum (ZPO), a neutral absorber (ZTBABS), a ionized absorber (XSTAR), and Gaussian lines (ZGAUSS). More details can be found in Section 3.1.

in the fit. This removed the need of a neutral absorber, which was not constrained by the fit ($N_H \leqslant 2.3 \times 10^{19}$ cm^{-2}), and resulted in a good fit ($\chi^2 = 346$ for 309 DOF, panel (E)). The ionized absorber provides a better fit than a simple neutral absorber, providing a difference in the chi-squared of $\Delta\chi^2 = 29$ for two additional DOF (i.e., ionization parameter and redshift).

We then fitted the EPIC spectra together with RGS, using our best model, which included a blackbody, a power law, two Gaussian lines, and a layer of ionized material. This model can reproduce the data very well (Stat/DOF = 2943/2847, where Stat includes both χ^2 and C-stat; see Figure E1(C) in Appendix E), and resulted in a temperature of the blackbody

component of $kT = 102 \pm 1$ eV and a photon index of $\Gamma = 1.9^{+0.5}_{-0.7}$, consistent with what we found using only EPIC data. The results of this final fit are reported in column 2 of Table 1, while the spectrum and the different components used are illustrated in the top panel of Figure 3. We found that the ionized absorber has a redshift of $z \sim -0.22 \pm 0.02$, which implies a velocity of $v \sim 0.26c$ comparable to those observed in some AGNs (e.g., Tombesi et al. 2010) and ultraluminous X-ray sources (e.g., Pinto et al. 2016; Walton et al. 2016). We also created an absorption model with a lower turbulent velocity ($v_{turb} = 300$ km s^{-1}), considering a blackbody with a temperature of $kT = 100$ eV for the X-ray continuum. We included this model in our fit to the EPIC and RGS spectra, and found that it provides a worse fit (Stat/DOF = 2963/2847) than that obtained by considering an absorber with very large turbulent velocity. While both the column density and ionization parameter were consistent with those obtained assuming $v_{turb} = 10^4$ km s^{-1}, the redshift of the absorber was considerably lower ($z = -0.101 \pm 0.001$).

As a further test, we replaced the XSTAR table with the XSTAR WARMABS model, which is not based on precalculated grids but calculates the spectrum on the fly. We produced specific population files using the observed X-ray spectrum of 1ES 1927+654, rather than a single-component model. Fitting the X-ray spectrum with this model [CONS×TBABS×ZT-BABS×WARMABS× (ZBB+ZPO+ZGAUSS+ZGAUSS)] resulted in a good fit (Stat/DOF = 3021/2846), and values of the temperature of the blackbody ($kT = 102 \pm 1$ eV) and photon index ($\Gamma = 2.0^{+0.5}_{-0.7}$), consistent with what we found applying the XSTAR table. With this approach, we could also get some constraints on the turbulent velocity of the absorber, which was found to be $v_{turb} \geqslant 7418$ km s^{-1}.

We tested different X-ray continuum models to replace the blackbody component, including a multicolor blackbody model and a Comptonized plasma (see Appendix F), and we found that the data appear to be best fitted by the blackbody model.

3.2. The 2018 December and 2019 May Observations

Two additional joint XMM-Newton/NuSTAR observations of the source were carried out on 2018 December and 2019 May (Figure 4(A)). During these observations, the source was $\simeq$7–8 times brighter than in June, and the maximum luminosity was reached during the 2019 May observation. While the spectra were found to be still extremely soft, the emission was significantly harder than in the previous XMM-Newton observation. This, combined with the higher overall flux, allowed NuSTAR to detect the source in both observations. For 2018 December (2019 May), we used the EPIC/PN data in the 0.3–3 keV (0.3–3 keV) range and RGS data in the 0.35–1.85 keV (0.35–1.85 keV) interval; NuSTAR data were used in the 3–8 keV (3–11 keV) range.

We started by applying a model that includes a blackbody plus a power-law component [CONS×TBABS×ZTBABS×(ZBB+ZPO)]. This resulted in a poor fit (χ^2/DOF = 1637/567 and χ^2/DOF = 1340/667 for 2018 December and 2019 May, respectively), with clear residuals in the 1–2 keV region, similarly to what we found studying the 2018 June XMM-Newton observation (see Section 3.1). Moreover, the fit also fails to reproduce the spectrum above 3 keV (Figure 4(B)). Adding a Gaussian line [CONS×TBABS×ZTBABS×(ZBB+ZPO+ZGAUSS)], panel (C), to this model removes the residuals at $\simeq$1 keV, leaving, however, very strong residuals above 3 keV
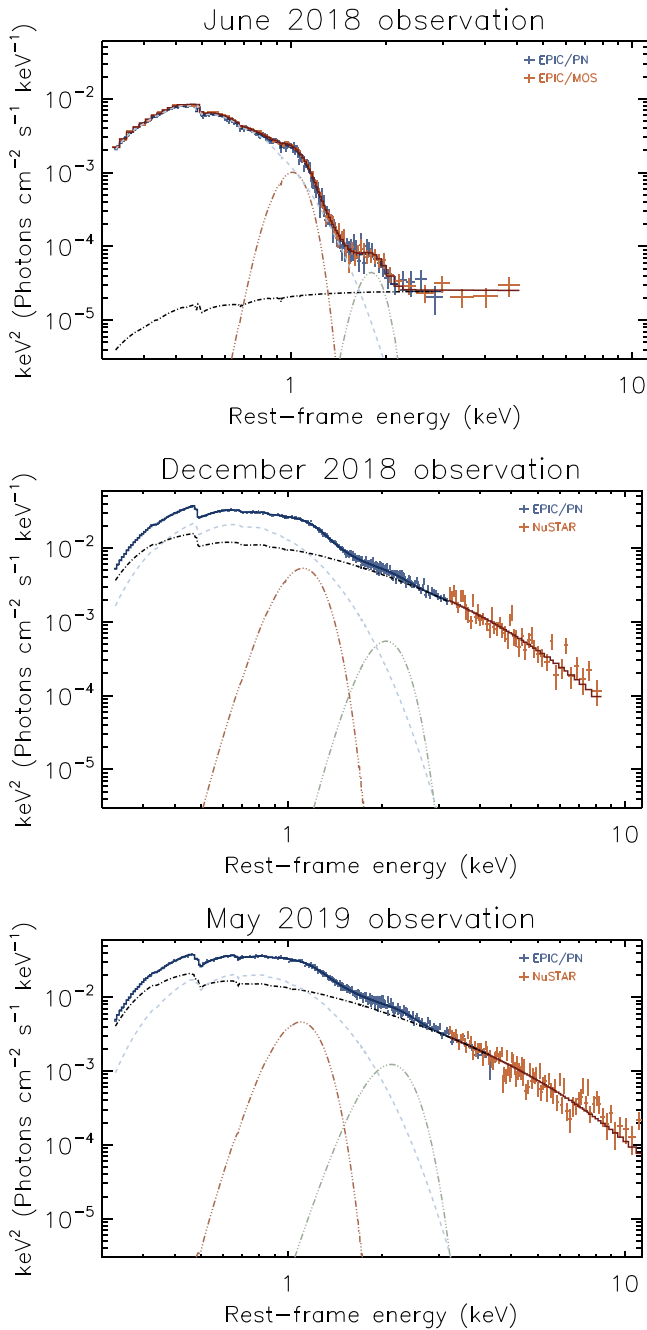
Figure 3. Top panel: 2018 June XMM-Newton EPIC/PN (blue points) and MOS (red points) spectra of 1ES 1927+654. The continuous line shows the best-fitting model, which includes a blackbody (cyan dashed line), a power law (black dotted–dashed line), and two Gaussian lines (dotted–dotted–dashed lines). These components are absorbed by low-column-density neutral and ionized material (see Section 3.1 and column 2 of Table 1 for details). The residuals of this fit are shown in panel E of Figure 2. Middle panel: same as the top panel for the 2018 December XMM-Newton EPIC/PN (blue points) and NuSTAR (red points) observations, using a cutoff power law (black dotted–dashed line). See Section 3.2 and column 3 of Table 1 for details. The residuals of this fit are shown in panel E (left) of Figure 4. Bottom panel: same as the middle panel for the 2019 May XMM-Newton EPIC/PN (blue points) and NuSTAR (red points) observations (see Section 3.2 and column 4 of Table 1 for details). The residuals of this fit are shown in panel E (right) of Figure 4.

($\chi^2/\mathrm{DOF} = 820/564$ and $\chi^2/\mathrm{DOF} = 1079/664$) and a cross-calibration constant for the NuSTAR spectrum that is rather unrealistic ($C_{\mathrm{Nu}} = 0.41 \pm 0.03$ and $C_{\mathrm{Nu}} = 0.53 \pm 0.03$), considering that the observations were carried out simultaneously.

3.2.1. Cutoff Power-law Continuum

Because a power-law continuum cannot reproduce the 3–10 keV region, we used a cutoff power-law model to account for the spectral curvature observed in NuSTAR data [CONS×TBABS×ZTBABS×(ZBB+ZCUT+ZGAUSS)]. This reproduces much better the spectra ($\chi^2/\mathrm{DOF} = 647/563$ and $\chi^2/\mathrm{DOF} = 1040/663$; panel (D)). An ionized absorber appears to be still present, as shown by the RGS spectra (see Figures E1(B) and Figure E2(B) in Appendix E), with absorption features around 0.7–0.8 keV. We therefore used the same XSTAR table adopted for the June observation to take into account this absorber. Some residuals are also evident in the 1.7–2 keV region, consistent with what we found for the 2018 June observation, so that we added also a second Gaussian component, which significantly improved the fit ($\chi^2/\mathrm{DOF} = 621/557$ and $\chi^2/\mathrm{DOF} = 726/657$, panel (E)).

As we did for the 2018 June observation, we used this model to fit the NuSTAR, XMM-Newton EPIC/PN, and RGS data (Stat/DOF = 4363/3718 and Stat/DOF = 3949/3552). The RGS spectrum of the 2018 December observation shows two additional absorption features at ∼0.4 keV and ∼0.53 keV that are not reproduced by the ionized absorber. Only the feature at ∼0.4 keV was found in the 2019 May spectrum. We therefore added two (one) Gaussian absorption lines to the 2018 December (2019 May) spectrum, leaving both the energy and the width free to vary, which improved the fit (Stat/DOF = 4137/3712 and Stat/DOF = 3916/3549; see panel (C) in Figures E1 and E2). The results of this fit are reported in columns 3 and 4 of Table 1, while the spectra and the different components used are illustrated in the middle and bottom panels of Figure 3.

The temperature of the blackbody component is higher in 2018 December (2019 May) than it was in 2018 June ($kT = 142 \pm 1$ eV and $kT = 160^{+4}_{-6}$ eV, respectively). The velocity of the outflow is slightly higher in 2019 May than in the previous two observations. The photon index is consistent in the two observations, and the power-law component is significantly stronger with respect to the blackbody component than in 2018 December.

3.2.2. Thermal Comptonization Continuum

In order to describe the hard X-ray component produced by the corona, which was only weakly detected in the first XMM-Newton observation, we have thus far used a cutoff power law, consistent what is typically done for AGNs (e.g., Dadina 2007; Ricci et al. 2017). However, if the seed photons of the Comptonization process are the soft X-ray photons from the thermal component, this approach might not be physically self-consistent. In order to test this scenario, we used the NTHCOMP model (Zdziarski et al. 1996; Życki et al. 1999), which provides an accurate description of the X-ray continuum arising from thermal Comptonization. The parameters of this model are the temperature of the Comptonizing electrons (kT_{e}), the temperature of the blackbody providing the seed photons (kT_{bb}), the asymptotic power-law photon index (Γ_{nth}), and the normalization. In XSPEC, our model is CONS×TBABS×ZTBABS×M-TABLE{XSTAR} × (ZBB+NTHCOMP+ZGAUSS+ZGAUSS). In our fits of the 2018 December and 2019 May XMM-Newton observations, we substituted NTHCOMP to the cutoff power-law component, fixed the temperature of the seed photons to that of the thermal component ($kT_{\mathrm{bb}} = kT$), and let kT_{e} and Γ_{nth} free to
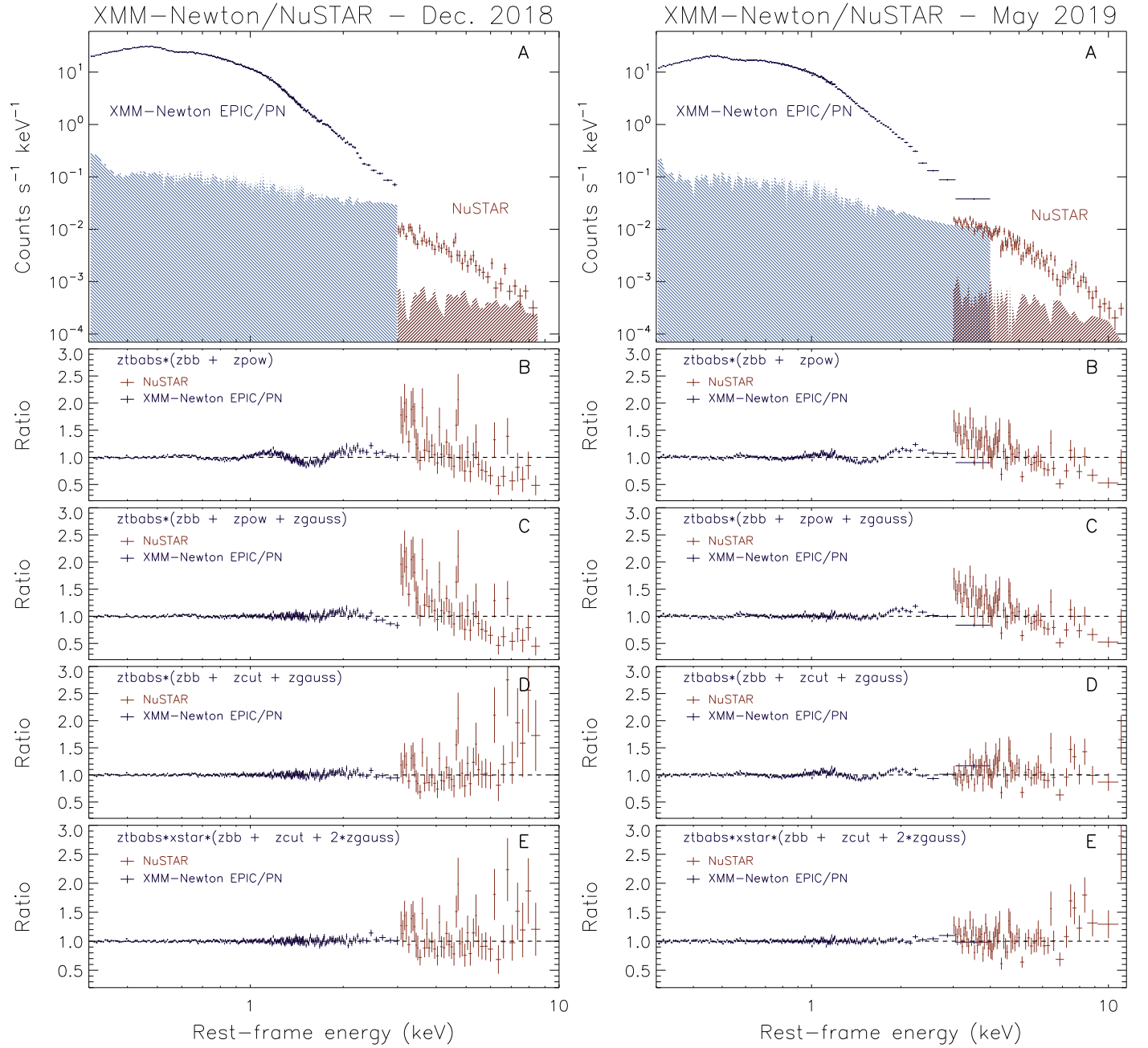
Figure 4. (A) 2018 December (left panels) and 2019 May (right panels) XMM-Newton EPIC/PN (blue) and NuSTAR (red) spectra of 1ES 1927+654. The blue and red shaded area are the background spectra of EPIC/PN and NuSTAR, respectively. (B)–(E) Ratio between the models and the data, sorted from the least (B) to most complex (E) model. The different models used include a blackbody component (ZBB), a power-law continuum (ZPO), a neutral absorber (ZTBABS), ionized absorbers (XSTAR), and Gaussian lines (ZGAUSS). More details can be found in Section 3.2.

vary. In both cases, this model provided a fit worse than (χ^2/DOF = 631.1/557 for the 2018 December observation) or similar ($\chi^2 = 727/657$ for 2019 May) to the cutoff power-law model. Both temperature of the electrons in the Comptonizing plasma and the photon index are higher in the 2019 May observation ($kT_e = 4.4^{+7.3}_{-1.5}$ keV and $\Gamma = 4.4 \pm 0.1$) than in the 2018 December one ($kT_e = 1.8^{+1.0}_{-0.5}$ keV and $\Gamma = 3.7 \pm 0.2$). Interestingly, the blackbody temperature obtained is consistent between the two observations and is significantly lower than when using a cutoff power-law model: $kT = 124 \pm 1$ eV and $kT = 122 \pm 4$ eV for the 2018 December and 2019 May observation, respectively. The temperature is however

significantly higher than in our first XMM-Newton observation ($kT = 102 \pm 1$ eV).

3.3. Comparison with the 2011 XMM-Newton Observation and Alternative Modelling

The 2011 XMM-Newton observation of 1ES 1927+654 was studied in detail by Gallo et al. (2013), who applied several different models, including a power law absorbed by two partial covering neutral or ionized obscurers, as well as blurred ionized reflection. The authors found that all models could well reproduce the X-ray spectrum of the source, and they concluded that the X-ray emission in this source was consistent

with being produced by a corona surrounding a standard accretion disk. In this section, we test neutral and ionized partial covering models, as well as blurred ionized reflection, on the 2018 June and 2018 December XMM-Newton/ NuSTAR observations.

3.3.1. Partial Covering

We first tested a model that includes a power law absorbed by two layers of partially covering neutral material (TBABS×ZT-BABS×ZPCFABS×ZPCFABS×ZPO). This model leaves very strong residuals across most of the spectrum and results in a very high reduced chi-squared (∼39 and ∼18 for the June and December observations, respectively) and in a very steep power law ($\Gamma \sim 7.3$ and $\Gamma \sim 5.5$, respectively). Including a blackbody component [TBABS×ZTBABS×ZPCFABS×ZPCFABS×(ZPO+ZBB)] improves the fit, but it still results in a poor reduced chi-squared (∼4.5 and ∼2 for the June and December observations, respectively). We then considered a model that includes partial covering ionized obscuration. We started by considering only a power-law continuum, as done by Gallo et al. (2013; TBABS×ZTBABS×Z-XIPCF×ZXIPCF×ZPO). This cannot reproduce well the continuum, leaving strong residuals and resulting in a reduced χ^2 of ∼1.4 for both the 2018 June and December observations. Similarly, simultaneously fitting these two observations and the 2011 observation, leaving all of the parameters of the absorbers free to vary while tying the photon index and normalization of the power-law component, results in a poor fit ($\chi^2/\mathrm{DOF} = 6609/1550$). This model fails to reproduce the spectrum even if we untie both the normalization and the photon index ($\chi^2/\mathrm{DOF} = 6539/1548$ and $\chi^2/\mathrm{DOF} = 6098/1546$, respectively). The addition of a blackbody component and of a third partially covering ionized absorber [TBABS×ZTBABS×ZXIPCF×ZXIPCF×ZXIPCF×(ZPO+ZBB)] provides a good fit for both the June ($\chi^2/\mathrm{DOF} = 346/306$) and the December ($\chi^2/\mathrm{DOF} = 617/556$) observations. However, several of the parameters obtained from the fit are quite extreme: the photon indices would be $\Gamma \sim 5-6$, the velocity of the absorbers would be up to ∼0.55c, while the unobscured luminosity of the 2018 June observation would be $\sim 2 \times 10^{47}$ erg s^{-1} cm^{-2}. This would make 1ES 1927+654 the brightest AGN in the local universe by several orders of magnitude. The strong change in the ratio between power-law and blackbody emission between the two observations (see Ricci et al. 2020) would be even more extreme than what we found, including two Gaussian lines (see Figure 13), with the fractional contribution of the power-law component to the flux increasing ∼2500 times between the 2018 June and December observations.

3.3.2. Relativistic Reflection

We also tested several relativistic reflection models (Dauser et al. 2010, 2013; García & Kallman 2010; García et al. 2013, 2014), such as RELXILLLP and RELXILLLPD (which considers a high-density accretion disk), and found that they also leave very strong residuals throughout the whole spectrum. The RELXILLLPD fit in particular results in a steep continuum ($\Gamma \sim 3.4$), a high inclination angle with respect to the disk ($i \sim 89°$, similarly to Gallo et al. 2013), and a reduced chi-squared of ∼2.7.

3.4. X-Ray and UV Variability

3.4.1. X-rays

1ES 1927+654 shows very strong variability in the 0.3–10 keV band during the three XMM-Newton observations (Figure 5), though the variability characteristics are clearly different during each exposure. During the 2018 June observation, the AGN varies by a factor of 28 in ∼27 ks (top panel), while the ratio between the minimum and maximum flux in 2018 December and 2019 May (middle and bottom panels, respectively) was only ∼4–5, and the source varied more rapidly on shorter timescales.

In Figures G1(A) and (B) (Appendix G), we show the variability in four different energy bands for the 2018 June observation. The light curves show a very similar pattern, although with different ratios between the maximum and the minimum flux, ranging between ∼18 for the 0.3–0.5 keV band to a factor of ∼159 in the 1–1.3 keV range. The light curves in six energy bands for the 2018 December observation are illustrated in Figures G2(A)–(C). Also, in this case, the variability is similar in all bands but has a different ratio between the maximum and minimum flux, ranging from ∼3 in the 0.3–0.5 keV band to ∼70 in the 2–3 keV range. During the 2019 May observation, we also found that the variability is similar in all bands (Figures G2(A)–(C)), with the ratio between the maximum and minimum flux going from ∼4 in the 0.3–0.5 keV band to ∼59 in the 1–1.3 keV band. Interestingly, for all observations, the hardness ratio varies following the flux of the source, suggesting that the radiation becomes harder when the flux increases (see Figures G1(C)–(E) and Figures G2(D)–(H)).

The XMM-Newton EPIC/PN variability spectrum of 1ES 1927+654, calculated considering timescales of 200 s, is shown in Figure 6 for the 2011 (blue diamonds; see Gallo et al. 2013) observation, as well as for the 2018 June (red filled circles), the 2018 December (green empty circles), and the 2019 May (cyan filled circles) observations. The fractional rms variability amplitude (F_{var}) was calculated following Edelson et al. (1990) and Vaughan et al. (2003, see Equations (10) and (B2) in their paper). In the 2011 observation, the source shows a peak at ∼1.5 keV and a bell-shaped variability amplitude, similar to other well-known unobscured AGNs (e.g., Gallo et al. 2004; Gierliński & Done 2006). After the optical/UV outburst, the source is much more variable than in 2011 and in particular in 2018 June, only a few months after the detection of the optical/UV brightening, when F_{var} peaks at $96 \pm 2\%$ in the 1–1.1 keV band, and then decreases to $71\% \pm 5\%$ in the 1.2–2 keV range. In 2018 December, the peak of the variability is found at higher energies ($E \geqslant 1.5$ keV) and is $F_{\mathrm{var}} = 73 \pm 1\%$, a value comparable to what was observed in the same band six months before. Interestingly, in 2018 December, the variability below ∼0.7 keV is back to a level comparable with what was found in the 2011 May observation. During the 2019 May observations, the shape of the variability spectrum of the source is similar to that observed in the 2018 December observation, with a peak in the 1.5–2 keV bin ($F_{\mathrm{var}} = 75 \pm 1\%$). During this last observation, the variability below 1 keV is significantly higher than in December ($F_{\mathrm{var}} \simeq 30 - 50\%$). In 2018/2019, the value of F_{var} above ∼1.2 keV remains unchanged, and all of the changes occur at lower energies.
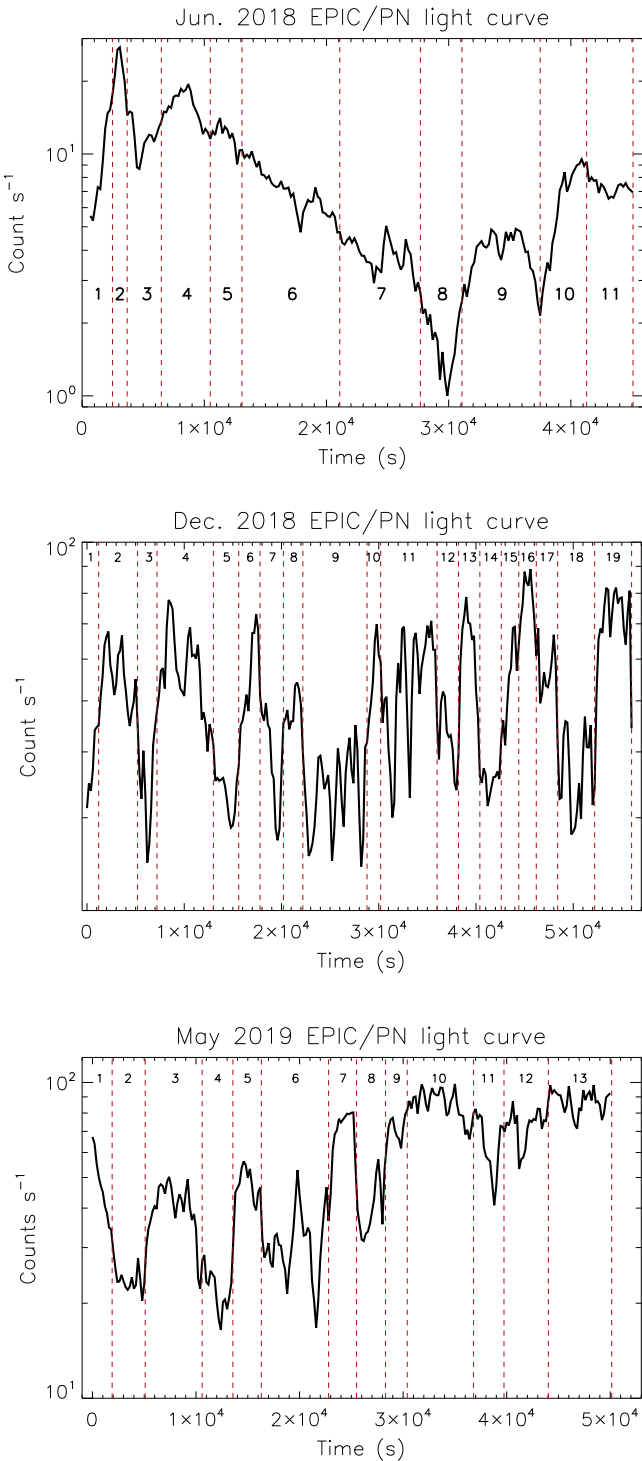
Figure 5. XMM-Newton EPIC/PN 0.3–10 keV light curve of 1ES 1927+654 for the 2018 June (top panel), 2018 December (middle panel), and 2019 May (bottom panel) observations (200 s bins). The figure also shows the intervals used for the time-resolved spectroscopy, which are denoted by the vertical red dashed lines (see Section 3.5).

3.4.2. UV

During the 2018 December XMM-Newton observation, OM carried out 11 exposures of the source in the UVW2 band (5.8 eV). In order to compare the UV and X-ray flux, we extracted EPIC/PN spectra using the same intervals adopted for the UVW2 exposures, and we fitted them using the same models

we applied for the time-resolved spectroscopy (Section 3.5). No clear correlation is found either between the 0.3–3 keV and the UVW2 flux (top panel of Figure 7), or between the UVW2 flux and the emission in different X-ray bands or considering different spectral components. Similarly, no clear trend is found when studying the relation between the UVW2 and the X-ray flux for the 14 Swift observations and the 2018 June and 2019 May XMM-Newton observations (bottom panel of Figure 7).

3.5. Time-resolved Spectroscopy

Given the very strong X-ray variability of 1ES 1927+654 on short ($\lesssim$5–10 ks) timescales, we studied its spectral evolution in different intervals using EPIC/PN for all XMM-Newton observations (Section 3.5.1). This was done by considering different good time intervals for the spectral extraction. For the 2018 June observation, we divided the exposure into 11 intervals, while for the 2018 December observation, given the higher flux and more rapid variability, we divided the observation into 19 periods. For the 2019 May observation, we considered 13 periods. The intervals used for the spectral extraction are shown in Figure 5. The exposures of the different intervals vary between 1.2 ks and 8 ks (see Appendix H). To compare the spectral variations after the optical/UV outburst with the previous X-ray observations, we also performed time-resolved spectroscopy for the 2011 XMM-Newton observation (Section 3.5.2). Due to the low flux of some of the intervals, we fitted all spectra using Cash statistics, after binning the spectra to have at least one count per bin, to avoid possible issues related to empty bins in XSPEC.

3.5.1. 2018 June/December and 2019 May

Strong spectral variability was detected in all XMM-Newton observations carried out after the optical/UV outburst. We fitted all the spectra with a model that included neutral absorption, a power law, and a blackbody component, plus a Gaussian line [TBABS×ZTBABS×(ZPO+ZBB+ZGAUSS)]. The spectral change between the highest and lowest-flux intervals can be clearly seen in the top panels of Figure 8: the spectral shape changes significantly with flux, with the source becoming harder at higher fluxes, in good agreement with what is discussed in Section 3.4.1. The middle panels of the figure show the residuals obtained by fitting the spectra with a model that did not include an emission line [TBABS×ZTBABS×(ZPO+ZBB)], highlighting the fact that the broad feature at 1 keV is present both at the highest and the lowest-flux level, with the exception of the highest luminosity intervals of the 2018 December and 2019 May observations. The bottom panels show the ratio between the best-fitting model of the highest- and lowest-flux intervals, normalized at 0.3 keV. The plot illustrates that the spectral difference arises due to both a higher-temperature blackbody (1) and a stronger power-law component (2) during the higher flux periods.

The results of the spectral fitting for all intervals using the emission line model are reported in Tables H1–H3 in Appendix H. The model reproduces the X-ray spectra of the source well in all the intervals. The temperature of the blackbody component ranges between $kT = 79^{+7}_{-7}$ eV and $kT = 183^{+4}_{-3}$ eV. A very tight relation between the flux level and the temperature of the blackbody is found for all intervals (top panel of Figure 9), with kT increasing as the source gets brighter. Fitting this trend with a function of the type
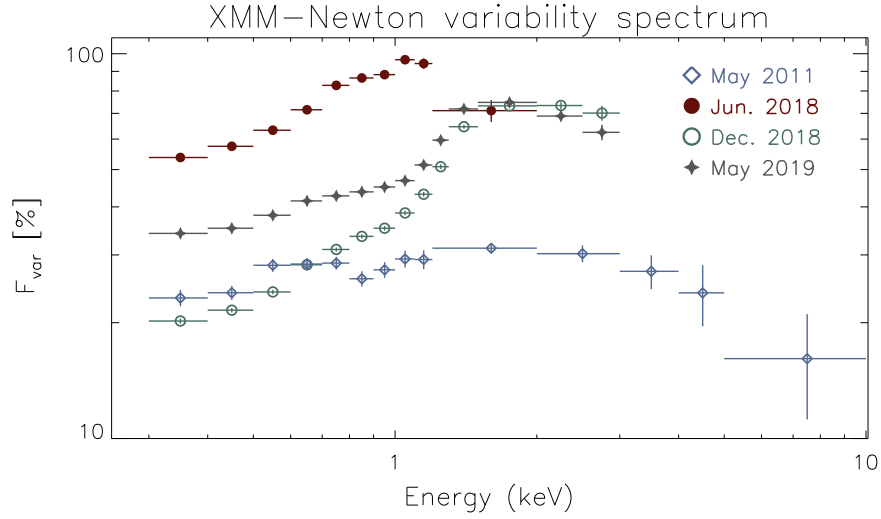
Figure 6. Variability spectra of the 2011 (blue filled diamonds), 2018 June (red filled circles), 2018 December (green empty circles), and 2019 May (gray filled stars) XMM-Newton/EPIC PN observations on timescales of 200 s. After the event, in June 2018, the source became much more variable at all energies probed here. In 2018 December and 2019 May, when the source luminosity was significantly higher, the peak of the variability is found at higher energies.
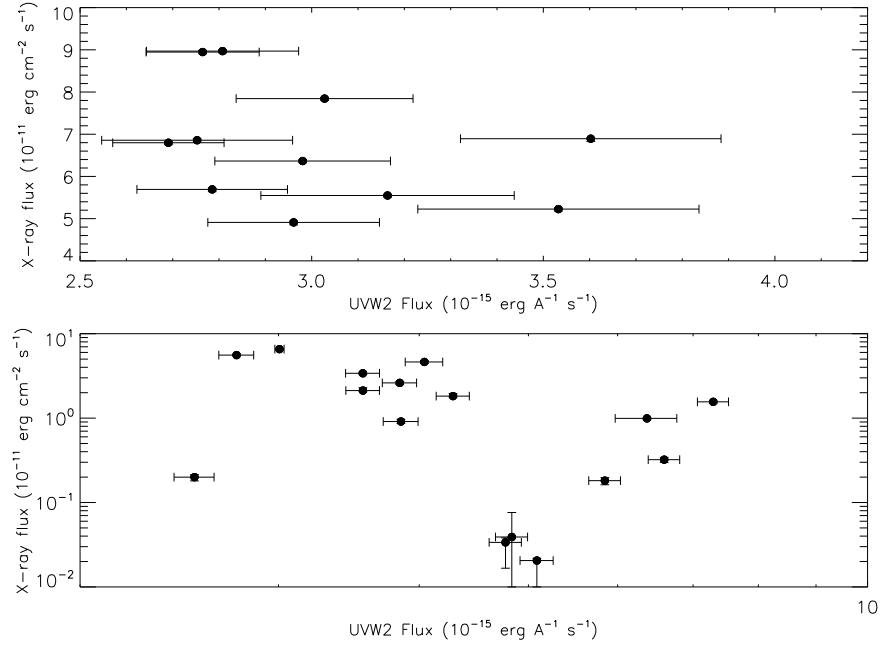

Figure 7. Top panel: X-ray flux (in the 0.3–3 keV range) vs. UVW2 flux (5.8 eV) for the simultaneous EPIC/PN and OM exposures during the 2018 December observation. Bottom panel: 0.3–3 keV flux vs. UVW2 flux for the Swift/XRT and UVOT observations, as well as for the 2018 June and 2019 May XMM-Newton observations.

$\log(L_{0.3-2}/\mathrm{erg\,s^{-1}}) = a + b * \log(kT/\mathrm{eV})$, we find a very steep slope ($b = 7.9 \pm 1.1$) for the 2018 June observation, while in 2018 December and 2019 May the trend is flatter ($b = 2.0 \pm 0.2$ and $b = 3.1 \pm 0.4$, respectively). The median photon index is $\Gamma = 3.52 \pm 0.13$ and spans a wide range ($\Gamma = 0.8-5.5$) at the lowest luminosities. No clear relation is found between the photon index and the luminosity.

The emission line is well constrained in all intervals except the most luminous ones (see central panels of Figure 8). The energy of the line does not show any significant trend with luminosity for the 2018 June observation, while in 2018 December, at the highest luminosities, the energy of the line appears to increase, up to ∼1.15 keV. No clear trend is observed in the 2019 May observation. During the 2018 June observation, the flux of the Gaussian component increases as

the source gets brighter (blue filled circles in the middle left panel of Figure 10), while in the 2018 December and 2019 May observations, the line flux shows a flat trend with luminosity and a possible decrease at the highest luminosities. A possible increase of the line width with luminosity is observed, with the Gaussian line being broader in 2018 December and 2019 May than in 2018 June.

To further examine the relation between spectral changes and luminosity, we also divided the 2018 June RGS observation into two intervals, based on their flux. The high-flux interval covers the first 13 ks of the observation (intervals 1–5 in Figure 5), while the low-flux interval covers the 21–39 ks range (intervals 7–9). We then fitted both intervals separately using our best model for the continuum, which includes a blackbody and a power law [TBABS×(ZPO+ZBB)].
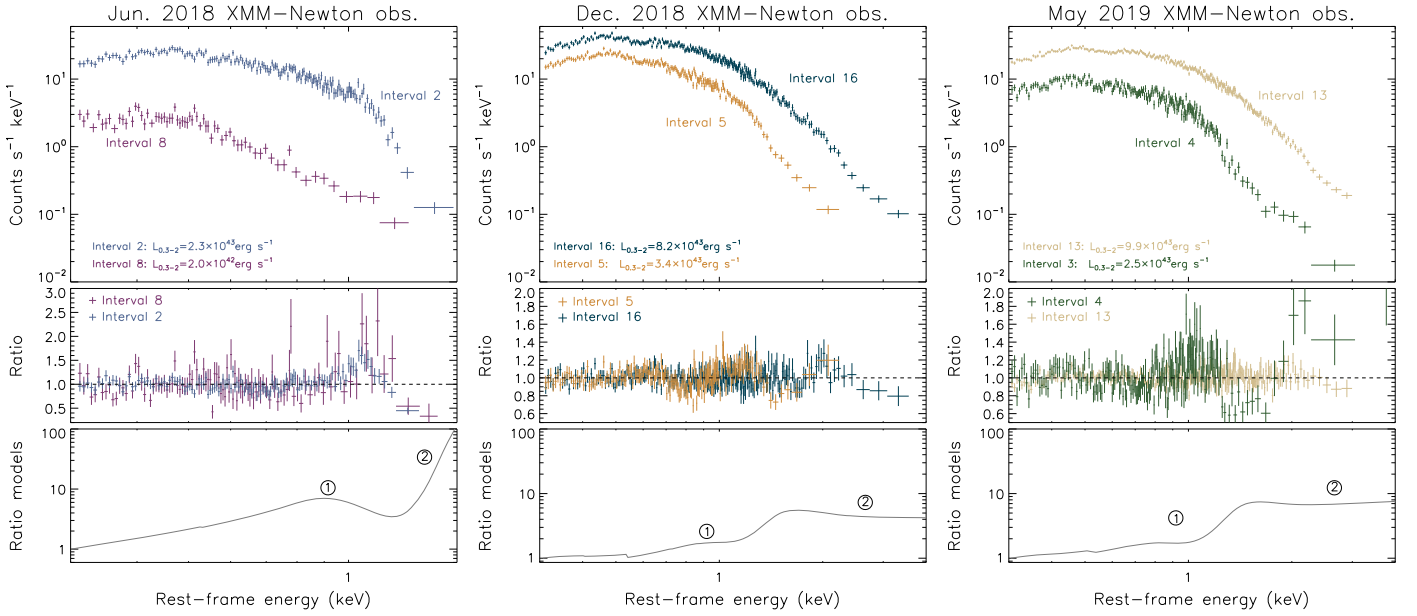
11

Figure 8. Top panels: XMM-Newton EPIC/PN spectra of the periods of the 2018 June (left panel), 2018 December (middle panel), and 2019 May (right panel) observations with the highest (intervals 2/16/13) and lowest (intervals 8/5/4) fluxes (see Figure 5). The spectral results obtained for all intervals of these three observations are reported in Tables H1–H3 of Appendix H. Central panels: ratio between the spectra and a power-law plus blackbody model, which shows the persistent presence of a feature at ∼1 keV, except at the highest luminosity (intervals 16 and 13 of the 2018 December and 2019 May observations, respectively). Bottom panels: ratio between the best-fitting spectral models of the highest- and lowest-flux intervals, after having normalized their fluxes at 0.3 keV. The plots show that the difference arises both from a higher-temperature blackbody (1) and a stronger power-law component (2).

The ratio between the model and the data is shown in Figure H1 for the low (red squares) and high (black diamonds) flux intervals. No strong change is evident between the two spectra below 1.2 keV, with the possible exception of the absorption feature at $E \simeq 0.7$–0.8 keV, which appears to be broader in the low-flux interval.

3.5.2. 2011 May

In order to compare the relation between flux ratios in different bands and the 0.3–10 keV flux with that before the outburst, we analyzed the light curves of the 2011 observations (see Appendix K for details). The ratios of different energy bands and the 0.3–0.5 keV flux versus the 0.3–10 keV flux (in bins of 1 ks) are shown in Figure K2 for the 0.75–1, 1–1.3, 1.3–2, 2–3, 3–5, 5–7 and 7–10 keV bands. We fitted 14 different intervals of this observation (see bottom panel of Figure K1) with a model that includes both a power-law and a blackbody component [TBABS×ZTBABS×(ZPO+ZBB)], leaving Γ, $N_{\rm H}$, and kT free to vary. We did not find any significant relation between the blackbody temperature and the luminosity (Table K1).

3.6. The Broad 1 keV Feature

As discussed in Section 3.5.1, we found clear evidence in the XMM-Newton observations of a broad feature at 1 keV, consistent with an emission line. The RGS spectra (see panels (A) and (B) of Figures E1 and E2 in Appendix E) show that the line might be asymmetric, with a shape that is reminiscent of the relativistically broadened profile typically observed in Fe K (e.g., Fabian et al. 2000; Walton et al. 2013) and L (e.g., Fabian et al. 2009) lines. We therefore fitted the line using the RELLINE model (Dauser et al. 2010, 2013) instead of the symmetric Gaussian line. We fixed the inner radius in RELLINE to $R_{\rm in} = -1$, so that it would self-consistently scale with the

spin (a) of the SMBH and the outer radius to $R_{\rm out} = 400\, r_{\rm g}$, where $r_{\rm g} = GM_{\rm BH}/c^2$ is the gravitational radius. The two indices of the emissivity profile were set to have the same value and were left free to vary, while the distance from the SMBH at which the indices change was fixed to an arbitrary value. The normalization and energy of the line, as well as the spin of the SMBH and the inclination angle of the system, were also left free to vary.

We studied the feature at ∼1 keV by fitting the two 2018 XMM-Newton observations simultaneously (PN, MOS, and RGS for the 2018 June observation; PN and RGS for the 2018 December observation). We did not use the 2019 May observations because the line was less prominent. We substituted the ∼1 keV Gaussian line with a relativistic line in our best model (see Sections 3.1 and 3.2), which includes a power-law and a blackbody component, as well as neutral absorption and a second Gaussian line at ∼1.8 keV [CONS×TBABS×ZTBABS×MTABLE {XSTAR} (ZBB+ZPO+RELLINE+ZGAUSS)]. We also included two absorption lines for the 2018 December observation (see Section 3.2). We left all of the parameters of the continuum, of the lines, and of the warm absorbers free to vary between the two observations, setting instead the energy of the broad line, the spin of the SMBH and the inclination angle to have the same values for both data sets. The normalization and the index of the emissivity profile were left free in both observations. The model fits the data well (Stat/DOF = 7752/7021) and results in a spin of $a = 0.41^{+0.07}_{-0.05}$, an inclination of $16.5^{+2}_{-1.5}$ degrees, and an energy of the line of $1.37^{+0.05}_{-0.03}$ keV, consistent with emission from Mg XI. During the first and second observations, the index of the emissivity profile was $8.0^{+1.2}_{-0.7}$ and $4.6^{+0.5}_{-0.3}$, respectively. The temperature of the blackbody component obtained for the June observation is consistent with the one we found using a Gaussian line (102 ± 1 eV), while that of the December observation is slightly higher (152 ± 2 eV). It should be noted however that this
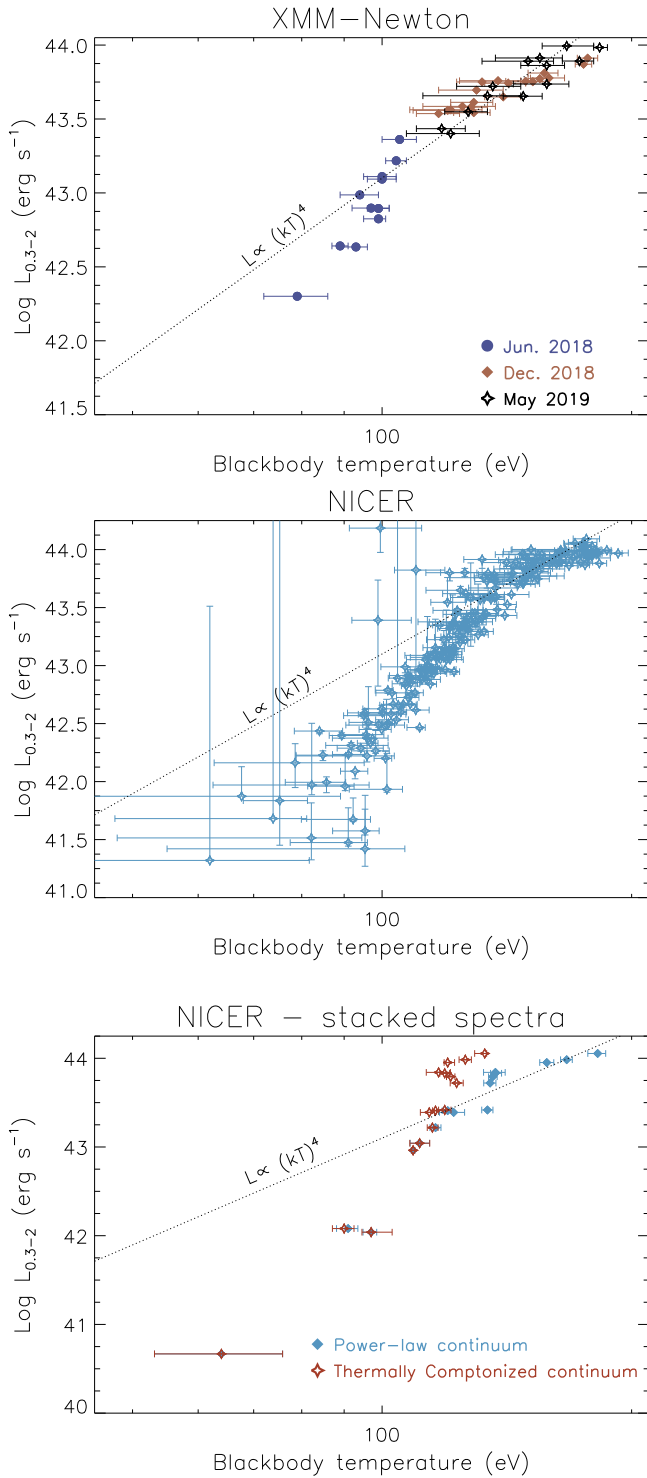
Figure 9. Top panel: temperature of the blackbody component vs. the 0.3–2 keV luminosity for the 2018 June (blue circles), 2018 December (red diamonds), and 2019 May (black stars) XMM-Newton observations (see Section 3.5). The black dotted line represents the $L \propto (kT)^4$ relation. The X-ray spectral model used included a power law, a blackbody component, and a Gaussian line (see Appendix H). Middle panel: same as the top panel for the individual NICER observations (see Section 4.2.1). Bottom panel: same as the top panel for the stacked NICER observations (see Section 4.2.2). The cyan diamonds and the red stars are the values obtained by using a power law or a thermally Comptonized continuum, respectively.

fit does not result in a significant improvement of the chi-squared with respect to a model that includes a Gaussian line instead of the relativistic line (Stat/DOF = 7754/7022).

4. The NICER Monitoring Campaign

NICER has been observing 1ES 1927+654 for about 450 days, starting from ~150 days after the beginning of the event. This very intense monitoring, together with the very large effective area of NICER, has allowed us to monitor the behavior of the source within great detail. In the following, we discuss the results obtained by studying the X-ray variability (Section 4.1) and spectroscopy (Section 4.2) of 1ES 1927+654 with NICER observations.

4.1. X-Ray Variability

The first NICER observations, carried out in 2018 May, ~150 days after the beginning of the event, found 1ES 1927+654 at a 0.5–10 keV flux level similar to that observed in the 2011 XMM-Newton observation (see Figure 1 of Ricci et al. 2020). However, the X-ray spectral shape of the source was at the time already very different from that of a typical AGN, with the continuum being dominated by a very soft component, as also seen in our Swift/XRT observations. Around the end of 2020 May, the flux of the source started to decline, reaching a minimum of ~10^{40} erg s^{-1} in 2018 July/August. In the following 100 days, the average X-ray emission increased rapidly, going even above the initial luminosity level and peaking at ~10^{44} erg s^{-1} in some intervals ~300 days after the outburst. In the following 300 days, the median luminosity continued increasing. Between 300 and 400 days from the event, it was $\log(L_{0.5-10}/\text{erg s}^{-1}) = 43.27$, in the 400–500 days range it increased to $\log(L_{0.5-10}/\text{erg s}^{-1}) = 43.89$, and finally, in the last 100 days of our monitoring campaign, it reached $\log(L_{0.5-10}/\text{erg s}^{-1}) = 44.25$. As discussed in Ricci et al. (2020), the X-ray luminosity appears to have an asymptote at $L_{0.5-10}/\text{erg s}^{-1} \sim 44.25$. Interestingly, the very strong intraday X-ray variability that was observed in the first year after the event, when the source was found to vary of up to two orders of magnitude in a few hours, decreases strongly for $t \gtrsim 400$ days. In the last few months of our campaign, 1ES 1927+654 is in fact found to vary only by ~0.3–0.5 dex in luminosity.

4.2. X-Ray Spectroscopy

In the following, we first analyze the spectra obtained from the individual NICER exposures (Section 4.2.1) and then focus on the spectra obtained by stacking different observations carried out within a few days to a few weeks from each other (Section 4.2.2).

4.2.1. Individual Spectra

We fitted a total of 232 NICER spectra, excluding 33 exposures for which the signal-to-noise ratio was not sufficient to perform spectroscopy. The fits were carried out in an energy range that went from 0.3 keV to E_2, where E_2 is the energy where the source and background rates are equal. Given the different signal-to-noise ratios of the observations, due to the very strong variability of the source, E_2 went from 0.5 keV up to 5 keV. We therefore used four different models to reproduce the X-ray emission of 1ES 1927+654.

1. The 11 observations in which the maximum energy was $E_2 < 1$ keV were fitted with Model 1, which included photoelectric intrinsic and foreground absorption, and a blackbody and a power-law component [TBABS× ZTBABS×(ZBB+ZPO)]. As we did for the XMM-Newton and Swift observations, foreground absorption was fixed at
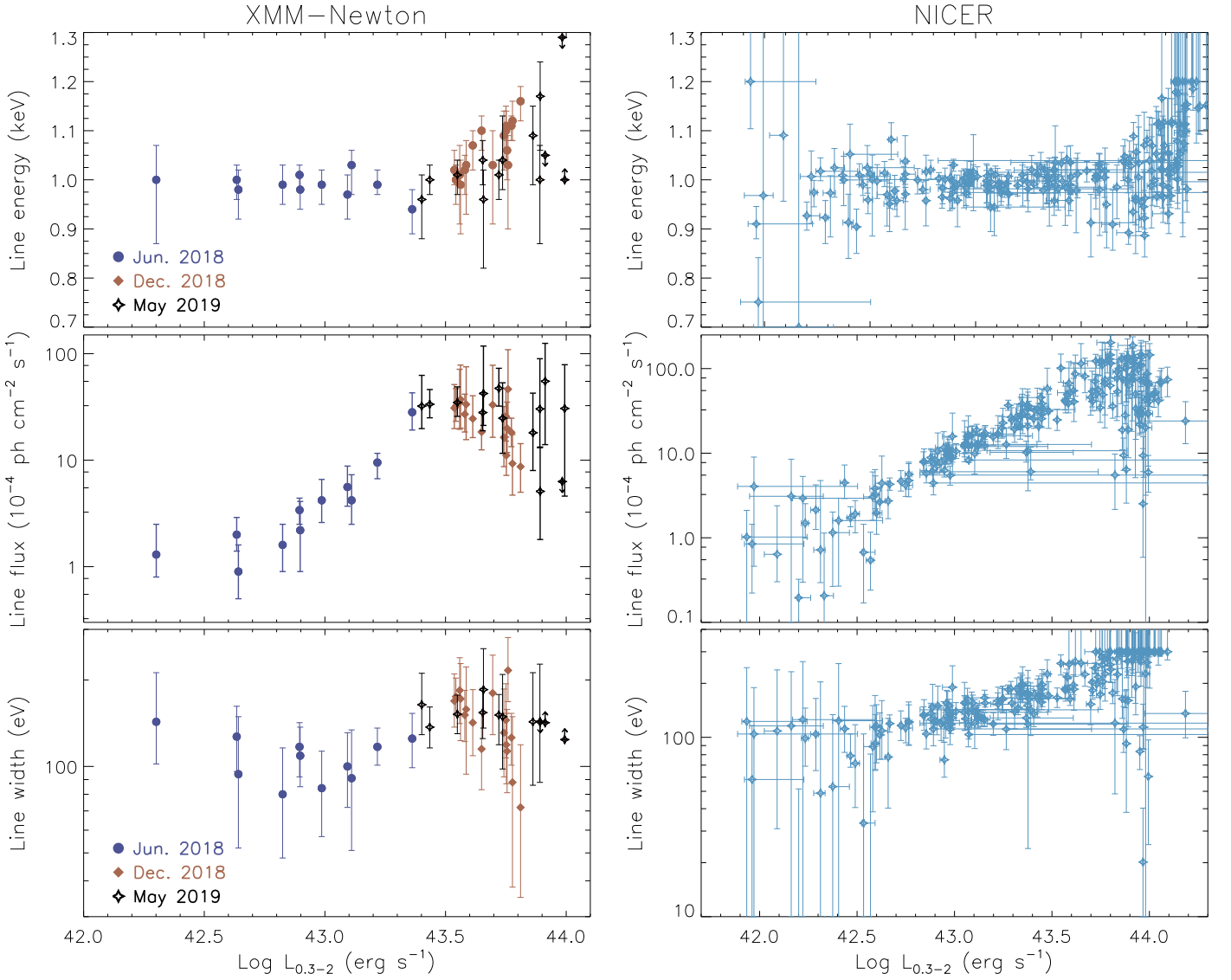
Figure 10. Left panels: relation between the properties of the broad line at $\simeq 1$ keV and the luminosity for the 2018 June (blue circles), 2018 December (red diamonds), and 2019 May (black stars) XMM-Newton observations (see Section 3.5). Right panel: same as left panels for the NICER observations (see Section 4).

the Galactic value, and all redshifts were fixed to $z = 0.019422$. Below 1 keV, the spectra of these observations were dominated by the blackbody component, therefore the photon index of the power law was fixed to $\Gamma = 3$, while the normalization was left free to vary.

2. All the exposures for which $1 \leqslant E_2/\text{keV} < 1.8$ were fitted with Model 2, which includes the same component as Model 1 plus a Gaussian line [(TBABS×ZTBABS×(ZBB +ZPO+ZGAUSS)]. The energy, width, and normalization of the line were left free to vary, while, as for Model 1, the photon index of the power law was fixed to $\Gamma = 3$. This model was used for 78 observations.

3. The 57 exposures in which $1.8 \leqslant E_2/\text{keV} < 3$ were fitted with Model 3. The only difference between this model and Model 2 is that the photon index of the power-law component was left free to vary.

4. The remaining 86 exposures were fit with Model 4, which considers a cutoff power law instead of a simple power-law [(TBABS×ZTBABS×(ZBB+ZCUT+ZGAUSS)].
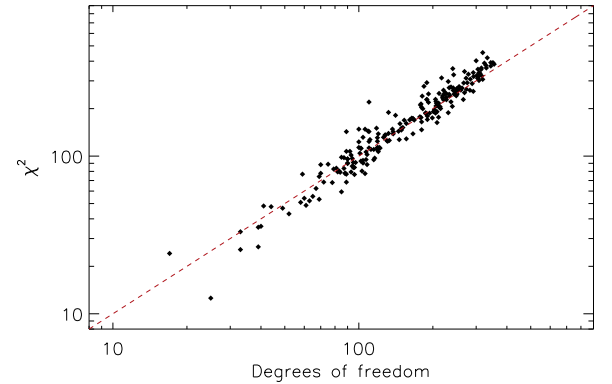

Figure 11. Chi-squared vs. degrees of freedom for the NICER spectra of our X-ray monitoring campaign. The red dashed line shows $\chi^2 = $ DOF.

The models provide typically a good fit, with the median reduced chi-squared being $\chi^2/\text{DOF} = 1.03$ (see Figure 11). The NICER observations encompass a very broad range of
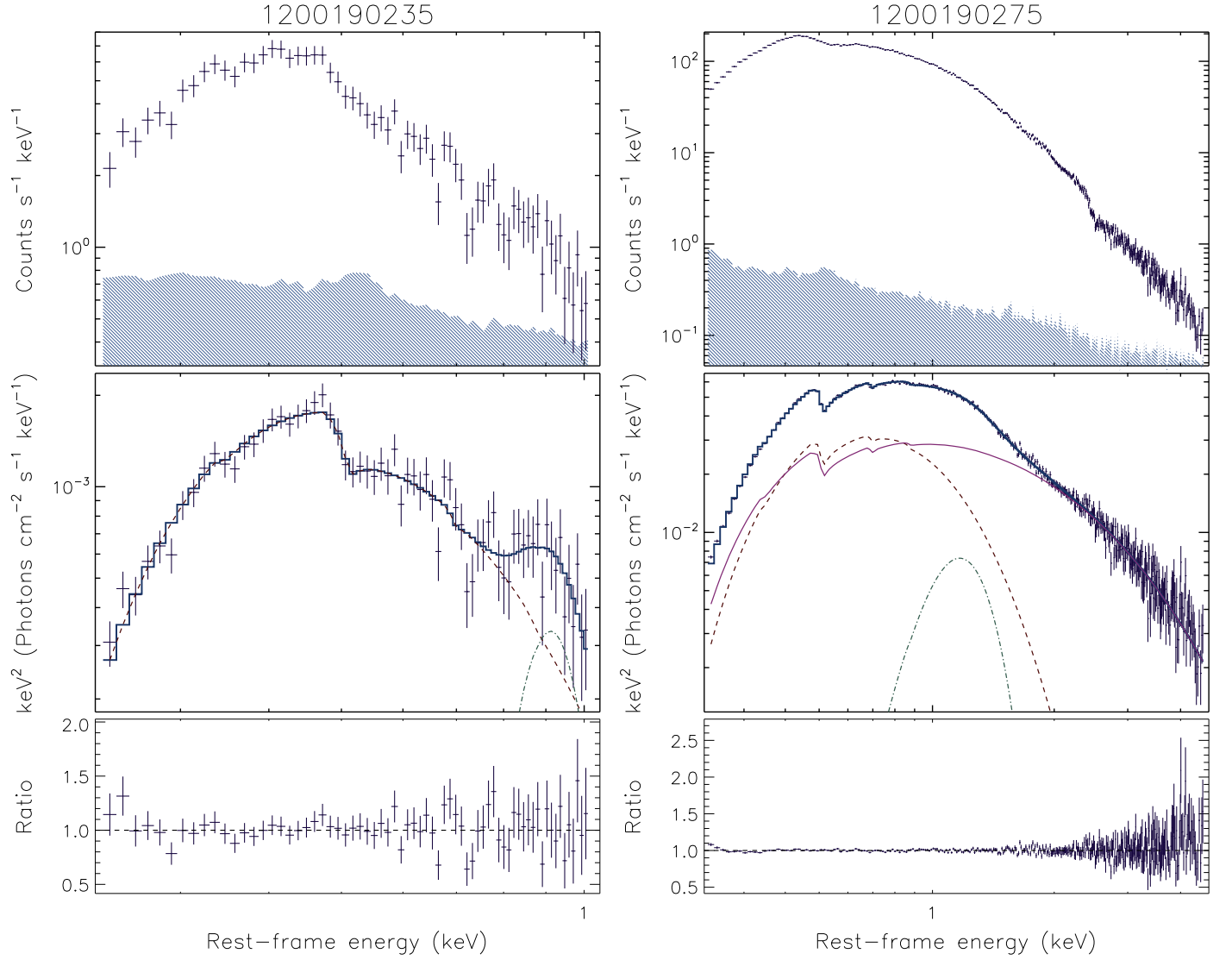
Figure 12. Examples of two fits of NICER spectra obtained during a low- ($L_{0.3-2} = 9.1 \times 10^{41}$ erg s^{-1}, left panel) and a high-flux ($L_{0.3-2} = 9.7 \times 10^{43}$ erg s^{-1}, right panel) interval. The shaded area in the top panels represent the background, while the bottom panels illustrate the ratio between the best-fitting model (continuous lines in the middle panel) and the data. During the low-luminosity periods, no power-law component is needed to reproduce the spectra, which is well fit by a blackbody component (dashed line) and a Gaussian line (dotted–dashed line). In the high-luminosity intervals, the power-law component (dotted–dotted–dashed line) reappears.

0.5–10 keV luminosities, from $\sim 10^{40}$ erg s^{-1} to $\sim 10^{44}$ erg s^{-1}. In Figure 12, we illustrate two of the NICER spectra, during a low- (left panel) and a high-luminosity (right panel) period. The harder-when-brighter behavior discussed in the previous sections is very evident when examining the NICER spectra. The blackbody temperature varies between ~ 70 eV and ~ 200 eV, and is found to correlate with the luminosity of the source (middle panel of Figure 9). Fitting this trend with the same relation we used for the time-resolved XMM-Newton observations [$\log(L_{0.3-2}/\text{erg s}^{-1}) = a + b * \log(kT/\text{eV})$; see Section 3.5] we find a slope of $b = 3.85 \pm 0.01$. A break in this $kT - L_{0.3-2}$ relation is observed at $\log(L_{0.3-2}/\text{erg s}^{-1}) \simeq 43.7$, with the trend being steeper (flatter) at lower (higher) luminosities. Fitting the two luminosity intervals separately, we find $b = 7.4 \pm 0.3$ for $\log(L_{0.3-2}/\text{erg s}^{-1}) < 43.7$ and $b = 0.9 \pm 0.2$ for $\log(L_{0.3-2}/\text{erg s}^{-1}) \geqslant 43.7$.

The properties of the ~ 1 keV Gaussian line versus the X-ray luminosity are illustrated in the right panel of Figure 10. The energy of the line (top panel) does not vary significantly up to $\log(L_{0.3-2}/\text{erg s}^{-1}) \simeq 43.7$, above which it appears to increase

up to ~ 1.15 keV. Similarly to what we have found in the XMM-Newton observations, we see a clear increase in the flux of the line (middle panel) with the luminosity. Interestingly, above $\log(L_{0.3-2}/\text{erg s}^{-1}) \simeq 43.7$ such a trend disappears, and the flux of the line appears to decrease with the luminosity. A similar behavior is observed for the width of the line (bottom panel), which increases up to $\simeq 200$ eV at $\log(L_{0.3-2}/\text{erg s}^{-1}) \simeq 43.7$ and then decreases.

4.2.2. Stacked Spectra

We also analyzed the spectral variations of 1ES 1927+654 by stacking NICER data in 16 different and successive epochs, spanning intervals between a few days and a few weeks (see Appendix J). We started by using the same approach to the spectral modeling that we used for the individuals spectra (Section 4.2.1), based on the energy range in which the spectra were not dominated by the background. Our spectral models include a blackbody component plus a Gaussian line [bb; TBABS×ZTBABS×(ZBB+ZGAUSS)], a blackbody, a Gaussian

line, and either a power law [*po*; TBABS×ZTBABS×(ZPO+ZBB +ZGAUSS)] or a cutoff power law [*cut*; TBABS×ZTBABS×(Z-CUT+ZBB+ZGAUSS)]. All the spectra for which a power-law or a cutoff power-law model was used were also fitted with a thermally Comptonized plasma [*nth*; TBABS×ZTBABS×(NTH-COMP+ZBB+ZGAUSS)]. In the latter model, the temperature of the seed photons was fixed to the temperature of the blackbody component. The results of our analysis are reported in Table J1 in Appendix J. For four spectra, we used the *bb* model, while for the remaining 12 spectra, we used the *po* or *cut* models, as well as the *nth* models. For the first interval, the model left strong residuals, suggestive of absorption features, and resulted in a chi-squared of $\chi^2/\mathrm{DOF} = 400/98$. Adding two ionized absorbers, using a XSTAR table that assumes $v_{\mathrm{turb}} = 300\,\mathrm{km\,s^{-1}}$ improved the fit significantly ($\chi^2/\mathrm{DOF} = 113/92$). The other spectra are well fit by the baseline models and do not require any additional components. The temperature of the blackbody component obtained by our fitting changes when considering the *nth* model with respect to the *po* or *cut* models, with kT being typically lower for the former model. However, as shown in the bottom panel of Figure 9, regardless of the model adopted for the hard X-ray component, we find that the blackbody temperature increases for increasing luminosities.

5. Discussion

5.1. X-Ray Spectral Properties of 1ES 1927+654

The X-ray spectral shape of 1ES 1927+654 inferred from our X-ray monitoring campaign is very different from what has been observed in typical AGN; the main peculiarities of this object are the supersoft continuum, dominated by a blackbody component ($kT \sim 80$–200 eV), the disappearance of the power-law component (Ricci et al. 2020), the broad emission features at ~ 1 keV and $\simeq 1.8$ keV, and the extremely low cutoff energy of the power law ($E_{\mathrm{C}} \sim 3$ keV). In the following, we discuss first the X-ray characteristics of 1ES 1927+654 inferred by previous studies (Section 5.1.1) and then the exceptional properties observed over the past ~ 2 yr (Section 5.1.2).

5.1.1. Previous X-Ray Observations of 1ES 1927+654

1ES 1927+654 was first detected in the X-ray band by the Einstein slew survey and classified as an AGN (Elvis et al. 1992; see also Perlman et al. 1996 and Simcoe et al. 1997). The source was later detected by the ROSAT mission in the 0.1–2.4 keV band and was reported in the all-sky survey bright source catalog (Voges et al. 1999). ROSAT observations showed that 1ES 1927+654 is very variable, and a position sensitive proportional counters (PSPC) pointed observation in December 1998 detected a strong X-ray flare. The 0.1–2.4 keV luminosities inferred by the all-sky survey and by the pointed observation were $4.6 \times 10^{43}\,\mathrm{erg\,s^{-1}}$ and $\sim 9 \times 10^{43}\,\mathrm{erg\,s^{-1}}$, respectively. Boller et al. (2003b) studied the ROSAT and Chandra spectra of this AGN and found a rapid and large-amplitude variation, together with a very steep continuum: $\Gamma = 2.6 \pm 0.3$ in the 0.1–2.4 keV band and 2.7 ± 0.2 in the 0.3–7 keV band. During the ROSAT all-sky survey, the source showed significant spectral variability, and the spectral variations did not display any clear correlation with the flux. The pointed PSPC observation showed hardness ratio variability, although also in this case, the spectral changes were not correlated with the flux variations.

Gallo et al. (2013) analyzed the 2011 XMM-Newton observation of 1ES 1927+654 (28 ks), together with a ~ 70 ks Suzaku observation, also carried out in 2011. The luminosity of the source in the 0.3–10 keV band was $8.63^{+0.05}_{-0.05} \times 10^{42}\,\mathrm{erg\,s^{-1}}$, very similar to that of the 2018 June XMM-Newton observation.[16] Gallo et al. (2013) applied several spectral models to the data, all taking into account a power-law component, plus different features, including a blackbody, two neutral partial covering absorbers, two ionized partial covering absorbers, and blurred reflection. During these observations, the narrow Fe Kα feature, which is ubiquitously found in AGNs (e.g., Nandra & Pounds 1994; Shu et al. 2010), was not detected, and only an upper limit on the EW could be obtained (EW $\lesssim 30$ eV). This is considerably lower than what would be expected for an AGN with a 2–10 keV luminosity of $3.1 \times 10^{42}\,\mathrm{erg\,s^{-1}}$: considering the well-known anticorrelation between the X-ray luminosity and the Fe Kα EW, one would in fact expect EW $\simeq 100$ eV (e.g., Iwasawa & Taniguchi 1993; Bianchi et al. 2007; Ricci et al. 2013a, 2013b, 2014; Boorman et al. 2018; Matt & Iwasawa 2019). Using a power-law plus blackbody model, similar to our baseline model, resulted in $\Gamma \simeq 2.3$, a value significantly different from the median value inferred for AGNs in the local ($z \lesssim 0.05$) universe ($\Gamma = 1.8$–1.9; e.g., Nandra & Pounds 1994; Piconcelli et al. 2005; Winter et al. 2009; Ricci et al. 2011, 2017; Lubiński et al. 2016). Most unobscured AGNs show a strong component below $\simeq 1$ keV, dubbed the soft excess, which can be typically reproduced by a blackbody component with a temperature of ~ 100 eV (e.g., Gierliński & Done 2004; Winter et al. 2009; Boissay et al. 2016; Ricci et al. 2017; García et al. 2019) and is believed to be either due to relativistic reflection from the innermost regions of the disk (e.g., Crummy et al. 2006) or to emission from a cooler Comptonizing region, possibly in the form of an atmosphere of the accretion disk (e.g., Done et al. 2012). In the case of 1ES 1927+654, the temperature of the blackbody was higher ($kT \simeq 170$ eV) than what is typically found in local AGNs.

Ionized absorbers have been systematically found in the X-ray spectra of nearby AGNs (e.g., Costantini et al. 2007; Pounds & Vaughan 2011), in some cases showing a high degree of complexity (e.g., Kaastra et al. 2014, 2018) and reaching very high velocities (e.g., Tombesi et al. 2010; Kosec et al. 2018; Boissay-Malaquin et al. 2019; Walton et al. 2019). Gallo et al. (2013) found that both an ionized partial covering model and a blurred reflection model are able to well reproduce the data. In the case of the partially covering ionized absorber, two outflows with a velocity of $\sim 0.3c$ and column densities of $3 \times 10^{22}\,\mathrm{cm^{-2}}$ and $6.6 \times 10^{23}\,\mathrm{cm^{-2}}$ were needed, while the blurred model required the system to be observed edge on.

5.1.2. The X-Ray Spectral Shape after the Optical/UV Outburst

After the optical/UV outburst (late 2017 December), the X-ray spectral shape of 1ES 1927+654 drastically changed with respect to the 2011 observation. Our analysis showed that the spectrum is dominated by a blackbody component and that the power law was extremely faint in 2018 May/June, was undetected in 2018 July–August, and reappeared only a few months later, when the flux of the source increased (Ricci et al. 2020). In Section 3.3, we discussed how neither partial covering nor blurred reflection models can explain the X-ray properties of 1ES 1927+654 observed after the optical event.

---

[16] $L_{0.3-10} = 8.54^{+0.10}_{-0.34} \times 10^{42}\,\mathrm{erg\,s^{-1}}$
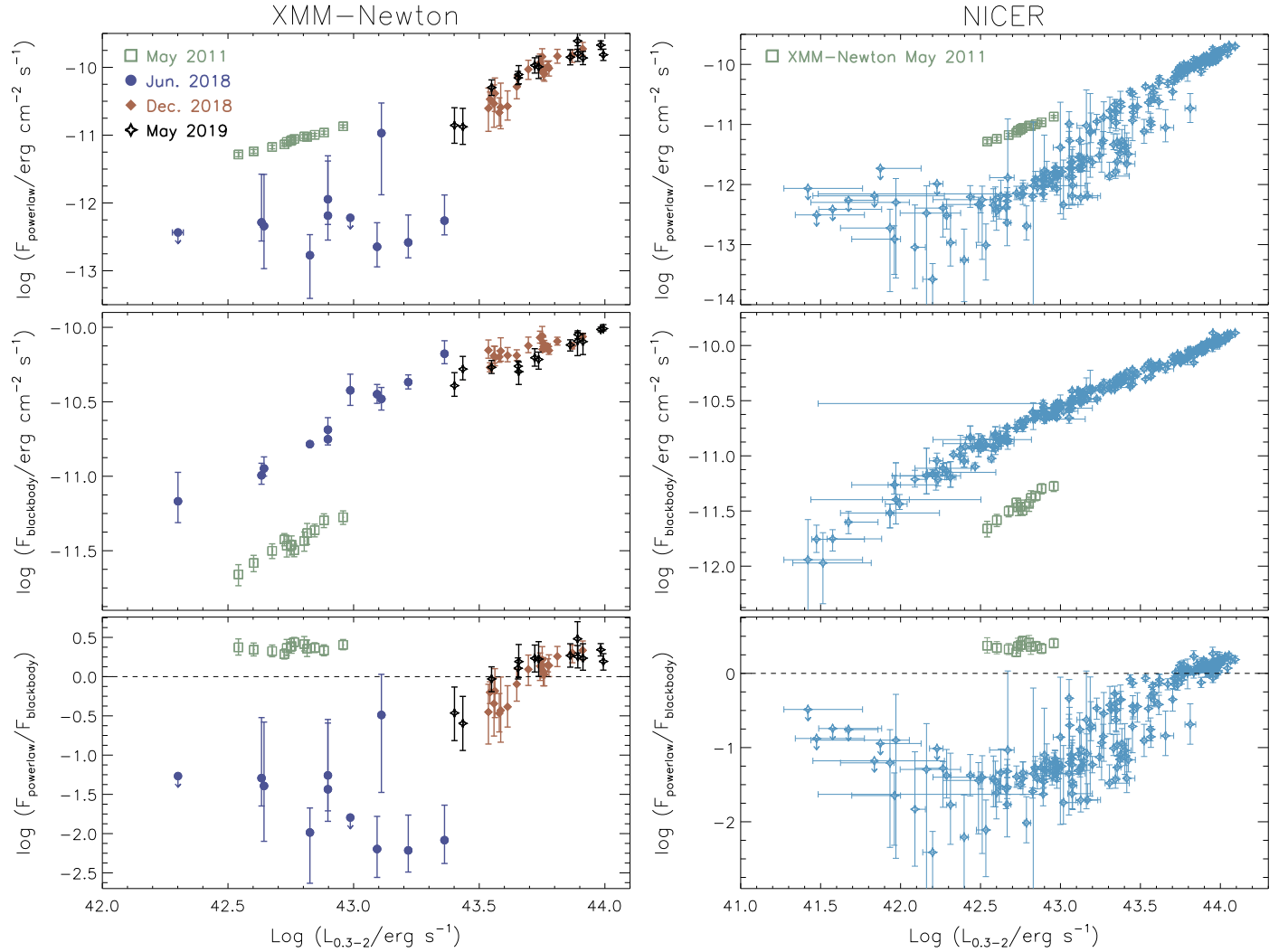
Figure 13. Left panels: relation between the contribution of the different spectral components to the 0.3–2 keV flux and the total luminosity for the 2018 June (filled blue circles), 2018 December (filled red diamonds), and 2019 May (empty black stars) XMM-Newton observations. The top and middle panels show the flux of the power-law (F_{powerlaw}) and blackbody ($F_{\mathrm{blackbody}}$) components, respectively, while the bottom panel shows their ratio. Right panels: same as the left panels for the NICER observations.

A supersoft X-ray continuum has so far been observed only in handful of objects classified as AGN (e.g., Terashima et al. 2012; Miniutti et al. 2013, 2019; Sun et al. 2013; Lin et al. 2017a; Shu et al. 2017, 2018; Giustini et al. 2020), and never before was the power law observed in the process of disappearing. The XMM-Newton and the NICER observations show that the flux of the power law and that of the blackbody component increases with the 0.3–2 keV luminosity of the source (top and middle panels of Figure 13; see also Ricci et al. 2020). While for the same luminosity interval covered by the 2011 XMM-Newton observation [$\log(L_{0.3-2}/\mathrm{erg~s}^{-1}) \sim 42.5$–43] the flux of the power-law component after the event is considerably lower than in 2011 (green empty squares), that of the blackbody component is ~ 0.7 dex higher. Interestingly, the ratio between the flux of the power law and that of the blackbody shows a clear increase with luminosity (see Figure 3 of Ricci et al. 2020), going from $\sim 10^{-2}$ for $\log(L_{0.3-2}/\mathrm{erg~s}^{-1}) \lesssim 43$ to $\sim 10^{0.4}$ for $\log(L_{0.3-2}/\mathrm{erg~s}^{-1}) \sim 44$ (Figure 13). The transition between having a blackbody-dominated flux to a power-law-dominated one is found at $\log(L_{0.3-2}/\mathrm{erg~s}^{-1}) \sim 43.7$, and at the highest luminosities, the source goes back to having a ratio comparable to that observed in 2011 May (Ricci et al. 2020).

The power law is very steep ($\Gamma \sim 3$), and our joint XMM-Newton/NuSTAR observations showed that the addition of a cutoff with a very low energy ($E_{\mathrm{cut}} \sim 3$ keV; see Table 1) is required (see Figures 4(B) and (C)). This value is considerably lower than what is typically observed in nearby accreting SMBHs. From the analysis of the broadband X-ray properties of the ~ 840 AGNs detected by Swift/BAT during the first 70 months of operations, Ricci et al. (2017) found that the median cutoff energy is 200 ± 29 keV (210 ± 36 keV for unobscured AGNs). Previous BeppoSAX observations found consistent results (230 ± 22 keV for unobscured AGNs; see Dadina 2007, 2008). Recent NuSTAR observations have also confirmed that the cutoff energy is typically found between ~ 40 keV (Kara et al. 2017) and ~ 200–300 keV (e.g., Tortosa et al. 2017, 2018; Kamraj et al. 2018; Baloković et al. 2020), with the highest recorded value thus far being for NGC 5506 ($E_{\mathrm{cut}} = 720^{+130}_{-190}$ keV; Matt et al. 2015). A relation between the cutoff energy and the Eddington ratio was recently found by Ricci et al. (2018), who showed that sources with higher λ_{Edd} tend to have cooler coronae. This could be explained by the fact that AGNs typically tend to avoid the region in the temperature–compactness parameter space where runaway pair production dominates

(Bisnovatyi-Kogan et al. 1971; Svensson 1984; Fabian et al. 2015, 2017). Extending the relation of Ricci et al. (2018) to higher Eddington ratios, assuming that the trend does not change at $\lambda_{\rm Edd} \gg 1$, one would expect to find such low values of $E_{\rm cut}$ only for $\lambda_{\rm Edd} \sim 30$. Assuming instead the relation between the photon index and the Eddington ratio (e.g., Shemmer et al. 2006; Brightman et al. 2013; Trakhtenbrot et al. 2017), and in particular the one obtained by Trakhtenbrot et al. (2017) considering a cutoff power-law model ($\Gamma = 2.00 + 0.167\log\lambda_{\rm Edd}$), one would need $\lambda_{\rm Edd} \sim 6$ to obtain the photon index found by our observations. It should be however remarked that the physical properties of the corona at these extreme Eddington ratios, where the accretion flow might be very different (e.g., Abramowicz et al. 1988), are still unclear.

The black hole mass of 1ES 1927+654, inferred by Trakhtenbrot et al. (2019a) by analyzing broad Balmer lines, is $1.9 \times 10^7 M_{\odot}$. As discussed in Ricci et al. (2020), the black hole mass could however be quite different, due to the fact that the BLR clouds might not have had the time to virialize. This is also shown by the variable FWHM of both Hα and Hβ (R. Li et al. 2021, in preparation; see Appendix A of Ricci et al. 2020). The stellar mass of the galaxy ($2.3 \times 10^9 M_{\odot}$) suggests $M_{\rm BH} \sim 10^6 M_{\odot}$ (Kormendy & Ho 2013). At $\gtrsim 300$ days after the optical outburst, the optical/UV flux had decreased strongly (Trakhtenbrot et al. 2019a), and most of the emission is observed in the X-rays (Ricci et al. 2020). Assuming that the X-ray bolometric correction is $\kappa_{\rm X} \sim 1$ and $M_{\rm BH} \sim 10^6 M_{\odot}$, the maximum observed X-ray luminosity would correspond to $\lambda_{\rm Edd} \sim 1$. Therefore, we can conclude that the maximum Eddington ratio would be $\lambda_{\rm Edd} \simeq \kappa_{\rm X} \gtrsim 1$, and it is likely that the source was super-Eddington for a considerable fraction of its time during our monitoring campaign. In a forthcoming publication (R. Li et al. 2021, in preparation), we will discuss in detail the spectral energy distribution of this source. It should be noted that some of the properties of 1ES 1927+654 after the optical outburst, such as its softness, are similar to those of some of the most extreme narrow-line Seyfert 1 s, e.g., 1H 0707 $-$495 and IRAS 13224$-$3809 (e.g., Boller et al. 2003a; Fabian et al. 2004). However, none of these sources shows a power-law component as steep and faint as 1ES 1927+654. Interestingly, both 1H 0707$-$495 and IRAS 13224$-$3809 show an excess due to a relativistically broadened Fe L line at 0.9 keV (Fabian et al. 2009, 2013). The energy of this line is, however, lower than that of the feature observed in the X-ray spectrum of 1ES 1927+654 ($E = 1.01 \pm 0.01$ keV; see Table 1).

Similarly to the 2011 observations, we do not see any sign of a Fe Kα line at 6.4 keV. This is not surprising, due to the very low flux of the source at 7.1 keV. However, we could in principle expect to see an Fe Kα echo from more distant material (e.g., the BLR or the torus), which is not found in any of our X-ray observations. This, together with the absence of a Compton hump, suggests that the circumnuclear environment of 1ES 1927+654 is particularly poor in gas and dust. The two broad emission lines observed at ~ 1 keV and $\simeq 1.8$ keV are also extremely puzzling, and they have not been observed in any other AGN thus far. The line at ~ 1 keV could be associated with Ne X (1.02 keV) or with the ionized Fe-L emission from Fe XX–XIV. In the latter case, the increase in the energy of the line observed at the highest luminosities (top panels of Figure 10) might be related to the increase in the ionization state of the circumnuclear material. The second line is found at $E \sim 1.7$ keV during the first XMM-Newton

observation and at ~ 1.9 during the second and third observations. While the line at ~ 1.7 keV could be Si Kα (1.74 keV) or Al XIII (1.73 keV), it is unclear to what transition the line at ~ 1.9 could be associated. It should be stressed that we cannot exclude that these two broad features are produced by strong and very turbulent ionized outflows, and we refer to a future publication (M. Masterson et al. 2021, in preparation) for a detailed analysis.

5.2. The Peculiar X-Ray Spectral Variability

Our X-ray monitoring campaign (Sections 3–4) showed a clear relation between the spectral shape and the flux of the source. This was observed in all X-ray observations, with the spectrum becoming harder as the flux increased. This effect was first illustrated, in a model-independent way, by the fact that (i) the flux ratios between different bands and the softest (0.3–0.5 keV) band follow the same pattern as the overall variability (see Figures G1(C)–(E) and Figures G2(D)–(H)); (ii) when we plot the flux ratios in each band as a function of the total flux (see Figure G3 in Appendix G and Figure I1 in Appendix I for XMM-Newton and NICER, respectively), we see a very clear correlation in all bands, up to the 2–3 keV bin for XMM-Newton (i.e., the limit of our EPIC/PN detections); (iii) comparing the spectra of the highest- and lowest-flux intervals (top panels of Figure 8) and looking at their ratios (bottom panels of Figure 8), we see a clear hardening. This effect is due to both the increase of the temperature of the blackbody with the X-ray luminosity (Figure 9) and to the increase of the ratio between the flux from the power-law and blackbody component with luminosity (see Figure 13 and Ricci et al. 2020). The harder-when-brighter behavior does not appear to be associated with variations of the outflowing material. Fitting the X-ray spectra with a blackbody component in a range that is not strongly affected by the ionized absorbers (0.3–0.5 keV), we obtain a significant difference in the temperature of the blackbody of low- and high-luminosity intervals. In particular, for the 2018 June XMM-Newton observation, we obtain $kT = 122^{+7}_{-6}$ eV and $kT = 88^{+7}_{-6}$ eV for the brightest (interval 2) and faintest (interval 8) periods (see Figure 5). Moreover, no clear difference is observed in the RGS spectra of two intervals with very different fluxes during the 2018 June observation (Figure H1 in Appendix H).

Unobscured AGNs typically show a softer-when-brighter behavior (e.g., Sobolewska & Papadakis 2009) in the X-rays. This is likely related to the steepening of the power-law component for increasing luminosities (e.g., Shemmer et al. 2006), which is also found in Galactic black hole binaries (e.g., Wu & Gu 2008). On the other hand, the temperature of the blackbody component, adopted to reproduce the soft excess, does not vary with the source luminosity (e.g., Gierliński & Done 2004). At low Eddington ratios ($\lambda_{\rm Edd} \lesssim 10^{-2}$), it has been shown that AGNs can present a harder-when-brighter behavior (e.g., Constantin et al. 2009; Gu & Cao 2009; Younes et al. 2011; Emmanoulopoulos et al. 2012; Connolly et al. 2016), which is however entirely related to the power-law component and that results in a negative correlation between Γ and $\lambda_{\rm Edd}$. Such a trend has also been observed in black hole binaries in the low/hard state (e.g., Kalemci et al. 2004; Yamaoka et al. 2005; Yuan et al. 2007), and it has been argued that such behavior might be related to the fact that accretion in these objects happens through an advection-dominated accretion flow (ADAF; Ichimaru 1977; Ho 2008; Yuan & Narayan 2014).

Such a trend has been also observed in blazars (e.g., Krawczynski et al. 2004), where shocks and synchrotron self-Compton processes in the jet are thought to be responsible for the hardening of the X-ray radiation (Ghisellini et al. 2009). There are however important differences between the case of 1ES 1927+654 and that of low-Eddington-ratio AGNs, black hole binaries in the low/hard state, and blazars, which suggest that the physical mechanisms responsible for the spectral variability might be very different. The spectral shape of 1ES 1927+654 is in fact extremely soft, with a very strong blackbody component, while low-Eddington-ratio AGNs and blazars have significantly harder continua. Moreover, the power-law component does not show any spectral variation with luminosity, contrary to what is found in ADAF and strongly jetted AGNs.

5.3. The Origin of the Blackbody Component

In Ricci et al. (2020), we discuss how the event that created the broad lines, and drastically transformed the X-ray properties of 1ES 1927+654, might be related to a TDE in an AGN (e.g., Merloni et al. 2015; Blanchard et al. 2017; Liu et al. 2020). The blackbody component, observed in all X-ray spectra of 1ES 1927+654 after the optical event, could be produced in an accretion disk. However, assuming $M_{BH} \sim 10^6 M_\odot$, one would expect the maximum temperature to be ~ 35 eV (~ 100 eV) at the highest luminosity for a nonrotating (maximally rotating) black hole, assuming $\kappa_X \simeq 1$ (see Equation (F1) in Appendix F.1.2). This is considerably lower than that recovered from our fitting ($kT \sim 200$ eV or $kT \sim 235$ eV, for a blackbody or a disk blackbody, respectively). As discussed in Section 5.1.2, it is likely that $\kappa_X \geqslant 1$, which could lead to a disk temperature consistent with our observations (particularly if $\kappa_X \gtrsim 15$). Moreover, the color temperature correction for $M_{BH} \sim 10^6 M_\odot$ could be $\gtrsim 2$ (Done et al. 2012), which would also contribute to increasing the observed blackbody temperature.

The blackbody radius varies between $\sim 4 \times 10^9$ cm (at $\sim 10^{40}$ erg s^{-1}) and $\sim 7 \times 10^{10}$ cm (at $\sim 10^{44}$ erg s^{-1}), assuming $M_{BH} \sim 10^6 M_\odot$ and $\kappa_X \sim 1$. This is lower than the gravitational radius of the source, $R_g = GM_{BH}/c^2 \sim 1.5 \times 10^{11}$ cm (assuming $M_{BH} \sim 10^6 M_\odot$), which might suggest that the blackbody emission cannot be easily explained by a standard accretion disk, unless a high inclination angle with respect to the normal to the disk is assumed. Even if the black hole mass was considerably lower (e.g., $\sim 10^5 M_\odot$), the gravitational radius ($\sim 1.5 \times 10^{10}$ cm) would still be larger than the blackbody radius at the lowest luminosities observed here. Only a black hole mass of $\lesssim 5 \times 10^4 M_\odot$ would be consistent with the observations. In fact, while the blackbody radius would be larger than the gravitational radius at the highest luminosities for $\kappa_X \gtrsim 5$, at the lowest luminosities, one would need a rather extreme value of the X-ray bolometric correction ($\kappa_X \gtrsim 1200$). However, at this time (i.e., ~ 200 days after the event), the optical emission was remarkably stronger than in the X-rays (Trakhtenbrot et al. 2019a; Ricci et al. 2020), and the 5100 Å luminosity was $\sim 10^{43}$ erg s^{-1}, which could correspond to a bolometric luminosity of $L \sim 10^{44}$ erg s^{-1} (e.g., using the bolometric corrections of Kaspi et al. 2000). This would lead to a blackbody radius of $\sim 4 \times 10^{11}$ cm $> R_g$, resolving this discrepancy. Therefore, we conclude that the soft X-ray emission could be associated with an accretion disk, provided that the X-ray bolometric corrections are high enough.

1ES 1927+654 shows very strong spectral variability during our campaign, with the temperature of the blackbody component

increasing with the luminosity (Figure 9). This behavior is very different from what is typically observed in TDEs, which show little evolution in the temperature of the blackbody component. Interestingly, a similar behavior has also been observed in the narrow-line Seyfert 1 IRAS 13224−3809 (Chiang et al. 2015), and it was explained as being possibly related to the heating of the inner disk by the X-ray corona and by the effect of light bending, which allows radiation emitted and/or reflected by the disk to illuminate its surface. If the event were due to a TDE in a preexisting AGN, part of the X-ray radiation could be produced in the shocks between the debris and the disk, which would produce the observed harder-when-brighter behavior. The latter scenario will be tested in details in a forthcoming publication (M. Masterson et al. 2021, in preparation). Interestingly, such behavior has been recently observed also in a candidate TDE with peculiar properties (Lin et al. 2017b), as well as in recent observations of supersoft X-ray AGNs (e.g., Shu et al. 2017; Miniutti et al. 2019; Giustini et al. 2020), objects which could also be associated with TDEs (e.g., Shu et al. 2018; King 2020).

5.4. 1ES 1927+654 and True Type 2 AGNs

Before becoming a Type 1 AGN, 1ES 1927+654 was considered to be one of the clearest cases of true Type 2 AGN (e.g., Tran et al. 2011), i.e., unobscured sources lacking the BLR (e.g., Tran 2001; Panessa & Bassani 2002). A large fraction of these objects are found to accrete at $\lambda_{Edd} \lesssim 10^{-2}$ (e.g., Panessa et al. 2009; Bianchi et al. 2012b). It has been argued that this would be in agreement with models that predict the disappearance of the BLR at low Eddington ratios (e.g., Nicastro 2000), such as the disk-wind scenario (e.g., Elitzur & Ho 2009; Elitzur et al. 2014). In some cases, however, these sources have been found to have high accretion rates (e.g., Ho et al. 2012), which led Elitzur & Netzer (2016) to argue that the dependence on black hole mass might relax the limits on the accretion rate in the disk-wind model. A number of obscured AGNs were also thought to lack a BLR, as suggested by the nondetection of polarized broad lines (e.g., Tran 2003). Marinucci et al. (2012) found that most of these objects have low Eddington ratios ($\lambda_{Edd} < 10^{-2}$), possibly also in agreement with the disk-wind scenario. However, thanks to VLT/FORS2 optical spectropolarimetry observations, Ramos Almeida et al. (2016) were able to find polarized broad lines in several of these objects, questioning whether the lack of detection of broad lines was only related to dilution due to stellar emission in the host galaxy. Recently, using Hubble Space Telescope (HST) spectroscopy, Bianchi et al. (2019) found that the archetypal true Type 2 AGN NGC 3147 actually has very broad lines, which show an asymmetric relativistic profile. The fact that the BLR was not detected before in this object is due to (i) the very broadened emission profile, caused by the high mass ($2.5 \times 10^8 M_\odot$) of the black hole and by the small distance ($\sim 80\, r_g$) between the SMBH and the BLR (due to the low luminosity of the object, e.g., Kaspi et al. 2005); and (ii) the intrinsic weakness of the optical emission with respect to the host galaxy. NGC 3147 has in fact a 2–10 keV luminosity of $3.3 \pm 0.1 \times 10^{41}$ erg s^{-1} ($\lambda_{Edd} \simeq 10^{-4}$; Bianchi et al. 2017).

These results seem to suggest that most true Type 2 AGNs are just Type 1 AGNs in which the broad lines are too broad and/or too faint to be detected. This might also be important for changing-look AGNs (e.g., Dexter et al. 2019; Frederick et al. 2019; Yan et al. 2019). So far, no object has been found to show changes in both the level of obscuration and in the optical type.

Therefore, at the beginning/end of the changing-look event, a fraction of sources would be classified as unobscured Type 2 AGNs. In 2011, before the outburst, 1ES 1927+654 had a 2–10 keV luminosity an order of magnitude larger than NGC 3147 (3.3×10^{42} erg s^{-1}; Gallo et al. 2013). Using the relation between the radius of the BLR and the X-ray luminosity inferred by Kaspi et al. (2005), we find that the BLR would lie at ∼5 light-days from the SMBH, which corresponds to ∼4,500 $r_{\rm g}$ for $M_{\rm BH} = 1.9 \times 10^{7} M_{\odot}$ (∼88,000 $r_{\rm g}$ for $M_{\rm BH} = 10^{6} M_{\odot}$), a factor of ∼60 (∼1200) larger than NGC 3147. One would therefore not expect to see extremely broad lines in this object. From the relation between the luminosity of the broad Hα line ($L_{\rm bH\alpha}$) and that in the X-ray band (Stern & Laor 2012), we would expect $L_{\rm bH\alpha} \simeq 10^{42}$ erg s^{-1}. As shown by Stern & Laor (2012; see their Figure 14), this is considerably higher than the upper limit on the broad Hα line ($L_{\rm bH\alpha} \lesssim 3 \times 10^{39}$ erg s^{-1}) inferred by Tran et al. (2011) for 1ES 1927+654. This, together with the lack of Fe Kα emission and of a Compton hump, suggests that before the event, 1ES 1927+654 might have had accretion properties rather different from those of typical AGNs.

5.5. 1ES 1927+654 and Changing-look AGNs

Over the past years, several dozens of changing-look AGNs have been discovered at different wavelengths (e.g., Yang et al. 2018; MacLeod et al. 2019; Hon et al. 2020; Sheng et al. 2020). A few of these objects have been followed up and studied in detail in the X-ray band. 1ES 1927+654 shows several extreme characteristics that have not been observed in other changing-look AGNs. In particular, 1ES 1927+654 is the only changing-look AGN that has been found to undergo a complete transformation of its X-ray spectral properties and to show X-ray variability of over four orders of magnitude on timescales of months. Moreover, another peculiarity of 1ES 1927+654 is that the broad optical lines were found to disappear a few months after they were created (Trakhtenbrot et al. 2019a).

Several changing-look AGNs show little X-ray spectral variability and characteristics consistent with those of typical AGNs. NGC 1566 was found to transition from Sy 1.8-19 to Sy 1.2 (Oknyansky et al. 2019) following an increase by a factor of ∼40–70 in the X-rays. After the changing-look event, at the peak of the X-ray luminosity, its overall X-ray spectral properties however were not remarkably different from those of nearby AGNs (Parker et al. 2019). HE 1136−2304 brightened in the X-rays by a factor of ∼30, which was accompanied by an increase in the flux of the Balmer lines, causing a transition from a Sy 1.9 to a Sy 1.5 (Parker et al. 2016). The X-ray properties of this source are also not very different from those of typical AGNs, with the source showing a well-defined power-law component. Wang et al. (2020) found that the X-ray luminosity decreases (increases) as UGC 3223 transitions from Sy 1.5 to Sy 2 (Sy 2 to Sy 1.8), but did not find evidence of strong X-ray spectral variations.

On the other hand, Noda & Done (2018) showed that the appearance/disappearance of broad optical lines in Mrk 1018 (Husemann et al. 2016; McElroy et al. 2016; Krumpe et al. 2017) could be directly associated with the presence/absence of a strong soft excess in the X-rays, which extends to the UV and is responsible for the ionizing photons responsible for the emission lines. Noda & Done (2018; see also Ruan et al. 2019a, 2019b) discussed that these variations are similar to the soft-to-hard state transition in black hole binaries, where the inner disk is replaced

by an ADAF as the Eddington ratio decreases. This behavior is remarkably different from what was observed in 1ES 1927+654, which showed an extremely strong soft X-ray component even after the disappearance of the broad lines. Recently, Ai et al. (2020) found evidence of a harder-when-brighter behavior in the changing-look AGN SDSS J155258+273728, ascribed to a flattening of the power-law component for increasing luminosities. They associated this behavior with the low Eddington ratio of this source, which, as discussed in Section 5.2, is very different from that observed for 1ES 1927+654.

The properties of 1ES 197+654 seem to suggest that the changing-look event is very different from those observed in the aforementioned sources and that it could be associated with a TDE (Ricci et al. 2020). An alternative explanation for the origin of the event in 1ES 1927+654 has been recently proposed by Scepi et al. (2021), who argued that the inversion of magnetic flux in a magnetically arrested disk could explain its X-ray and optical light curves, as well as the observed timescales.

6. Summary and Conclusions

We reported here the results obtained by our 2018/2019 X-ray monitoring campaign of the changing-look AGN 1ES 1927+654. The source, which was previously classified as an unobscured Type 2 AGN ($N_{\rm H} \simeq 10^{20}$ cm^{-2}), was found to have significantly increased its optical flux in 2018 March. Prediscovery detections from ATLAS showed that the event started on 2017 December 23. Our optical spectroscopic follow-up campaign showed, for the first time, evidence of strong broad Balmer emission lines in this source, ∼1–3 months after the optical flux rise (Trakhtenbrot et al. 2019a). Our X-ray monitoring campaign includes 265 NICER (for a total of 678 ks) and 14 Swift/XRT (26 ks) observations, as well as three simultaneous XMM-Newton/NuSTAR (158/169 ks) exposures.

In the X-rays, 1ES 1927+654 shows a behavior unlike any other AGN. The main characteristics of the source are the following.

1. After the optical/UV outburst, the source is found to show a supersoft X-ray continuum, with the emission being almost entirely due to a blackbody component ($kT \simeq 100$ eV). The power-law component, ubiquitously found in AGNs, and which was present in previous X-ray observations, had almost completely disappeared (top panel of Figure 3 and left panel of Figure 12).

2. When the flux of the source increases, a steep power-law component reappears. The ratio between the power-law and blackbody flux increases with the luminosity, with the power law dominating at $\log(L_{0.3-2}/{\rm erg\ s}^{-1}) \gtrsim 43.7$ (Figure 13 and Ricci et al. 2020).

3. The source shows extremely strong X-ray variability, with an amplitude of two orders of magnitude on timescales of a few hours (Figure 5) and of up to four orders of magnitudes on timescales of a few months (Figure 1 of Ricci et al. 2020).

4. The variability spectrum inferred from XMM-Newton observations (Figure 6) shows that the peak of the variability moves to higher energies when the X-ray luminosity increases. The X-ray variability is found to be completely disconnected from the UV variability (Section 3.4.2).

5. A simple power-law component cannot reproduce the curvature above a few keV, and an extremely low-energy cutoff ($E_{cut} \sim 3$ keV) is needed when NuSTAR data are included (see Figures 4(B) and (C)).

6. The spectral shape shows a clear relation with the luminosity, becoming harder when brighter. This is due to (i) the relative increase of the flux from the power-law component (bottom panels of Figure 13) and (ii) a higher temperature of the blackbody component (see bottom panels of Figure 8). We find that kT shows a tight dependence on the luminosity in all of our observations (Figure 9). The harder-when-brighter behavior is also clearly observed in a model-independent fashion when looking at the hardness ratios (Figure G3 in Appendix G and Figure I1 in Appendix I for XMM-Newton and NICER, respectively).

7. Two prominent features at ~1 keV and ~1.8 keV were found in the spectra (see panel (B) of Figures 2 and 4) and could be reproduced by using broad Gaussian lines. The broad feature at ~1 keV is found in all observations, with the exception of the ones in which the source was most luminous (central panels of Figure 8).

The unique characteristics of 1ES 1927+654 in the X-ray band suggests that it belongs to a new type of changing-look AGN, which underwent some catastrophic event that restructured its accretion flow. The lack of X-ray flux above 2 keV right after the detection of the optical/UV event implies that the event destroyed the X-ray corona and possibly also the innermost regions of the accretion flow. The corona appears to be in the process of being re-formed as the X-ray luminosity of the source increases. In Ricci et al. (2020), we speculated that the characteristics of 1ES 1927+654 might match what would be expected from the interaction between a tidally disrupted star with an accretion disk around an SMBH, which would empty the innermost regions of the accretion flow (Chan et al. 2019, 2020, 2021). Future observational studies and simulations will be able to better understand the link between TDEs and flaring AGNs such as 1ES 1927+654.

In a forthcoming paper (M. Masterson et al. 2021, in preparation), we will test alternative X-ray spectral models, with the goal of understanding the origin of the broad features at ~1 keV and ~1.8 keV. Soft X-ray surveys, such as the one that is currently being carried out by eROSITA (Merloni et al. 2012) or those that will be performed by the future mission Einstein Probe (Yuan et al. 2015), could potentially detect several objects like 1ES 1927+654 in the next few years.

Appendix A
Observation Log

In Table A1 we list all of the X-ray observations carried out during our follow-up campaign of 1ES 1927+654 between 2018 May 17 and 2019 August 5. For completeness, we also include the XMM-Newton observation carried out in 2011 May (PI: L. Gallo).

Table A1
X-Ray Observation Log

(1) Date and Time	(2) Observation ID	(3) Exposure (s)
XMM-Newton		
2011-05-20 06:08:25	0671860201	28600
2019-05-06 21:56:01	0843270101	52000
NuSTAR		
2018-06-05 13:06:09	90401625002	45877
2019-05-06 20:06:09	90501618002	58249
Swift/XRT		
2018-05-17 13:50:57	00010682001	2179
2019-03-28 06:54:36	00010682014	2113
NICER		
2018-05-22 19:21:20	1200190101	2156
2019-08-05 15:54:38	2200190279	424

(This table is available in its entirety in machine-readable form.)

Appendix B
The Swift/XRT Observations

The results of our spectral analysis of the 14 Swift/XRT observations of 1ES 1927+654 are reported in Table B1, while the spectra are illustrated in Figure B1. In the following, we describe the procedure adopted for the data reduction (Appendix B.1) and our spectral analysis (Appendix B.2).

B.1. XRT and UVOT Data Analysis

A total of 14 observations of 1ES 1927+654 were performed in 2018 by the X-ray Telescope (XRT, Burrows et al. 2005) and the Ultraviolet Optical Telescope (UVOT; Roming et al. 2005) on board the Neil Gehrels Swift Observatory (Gehrels et al. 2004). The typical exposures were of ∼2 ks. The data were retrieved from the High Energy Astrophysics Science Archive Research Center (HEASARC) Swift archive.[17]

For all observations, the XRT data were reduced using the XRTPIPELINE V0.13.4, which is part of the XRT Data Analysis Software within Heasoft v6.24, following the standard guidelines (Evans et al. 2009). The UVOT data were instead reduced using the UVOTIMSUM and UVOTSOURCE routines, which are a part of the FTOOLS package provided by HEASARC[18] (Blackburn 1995). The scripts were run via the Python READSWIFT pipeline written by S. Valenti on a Swift-reduction Docker container created by C. McCully. We used an aperture radius of 5″ both at the position of the event and at a nearby position with no obvious sources for sky subtraction. We did not remove host contamination, which will be part of a dedicated forthcoming publication (R. Li et al. 2021, in preparation).

B.2. Swift/XRT Spectral Analysis

The 14 Swift/XRT observations were carried out several weeks apart and show very different spectral characteristics, depending on the flux level of the source. The spectra obtained from the 14 XRT observations are shown in Figure B1 in Appendix B. During the first observation, in 2018 mid-May, the source was found to have a 0.3–2 keV luminosity of $L_{0.3-2} \simeq 10^{43}$, i.e., about a factor of 2 higher than the previous 2011 XMM-Newton observation in the same energy band (5.4×10^{42} erg s^{-1}), while the overall 0.5–10 keV flux was the same. A decline in flux was observed over the following observations, and the source was very weak in July and during the first week of 2018 August, with its 0.3–2 keV luminosity decreasing below 10^{41} erg s^{-1}. An increase in flux was then observed in the following observations, with the AGN going back to an X-ray luminosity of 10^{43} erg s^{-1} in 2018 October and showing a similar flux in 2019 March.

Due to the lower signal-to-noise ratio with respect to the XMM-Newton observations, the spectra were fitted using a model that includes a blackbody and, if it significantly improved the fit, a power-law component [TBABS×(ZBB+ZPO)]. The column density of the absorber was fixed to the Galactic value. We fitted the model using Cash statistics, similarly to what was done for the time-resolved XMM-Newton spectra (Section 3.5). The results of the spectral fitting are reported in Table B1 in Appendix B. Similarly to what was observed in the three XMM-Newton/ NuSTAR observations, the temperature of the blackbody component increases with the X-ray luminosity of the source, reaching $kT = 205^{+26}_{-24}$ eV for $L_{0.3-2} = 3.6 \times 10^{43}$ erg s^{-1}. The power-law component was observed only in the observations in which $L_{0.3-2} \gtrsim 7 \times 10^{42}$ erg s^{-1}, and the photon index varied in the range $\Gamma = 3 - 4.5$, consistent with what we found for the XMM-Newton observations.

Table B1
Spectral Parameters Obtained for the 14 Swift/XRT Observations (See Section B.2 and Figure B1)

(1) Obs. ID	(2) kT (eV)	(3) Γ	(4) C-stat/DOF	(5) $L_{0.3-2}$ (erg s^{-1})
00010682001	149 ± 10	$4.52^{+0.56}_{-0.41}$	161/129	$1.26^{+0.03}_{-0.06} \times 10^{43}$
00010682002	101^{+7}_{-6}	⋯	54/68	$2.60^{+0.15}_{-0.19} \times 10^{42}$
00010682003	105^{+10}_{-9}	⋯	47/58	$1.47^{+0.12}_{-0.15} \times 10^{42}$
00010682004	56^{+41}_{-23}	⋯	8/5	$1.40^{+0.12}_{-1.40} \times 10^{41}$
00010682005	$\geqslant 71$	⋯	13/3	$3.10^{+2.68}_{-3.10} \times 10^{41}$
00010682006	85^{+19}_{-16}	⋯	10/18	$3.31^{+0.49}_{-0.90} \times 10^{41}$
00010682007	94 ± 8	⋯	52/59	$1.62^{+0.12}_{-0.15} \times 10^{42}$
00010682008	141^{+13}_{-10}	$2.95^{+0.51}_{-0.70}$	146/128	$1.42^{+0.12}_{-0.05} \times 10^{43}$
00010682009	205^{+26}_{-23}	$3.48^{+0.37}_{-0.32}$	151/165	$3.60^{+0.13}_{-0.15} \times 10^{43}$
00010682010	159^{+13}_{-12}	$3.96^{+0.80}_{-0.70}$	126/124	$2.09^{+0.08}_{-0.09} \times 10^{43}$
00010682011	148^{+12}_{-8}	$3.11^{+0.77}_{-1.63}$	127/123	$1.68^{+0.13}_{-0.05} \times 10^{43}$
00010682012	132^{+11}_{-10}	$4.36^{+2.60}_{-4.36}$	101/104	$7.33^{+0.92}_{-0.65} \times 10^{42}$
00010682013	153^{+11}_{-7}	$3.16^{+0.46}_{-0.78}$	122/149	$2.68^{+0.18}_{-0.14} \times 10^{43}$
00010682014	182^{+10}_{-8}	$2.84^{+0.22}_{-0.27}$	214/218	$4.54 \pm 0.10 \times 10^{43}$

Note. The columns report (1) the observation ID, (2) the temperature of the blackbody component, (3) the photon index of the power-law component, (4) the C-stat and the number of DOF, and (5) the 0.3–2 keV luminosity.
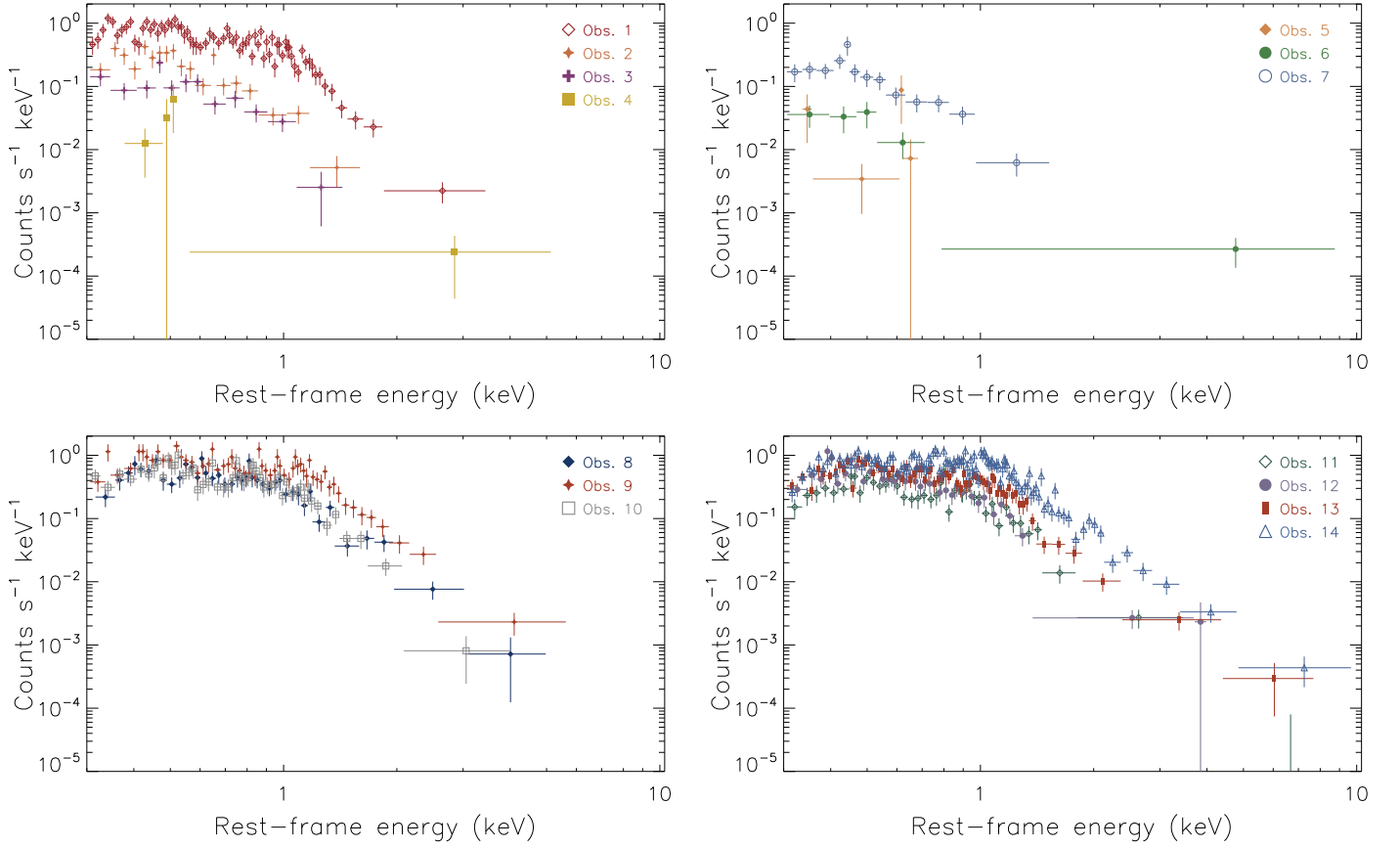

Figure B1. Swift/XRT observations of 1ES 1927+654 carried out in 2018, illustrating the dramatic variability of the source. All of the observations showed a very soft spectral shape, with very little flux above 2 keV. The source was in a very low-flux state during observations four, five, and six. Further details about the spectral analysis can be found in Appendix B.2 and Table B1.

Appendix C
The Simultaneous XMM-Newton and NICER Observation in 2018 December

NICER observed 1ES 1927+654 on 2018 December 12 (Observation ID 1200190238; see Table A1), at the same time as the second XMM-Newton observation of our campaign. This observation lasted 7.2 ks and started ∼42 ks after the beginning of the XMM-Newton observation. Given the extremely strong spectral and flux variability of the source on timescales of a few kiloseconds (see Figure 5), we could not use the NICER spectrum for our combined spectral analysis with XMM-Newton and NuSTAR. In Figure C1, we show the EPIC/PN light curve of the 2018 December observation around the NICER observation. NICER covers interval 15, 16, and 17, and part of intervals 14 and 18, all of which show significantly different spectra (see Table H2), with temperatures of the blackbody component varying between $kT \simeq 120$ eV and $kT \simeq 180$ eV, and 0.3–2 keV luminosities ranging between $\simeq 3.6 \times 10^{43}$ erg s^{-1} and $\simeq 8.2 \times 10^{43}$ erg s^{-1}.

We used this NICER observation to confirm that there were no issues related to pile-up or X-ray loading in the EPIC/PN spectrum, because the observation was carried out when the source was extremely bright. We extracted the EPIC/PN spectrum in the same interval covered by the NICER observation (blue shaded area in Figure C1) and compared the spectra and the spectral parameters obtained by fitting the two spectra with the same model. The two spectra are shown in the top panel of Figure C2. The spectral analysis was carried
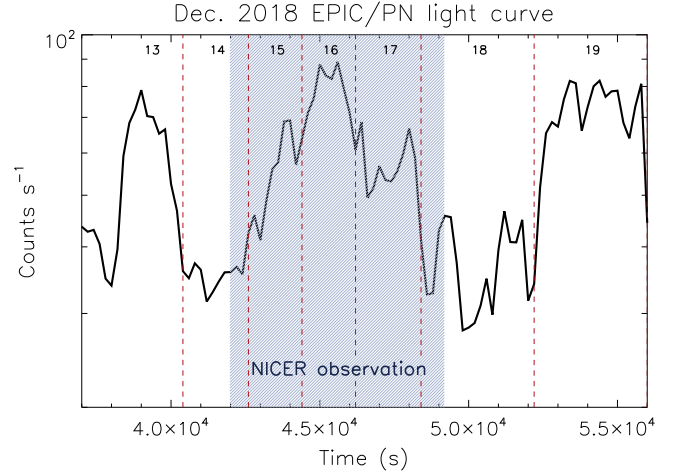
Figure C1. Extract of the 2018 December XMM-Newton EPIC/PN light curve (top-right panel of Figure 5) around the 7.2 ks NICER observation (blue shaded area). The EPIC/PN spectrum used for the comparison was extracted from that same interval.

out in the same band (0.3–3 keV) for the two spectra, and we used our best model, which includes neutral and ionized absorption, a blackbody, a power law, and two broad Gaussian lines [CONS × TBABS × ZTBABS × MTABLE{XSTAR} × (ZBB +ZPO+ZGAUSS+ZGAUSS)]. We started fitting the two data sets together, fixing the parameters of the two spectra to have the

23
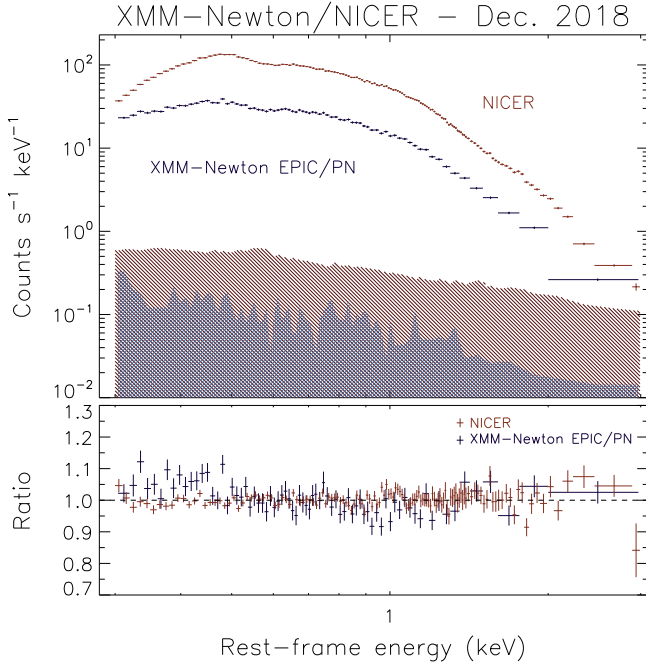
Figure C2. Top panel: 2018 December simultaneous XMM-Newton EPIC/PN (blue points) and NICER (red points) 0.3–3 keV spectra, rebinned to 30σ. The EPIC/PN was extracted from the blue shaded region of Figure C1, in order to be simultaneous with NICER. The blue and red shaded areas are the background spectra of EPIC/PN and NICER, respectively. Bottom panel: ratio between the model and the data. We fitted both data sets simultaneously, fixing all parameters to have the same values, in order to highlight possible differences.

same values, and found that the model can reproduce well the spectra ($\chi^2 = 751$ for 622 DOF); the residuals to this joint fit are illustrated in the bottom panel of Figure C2.

Next, we fitted the two spectra separately using the same model. We fixed the parameters of the second Gaussian line ($E \sim 1.92$ keV) to those obtained by the fit to the whole 2018 December XMM-Newton observation (see Section 3.2 and Table F2). The results of the fits to the NICER and XMM-Newton spectra are reported in columns 2 and 3 of Table C1, respectively. Overall EPIC/PN data are not able to constrain the parameters as well as NICER, due to the lower count rate (23.1 ct s^{-1} versus 78.6 ct s^{-1}). All parameters are consistent within their uncertainties, with the exception of the column density of the neutral absorber, which is slightly higher in the best-fit model to the XMM-Newton spectrum. The photon index obtained by fitting the XMM-Newton observation is consistent ($3.7^{+0.1}_{-0.2}$) within the uncertainties with that inferred from the NICER observation ($3.44^{+0.06}_{-0.07}$). The small difference is likely related to the $\sim$5%–10% excess observed in the 0.3–0.5 keV band in the EPIC/PN spectrum (see the bottom panel of Figure C2). The blackbody temperature is, on the other hand, very consistent between the two fits: 160 ± 1 eV and

Table C1
Spectral Parameters Obtained Fitting Individually the NICER (Column 2) and XMM-Newton EPIC/PN (column 3) Spectra Obtained during the 7.2 ks Simultaneous 2018 December Observation

		(1)	(2) NICER	(3) XMM-Newton
(a)		$N_{\rm H}$ (10^{20} cm^{-2})	$3.5^{+0.5}_{-0.7}$	$6.2^{+1.5}_{-1.8}$
(b)		$N_{\rm H}^{W}$ (10^{20} cm^{-2})	$2.0^{+0.3}_{-0.2}$	$\leqslant 2.1$
(c)		$\log \xi$ (erg cm s^{-1})	$\leqslant 1.3$	$\leqslant 3.7$
(d)		z	-0.26 ± 0.01	$-0.29^{+0.07}_{-NC}$
(e)		Γ	$3.44^{+0.06}_{-0.07}$	$3.7^{+0.1}_{-0.2}$
(f)		E_1 (keV)	1.12 ± 0.01	1.13 ± 0.05
(g)		σ_1 (eV)	113 ± 15	84^{+302}_{-44}
(h)		EW$_1$ (eV)	32 ± 3	21 ± 8
(i)		kT (eV)	160 ± 1	158^{+4}_{-5}
(j)		χ^2/DOF	339/257	341/356

Note. The model used consists of a blackbody component, a power law, two Gaussian absorption lines and two Gaussian emission lines, and neutral and an ionized absorber. The lines report the column density of the neutral absorber (a); the column density (b), ionization parameter (c) and redshift (d) of the ionized absorber; the photon index of the power-law component (e); the energy (f), width (g), and equivalent width (h) of the Gaussian emission line; the temperature of the blackbody (i); and the value of the chi-squared and the number of degrees of freedom (j).

158^{+4}_{-5} eV for the NICER and XMM-Newton observations, respectively.

Appendix D
The 2018 December NuSTAR Observations of 1ES 1927+654

Given the strong variability of 1ES 1927+654 on kilosecond timescales, we looked for potential differences between the NuSTAR spectrum obtained from the whole observations and that obtained by considering only the interval of time in which the observations were simultaneous with XMM-Newton. The spectra are illustrated Figure D1.

We fitted both spectra (Figure D1) in the 3–8 keV range using a simple power-law mode to test the differences obtained in the spectral parameters. For the complete observation (black diamonds), we obtained $\Gamma = 4.79^{+0.22}_{-0.21}$ and a normalization of $n_{\rm po} = 2.8^{+1.0}_{-0.7} \times 10^{-2}$ photons keV^{-1} cm^{-2} s^{-1}. Fitting the spectrum obtained from the interval consistent with the XMM-Newton observation (red squares), we found a very similar spectral shape ($\Gamma = 4.78^{+0.26}_{-0.25}$) and normalization ($n_{\rm po} = 3.5^{+1.5}_{-1.0} \times 10^{-2}$ photons keV^{-1} cm^{-2} s^{-1}). We concluded that, given the negligible spectral differences, it is safe to fit the XMM-Newton spectra with the NuSTAR spectrum extracted from the whole observation. We nevertheless included a constant when fitting NuSTAR and XMM-Newton data to take into account possible differences in flux and calibrations.
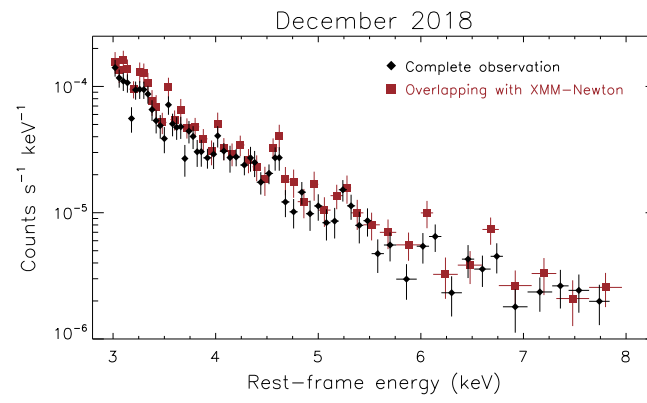
Figure D1. NuSTAR spectrum from the whole observation (black diamonds) and for the part of the observation overlapping with XMM-Newton (red squares).

Appendix E
The XMM-Newton/RGS Spectra

In this section, we show the XMM-Newton/RGS spectra of 1ES 1927+654 obtained by our campaign. In Figure E1, we illustrate the two 2018 first-order spectra, while in Figure E2, we show the 2019 May one. The second-order RGS spectra are illustrated in Figure E3.
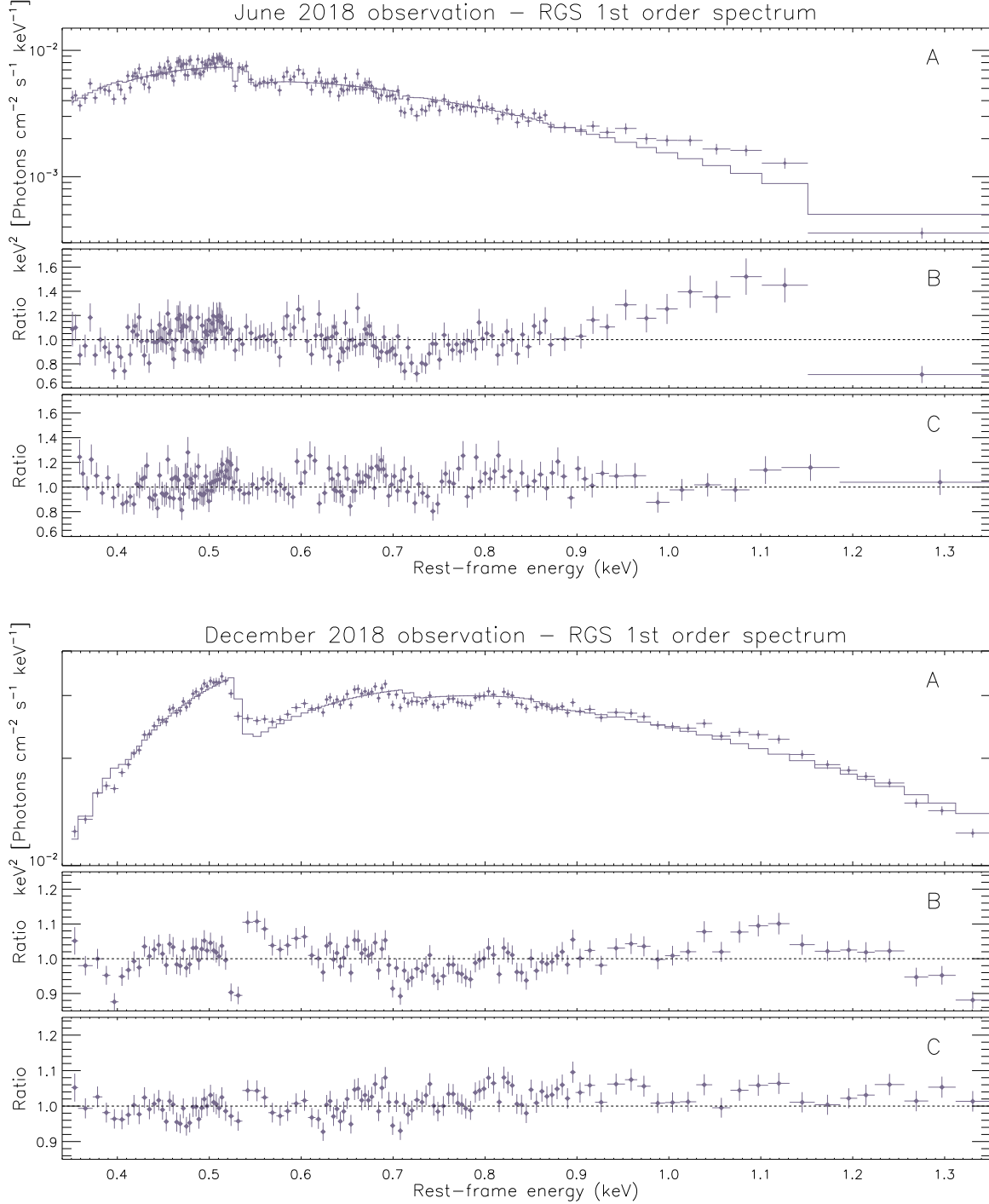
Figure E1. XMM-Newton/RGS 2018 observations. (A) First-order spectra obtained from the June (top figure) and 2018 December (bottom figure) XMM-Newton observations. For visual clarity the spectra were rebinned to 10σ and 35σ, respectively. The model for the continuum (continuous lines) includes a blackbody and a power law [ZTBABS*(ZBB+ZPOW) in XSPEC]. (B) Ratios between the model illustrated in panel (A) and the data. (C) Ratios obtained when considering the best-fitting model [TBABS×ZTBABS×MTABLE{XSTAR} (ZBB+ZPO+ZGAUSS+ZGAUSS)].
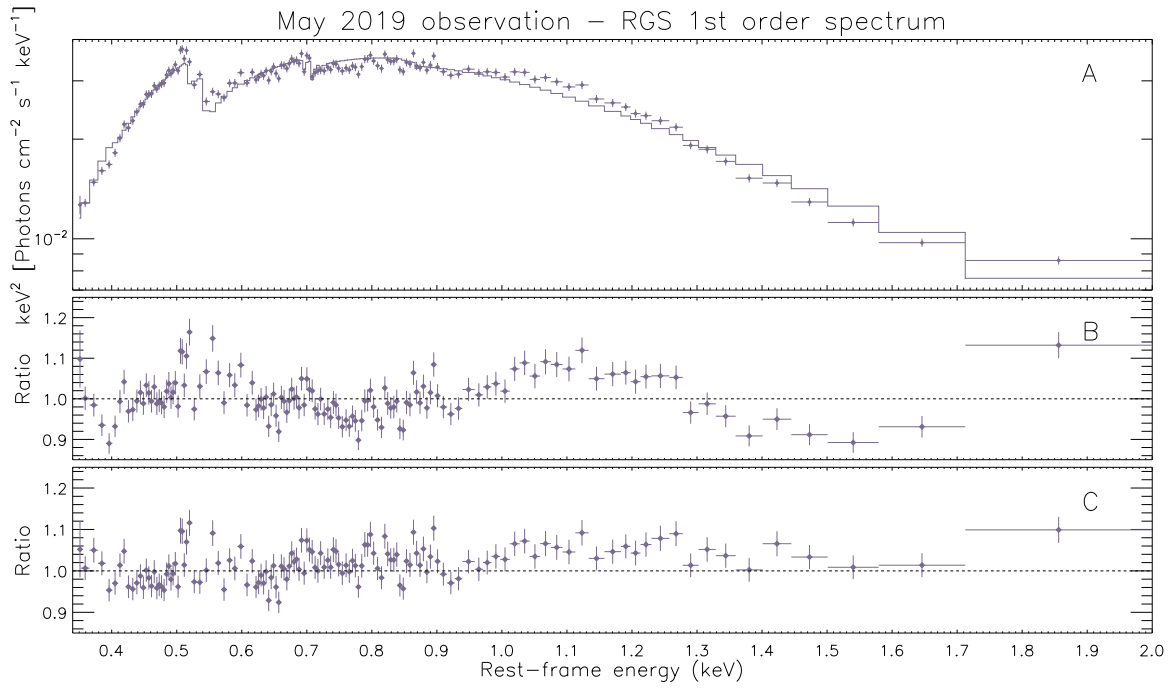
Figure E2. XMM-Newton/RGS 2019 May observations. (A) First-order spectrum of the 2019 May observation. For visual clarity, the spectra were rebinned to 35σ. The model for the continuum (continuous line) includes a blackbody and a power law [ZTBABS*(ZBB+ZPOW) in XSPEC]. (B) Ratios between the model illustrated in panel (A) and the data. (C) Ratios obtained when considering the best-fitting emission lines model [TBABS×ZTBABS×MTABLE{XSTAR}×(ZBB+ZPO+ZGAUSS +ZGAUSS)].
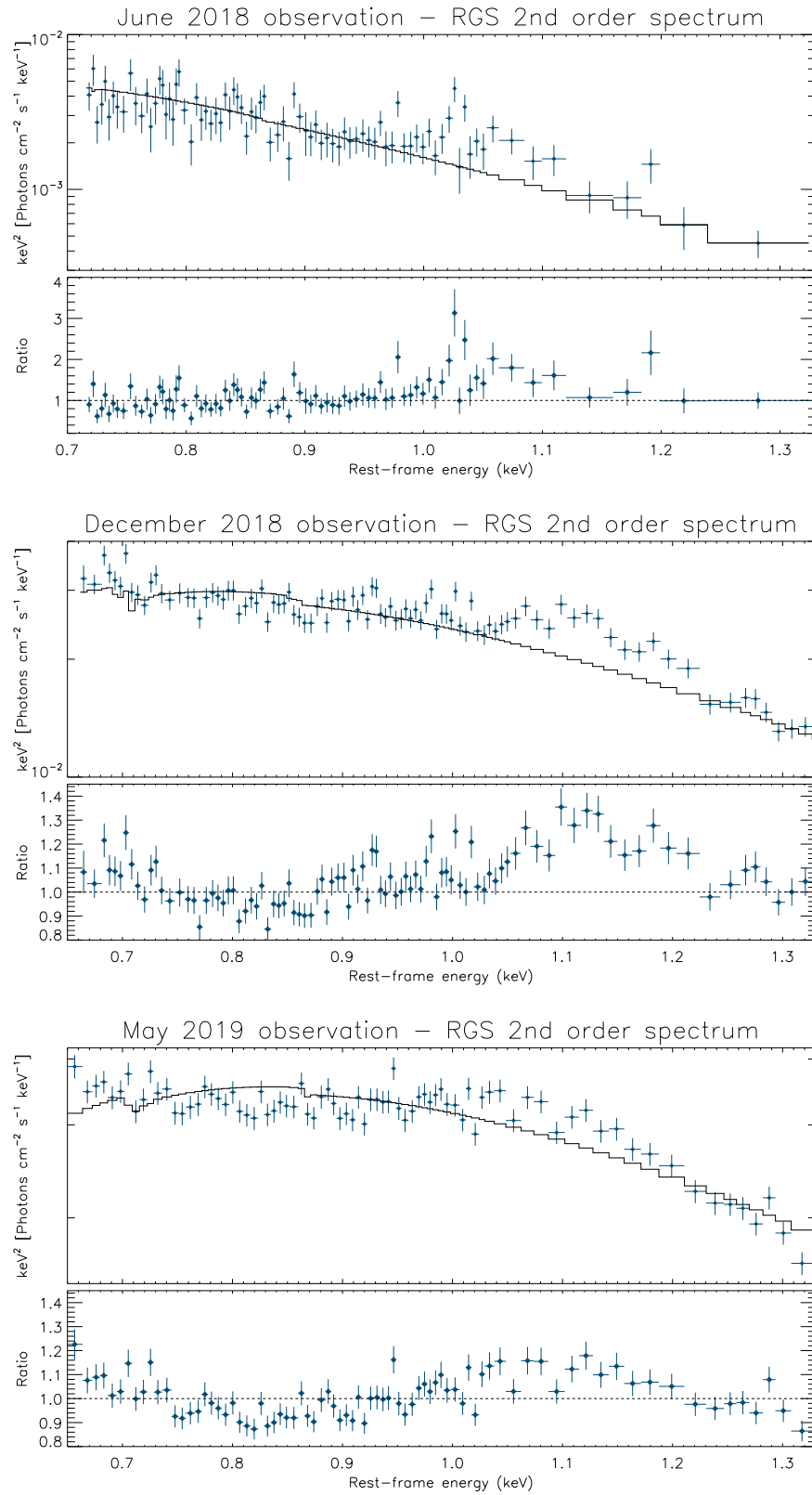
Figure E3. RGS second-order spectra obtained from the 2018 June (top panel), 2018 December (middle panel), and 2019 May (bottom panel) XMM-Newton observation. For visual clarity, the 2018 June, 2018 December, and 2019 May spectra were rebinned to 3σ, 17σ, and 17σ, respectively. The model for the continuum (black lines) includes a blackbody and a power law [ZTBABS*(ZBB+ZPOW) in XSPEC]. The bottom panels show the ratio between the model and the data.

Appendix F
Alternative Continuum Models

For the two XMM-Newton observations of 1ES 1927+654 carried out in 2018, we explored two different models of the continuum, the first including a multicolor disk model (Appendices F.1.2 and F.2.2), while the second considered a Comptonized disk model (Appendices F.1.2 and F.2.2).

F.1. The XMM-Newton 2018 June Observation

F.1.1. Multicolor Disk Model

As a first test, we adopted, instead of the blackbody component, a multicolor disk (MCD) blackbody (DISKBB in XSPEC; Mitsuda et al. 1984; Makishima et al. 1986). Because this model does not consider redshift, we used it in combination with the ZASHIFT model. The parameters of DISKBB are the same as the classical blackbody used in Section 3.1, and we left free to vary both the temperature (kT_{MCD}) and the normalization.

We started from a model that includes neutral absorption and a power-law component [CONS×TBABS×ZTBABS×(ZASHIFT×DISKBB+ZPO)] and found that, similarly to what was found in the case of the blackbody component, this model cannot reproduce well the X-ray spectrum ($\chi^2 = 1755$ for 317 DOF), leaving strong residuals in the 1–2 keV range. The addition of a Gaussian line significantly improves the fit ($\chi^2 = 538$ for 314 DOF), though still leaving residuals between 1.5 and 2 keV. Adding a second Gaussian line improves the fit and yields $\chi^2 = 480$ for 311 DOF, while adding a warm absorber to this model only marginally improved the fit ($\chi^2 = 477$ for 308 DOF). Including the RGS data to, the fit we obtained Stat = 3218 for 2847 DOF, and a temperature of the disk of $kT_{MD} = 121 \pm 1$ eV (see column 2 of Table F1). Overall, the multicolor disk model does not reproduce the X-ray spectrum of 1ES 1927+654 as well as the blackbody model.

F.1.2. Comptonized Disk Model

As a further test, we used a Comptonized disk model (COMPTT; Titarchuk 1994) to reproduce the strong soft component observed in the spectrum of 1ES 1927+654. The geometry parameter of the Comptonizing region was set to 1 (disk geometry), while the temperature of the seed photons (T_0) was assumed to follow Wien's law. The maximum effective temperature of a classic Shakura–Sunyaev accretion disk (Shakura & Sunyaev 1973; Bonning et al. 2007) is

$$kT_{max} = C \times L_{46}^{0.25}/M_8^{0.5} \text{ K} = C_1 \times L_{46}^{0.25}/M_8^{0.5} \text{ eV}, \quad \text{(F1)}$$

where L_{46} and M_8 are the bolometric luminosity and the black hole mass in units of 10^{46} erg s^{-1} and $10^8 M_\odot$, while the values of the constants are $C = 10^{5.08}$ ($C_1 = 10.4$) for a nonrotating Schwarzschild black hole and $C = 10^{5.54}$ ($C_1 = 29.9$) for a maximally rotating one. We assumed a black hole mass of $M_{BH} = 1.9 \times 10^7 M_\odot$ (Trakhtenbrot et al. 2019a), while the bolometric luminosity was calculated from the 0.3–10 keV luminosity, assuming a bolometric correction of $\kappa_X = 20$ ($L_{46} = 1.69 \times 10^{-2}$). It should be noted that this is a rather arbitrary value; in fact, because most of the X-ray radiation is emitted below 2 keV, we cannot use the typical 2–10 keV bolometric corrections (e.g., Vasudevan & Fabian 2007, 2009). From this luminosity, we obtained $kT_{max} \simeq 9$ eV for a

Table F1
Spectral Parameters Obtained for the XMM-Newton 2018 June Observation (EPIC+RGS) Using Two Models

	(1)	(2) Multicolor Disk	(3) Comptonized Disk
(a)	N_H (10^{20} cm^{-2})	3.3 ± 0.5	$1.5^{+1.1}_{-0.9}$
(b)	N_H^W (10^{20} cm^{-2})	$\leqslant 1.7$	3.6 ± 0.7
(c)	$\log \xi$ (erg cm s^{-1})	$3.0^{+0.2}_{-0.9}$	$2.7^{+0.2}_{-0.8}$
(d)	z	$-0.216^{+0.017}_{-0.018}$	$-0.191^{+0.007}_{-0.006}$
(e)	Γ	$0.7^{+0.6}_{-0.7}$	$-0.2^{+1.9}_{-2.7}$
(f)	E_1 (keV)	1.00 ± 0.01	$1.00^{+0.02}_{-0.01}$
(g)	σ_1 (eV)	92 ± 6	109^{+6}_{-8}
(h)	EW$_1$ (eV)	142^{+6}_{-9}	268^{+404}_{-206}
(i)	E_2 (keV)	$1.81^{+0.05}_{-0.04}$	$0.02^{+0.16}_{-0.02}$
(j)	σ_2 (eV)	162^{+56}_{-44}	312^{+10}_{-16}
(k)	EW$_2$ (eV)	767^{+381}_{-163}	1076^{+9436}_{-184}
(l)	C_{MOS}	1.04 ± 0.01	1.05 ± 0.01
(m)	C_{RGS}	0.92 ± 0.01	0.93 ± 0.01
(n)	kT_{MD} (eV)	122 ± 1	...
(o)	$kT_{Comp.}$	...	$5.7^{+3.1}_{-5.7}$
(p)	τ	...	$0.6^{+0.6}_{-0.3}$
(q)	Stat/DOF	3218/2847	2940/2822

Note. The two models used are: (i) a multicolor disk component, a power law, two Gaussian lines, a neutral and an ionized absorber (Column 2); and (ii) a Comptonized disk component, a power law, two Gaussian lines, and a neutral and an ionized absorber (Column 3). The table reports the column density of the neutral absorber (a); the column density (b), ionization parameter (c) and redshift (d) of the ionized absorber; the photon index of the power-law component (e); the energy (f), width (g) and equivalent width (h) of the first Gaussian line; the energy (i), width (j) and equivalent width (k) of the second Gaussian line; the cross-calibration constant of the MOS (l) and RGS (m) spectra; the temperature of the multicolor disk component (n); the temperature (o) and optical depth (p) of the Comptonized disk; and the value of the statistic and the number of degrees of freedom (q).

Schwarzschild black hole and $kT_{max} \simeq 25$ eV for a maximally rotating one. We started assuming a maximally rotating black hole and set $kT_0 = 25$ eV. Interestingly, this value is considerably lower than that inferred for 1ES 1927+654 by using a simple blackbody model. As we discussed in Section 3.6, fitting with a relativistic line model, the broad feature at ~1 keV suggests an intermediate spin, which would imply an even lower temperature.

In the fit, both the temperature ($kT_{Comp.}$) and optical depth (τ) of the Comptonizing plasma were left free to vary. A model including only the Comptonized disk fails to reproduce the shape of the continuum (χ^2/DOF = 11334/318). The addition of a power-law component [CONS×TBABS×ZTBABS×(COMPTT +ZPO)] improves the fit, but still results in a very large chi-squared ($\chi^2 = 11316$ for 316 DOF). Adding a Gaussian line improves the fit ($\chi^2 = 3467$ for 313 DOF), and the line energy is 0.561 ± 0.002 keV, while the width exceeds 200 eV, contributing to most of the X-ray emission between 0.5 and 1 keV, and improves the fit only because the COMPTT fails to reproduce the shape of the continuum above $\simeq 0.5$ keV. A second Gaussian line improves significantly the fit ($\chi^2 = 410$ for 310 DOF), and the energy (width) of the line is $0.927^{+0.002}_{-0.012}$ keV (141 ± 5 eV), similar to one of the two broad lines needed when applying the blackbody model. The addition of a warm absorber, similarly to what was done using the blackbody model (Section 3.1), further improves the fit ($\chi^2 = 340$ for 307 DOF) to a level comparable to what we obtained for the blackbody model. It should be however noted that

that, while this model can reproduce rather well the data, most of the continuum below 1 keV comes from an unrealistically large line ($\sigma = 271^{+46}_{-84}$ eV) at $E \simeq 0.2$. The results obtained applying this last model to the EPIC and RGS data are reported in column 3 of Table F1. In this last model, we left the energy of the lines completely free to vary. Considering the case of a nonrotating Schwarzschild SMBH ($kT_{\mathrm{max}} \simeq 9$ eV), we obtained very similar results, with the model failing to reproduce the continuum and needing an unrealistically broad ($\sigma \simeq 300$ eV) Gaussian line at $E < 200$ eV.

F.2. The XMM-Newton 2018 December Observation

F.2.1. Multicolor Disk Model

Following what was done for the 2018 June observation (Appendix F.1.2), we applied a multicolor disk model instead of a blackbody model [CONS×TBABS×ZTBABS×(ZASHIFT×DISKBB +ZPO)]. This resulted in a poor fit ($\chi^2/\mathrm{DOF} = 1822/567$) and was unable to reproduce correctly the NuSTAR spectrum, besides leaving strong residuals in the 1–3 keV range. This model also resulted in a low cross-calibration constant ($C_{\mathrm{Nu}} = 0.47 \pm 0.04$). Adding a Gaussian line improved the fit ($\chi^2/\mathrm{DOF} = 888/564$), still leaving however strong residuals above 1 keV and a low cross-calibration constant ($C_{\mathrm{Nu}} = 0.34 \pm 0.03$). A cutoff power-law component instead of a simple power law [CONS×TBABS×ZTBABS×(ZASHIFT×DISKBB+ZCUT)] allowed the $E \gtrsim 3$ keV part of the X-ray spectrum ($\chi^2/\mathrm{DOF} = 679/563$) to be better reproduced. We then added a warm absorber and a second Gaussian emission line [CONS×TBABS×ZTBABS×MTA-BLE{XSTAR}× (ZASHIFT×DISKBB+ZCUT+ZGAUSS+ZGAUSS)], and similarly to what was found with the other models, this yields a better fit ($\chi^2/\mathrm{DOF} = 634/557$). We then included the RGS spectrum and added two Gaussian absorption lines. Overall, the model can reproduce the X-ray spectrum of 1ES 1927+654 but not as well as the blackbody model (Stat/DOF = 4481/3712). The results of this fit are reported in column 2 of Table F2.

F.2.2. Comptonized Disk Model

The Comptonized disk model was also applied to the XMM-Newton spectrum of the 2018 December observation. Considering the higher luminosity of the source ($L_{46} = 8.8 \times 10^{-2}$), using Equation (F1), we find that the temperature of the seed photons would be $kT_0 = 37$ eV and $kT_0 = 13$ eV for a maximally rotating and Schwarzschild black hole, respectively. As done for the 2018 June observation, we started using the temperature for a maximally rotating SMBH.

Similarly to what we found for the previous XMM-Newton observation (Section F.1.2), this model cannot reproduce the spectral shape of the source. Considering a simple model including a Comptonized disk and a power-law component [CONS×TBABS×ZTBABS×(COMPTT+ZPO)] yields a chi-squared of $\chi^2 = 9048$ for 566 DOF. Strong residuals are still observed when adding a Gaussian line and, as observed for the other models, the power-law component does not reproduce correctly the curvature of the spectrum above ∼3 keV. We therefore used a cutoff power-law, which improves the fit, but still not to an acceptable level ($\chi^2/\mathrm{DOF} = 1859/562$). We included a warm absorber and a second Gaussian line, as done for the previous XMM-Newton observation. This improves the fit ($\chi^2/\mathrm{DOF} = 624/556$), but most of the emission in the

Table F2
Spectral Parameters Obtained for the XMM-Newton 2018 December Observation (EPIC+RGS) Using Two Models

	(1)	(2) Multicolor Disk	(3) Comptonized Disk
(a)	N_{H} (10^{20} cm^{-2})	$2.1^{+0.7}_{-0.4}$	3.9 ± 0.1
(b)	N_{H}^W (10^{20} cm^{-2})	$\leqslant 1.1$	$\leqslant 1.1$
(c)	$\log \xi$ (erg cm s^{-1})	$2.91^{+0.05}_{-0.4}$	$\leqslant 1.2$
(d)	z	$-0.434^{+0.007}_{-0.005}$	$-0.168^{+0.003}_{-0.004}$
(e)	Γ	2.7 ± 0.2	$0.63^{+0.03}_{-0.21}$
(f)	E_{cut}	$2.30^{+0.03}_{-0.3}$	$0.57^{+0.11}_{-0.09}$
(g)	E_1 (keV)	1.022 ± 0.004	$0.92^{+0.01}_{-0.04}$
(h)	σ_1 (eV)	175 ± 4	222^{+13}_{-2}
(i)	EW$_1$ (eV)	130^{+5}_{-4}	416^{+404}_{-206}
(j)	E_2 (keV)	1.95 ± 0.05	0.455 ± 0.002
(k)	σ_2 (eV)	$\geqslant 219$	$\geqslant 200$
(l)	EW$_2$ (eV)	88^{+10}_{-8}	274^{+NC}_{-121}
(m)	C_{Nu}	0.76 ± 0.04	0.97 ± 0.05
(n)	C_{RGS}	0.917 ± 0.004	0.92 ± 0.01
(o)	E_{abs1} (keV)	0.383 ± 0.004	0.396 ± 0.001
(p)	σ_{abs1} (eV)	56 ± 4	$0.2^{+0.5}_{-0.1}$
(q)	Strength (10^{-3})	25 ± 1	$2.7^{+11.4}_{-1.8}$
(r)	E_{abs2} (keV)	0.527 ± 0.001	0.527 ± 0.001
(s)	σ_{abs2} (eV)	0.5 ± 0.1	$0.8^{+1.0}_{-0.5}$
(t)	Strength (10^{-3})	$3.0^{+0.9}_{-0.8}$	1.0 ± 0.5
(u)	kT_{MD} (eV)	181 ± 1	⋯
(v)	$kT_{\mathrm{Comp.}}$	⋯	31.5 ± 0.2
(y)	τ	⋯	$0.97^{+0.01}_{-0.02}$
(x)	Stat/DOF	4481/3712	4152/3711

Note. The two models used are: (i) a multicolor disk component, a power law, two Gaussian absorption lines and two emission lines, and a neutral and an ionized absorber (Column 2); and (ii) a Comptonized disk component, a power law, two Gaussian absorption lines and two emission lines, and a neutral and an ionized absorber (Column 3). The lines report the column density of the neutral absorber (a); the column density (b), ionization parameter (c) and redshift (d) of the ionized absorber; the photon index (e) and cutoff (f) of the power-law component; the energy (g), width (h) and equivalent width (i) of the first Gaussian emission line; the energy (j), width (k) and equivalent width (l) of the second Gaussian line; the cross-calibration constant of the NuSTAR/FPM (m) and XMM-Newton RGS (n) spectra; the energy (o), width (p) and strength (q) of the first Gaussian absorption line; the energy (r), width (s) and strength (t) of the second Gaussian absorption line; the temperature of the multicolor disk component (u); the temperature (v) and optical depth (y) of the Comptonized disk; and the value of the statistic and the number of degrees of freedom (x).

$E \gtrsim 0.5 - 1.5$ keV interval comes from two extremely large Gaussian lines, suggesting that the model cannot really reproduce the X-ray spectrum. Considering a temperature of the seed photons of $kT_0 = 13$ eV (for a Schwarzschild black hole) does not improve the fit significantly. We used a model including two emission lines, two absorption lines, a neutral and a warm absorber, a Comptonized disk (with $kT_0 = 37$ eV), and a cutoff power law to fit all data, including the RGS spectrum. The results of this fit are reported in column 3 of Table F2.

Appendix G
The XMM-Newton Light Curves

In this appendix, we show the XMM-Newton EPIC/PN light curves of 1ES 1927+654 in different energy bands for the 2018
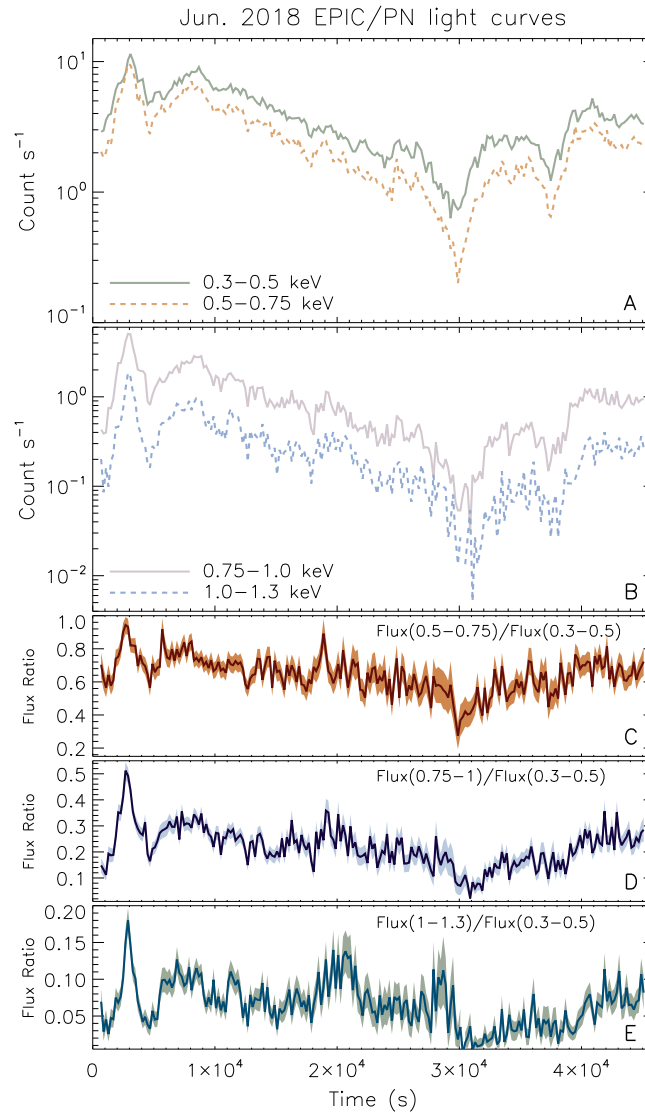
Figure G1. XMM-Newton EPIC/PN light curves and flux ratios of 1ES 1927+654 during the 2018 June observation. (A), (B) Light curves in four different energy bands, showing that the strongest variability is observed in the 0.75–1 keV (continuous pink line) and 1.0–1.3 keV (dashed cyan line) bands. (C)–(E) Ratios between the flux in three different bands and that in the 0.3–0.5 keV range.

June (Figure G1), 2018 December, and 2019 May (Figure G2) observations. The figures also show the ratio between the flux in different bands and that in the 0.3–0.5 keV interval. This illustrates how the hardness of the sources follows the same pattern as the total flux. The flux ratios in different bands versus the 0.3–10 keV count rate are illustrated for all observations in Figure G3 and clearly show that the source becomes harder when brighter.
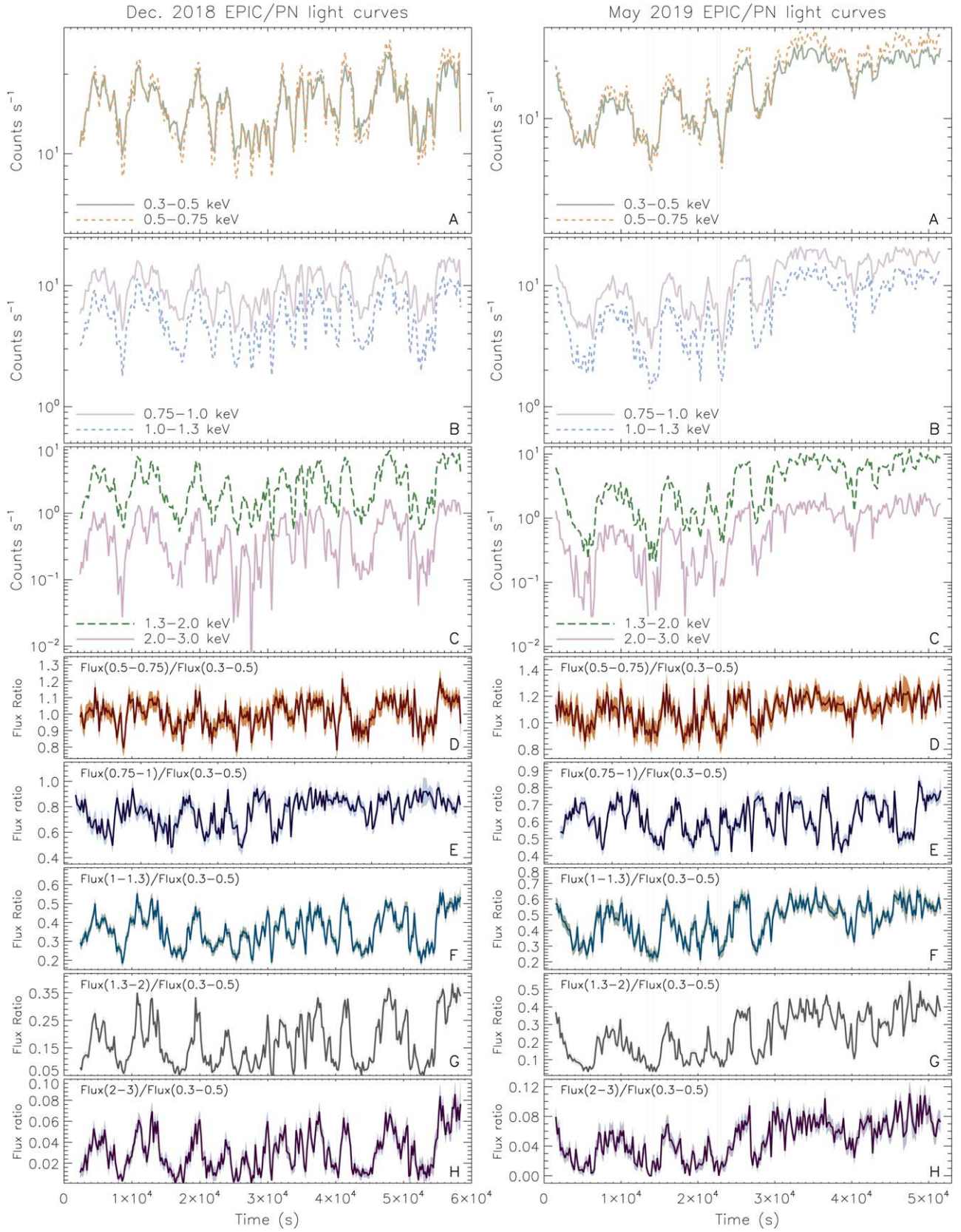
Figure G2. XMM-Newton EPIC/PN light curves and flux ratios of 1ES 1927+654 during the 2018 December (left panels) and 2019 May (right panels) observations. (A)–(C) Light curves in six different energy bands, showing that the strongest variability is observed in the 1.3–2 keV (dashed green line) and 2–3 keV (continuous pink line) bands. (D)–(H) Ratios between the flux in five different bands and that in the 0.3–0.5 keV range.
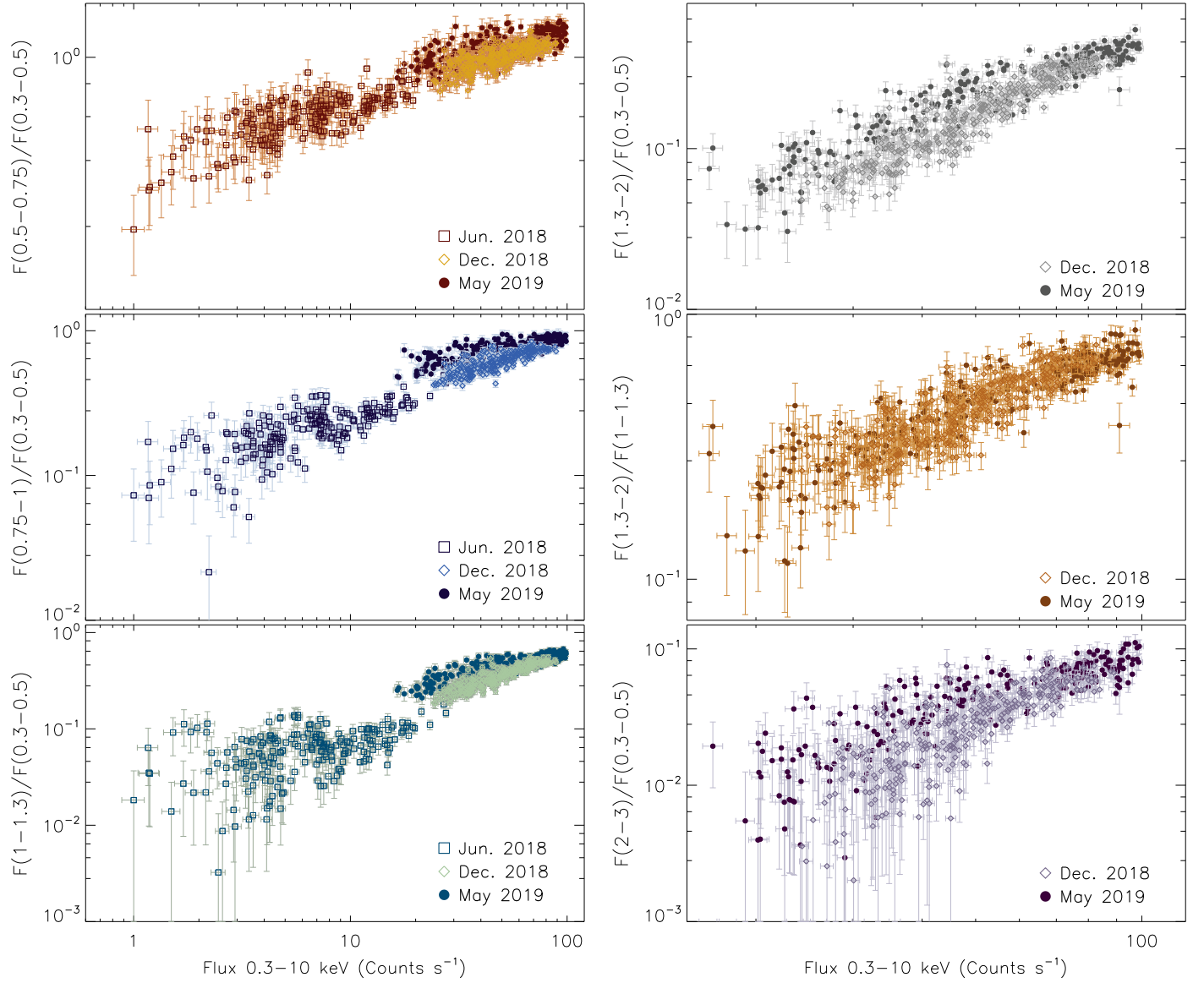
Figure G3. Left panel: XMM-Newton EPIC/PN flux ratios in different bands (0.5–0.75/0.3–0.5 keV, 0.75–1/0.3–0.5 keV and 1–1.3/0.3–0.5 keV, for the top, middle and bottom panels, respectively) vs. the 0.3–10 keV count rate for the 2018 June (empty squares), 2018 December (empty diamonds) and 2019 May (filled circles) observations. The fluxes were obtained integrating over intervals of 200 s. Right panel: same as the left panel using the 1.3–2/0.3–0.5 keV (top panel), 1.3–2/1–1.3 keV (middle panel), and 2–3/0.3–0.5 keV flux ratios for the 2018 December (empty diamonds) and 2019 May (filled circles) observations.

Appendix H
Time-resolved Spectroscopy of the 2018/2019 XMM-Newton Observations

The spectral parameters obtained by fitting the different intervals of the three XMM-Newton observations are reported in Tables H1–H3. The ratio between the XMM-Newton/RGS spectra for the low- and high-flux intervals of the 2018 June observation and a model including a blackbody and power law are illustrated in Figure H1. No clear difference is found in the residuals, suggesting that the ionized outflows do not change strongly between the two intervals.

Table H1
Spectral Parameters Obtained for the 11 Time Intervals of the XMM-Newton 2018 June Observation (See Top Panel of Figure 5)

(1) Interval	(2) $L_{0.3-2}$ (10^{43} erg s^{-1})	(3) N_H (10^{20} cm^{-2})	(4) kT (eV)	(5) Γ	(6) C-stat/DOF	(7) Energy (keV)	(8) σ (eV)	(9) EW (eV)	(10) Flux line (10^{-4} ph cm^{-2} s^{-1})
1	0.97 ± 0.01	$4.7^{+2.7}_{-2.4}$	94 ± 5	$\cdots$	193/193	$0.99^{+0.03}_{-0.04}$	84^{+29}_{-27}	202^{+50}_{-44}	$4.3^{+2.4}_{-1.6}$
2	2.30 ± 0.02	$3.8^{+2.2}_{-1.9}$	105 ± 5	$1.92^{+1.15}_{-1.09}$	231/250	$0.94^{+0.04}_{-0.05}$	125^{+28}_{-26}	288^{+56}_{-53}	28^{+15}_{-9}
3	$1.24^{+0.01}_{-0.02}$	$2.2^{+1.7}_{-1.6}$	100 ± 4	$0.75^{+1.23}_{-1.50}$	242/236	$0.97^{+0.04}_{-0.05}$	100^{+31}_{-28}	172^{+35}_{-30}	$5.6^{+3.2}_{-1.9}$
4	$1.65^{+0.01}_{-0.02}$	$1.6^{+1.3}_{-1.2}$	104 ± 3	$2.06^{+1.11}_{-1.08}$	279/284	$0.99^{+0.03}_{-0.02}$	117^{+19}_{-16}	222^{+30}_{-28}	$9.5^{+2.1}_{-2.8}$
5	$1.29^{+0.01}_{-0.03}$	$\leqslant 7.1$	100^{+4}_{-5}	$5.51^{+0.86}_{-1.80}$	229/231	$1.03^{+0.03}_{-0.06}$	91^{+43}_{-40}	186^{+41}_{-42}	$4.2^{+3.1}_{-1.7}$
6	0.79 ± 0.01	$\leqslant 1.8$	99 ± 3	$3.13^{+1.59}_{-3.00}$	259/265	$1.01^{+0.02}_{-0.03}$	117 ± 25	253^{+47}_{-48}	$3.4^{+1.0}_{-0.9}$
7	0.43 ± 0.01	$\leqslant 2.3$	93^{+3}_{-4}	$2.84^{+1.55}_{-2.94}$	248/248	$1.00^{+0.03}_{-0.04}$	127^{+35}_{-31}	316^{+85}_{-93}	$2.0^{+0.9}_{-0.6}$
8	0.20 ± 0.01	$\leqslant 7.3$	79 ± 7	$\cdots$	214/181	$1.00^{+0.07}_{-0.13}$	143^{+69}_{-41}	966^{+334}_{-178}	$1.3^{+1.2}_{-0.5}$
9	0.44 ± 0.01	$\leqslant 2.4$	89 ± 2	$3.58^{+1.45}_{-3.25}$	239/217	$0.98^{+0.04}_{-0.06}$	94^{+55}_{-42}	136^{+38}_{-53}	$0.9^{+0.7}_{-0.4}$
10	0.67 ± 0.01	$\leqslant 2.2$	99^{+2}_{-4}	$\cdots$	225/215	0.99 ± 0.04	80^{+36}_{-32}	111^{+29}_{-28}	$1.6^{+0.9}_{-0.7}$
11	0.79 ± 0.01	$\leqslant 3.9$	97 ± 5	$3.18^{+1.25}_{-1.35}$	245/266	$0.98^{+0.03}_{-0.04}$	109^{+28}_{-24}	216^{+44}_{-43}	$2.2^{+1.9}_{-1.3}$

Note. The spectral model includes a blackbody component, a power law, and a Gaussian line [TBABS×ZTBABS×(ZPO+ZBB+ZGAUSS)]. The columns report (1) the interval used for the spectral analysis, (2) the 0.3–2 keV luminosity of the source, (3) the column density of the cold absorber, (4) the temperature of the blackbody component, (5) the photon index of the power-law component, (6) the value of C-stat and the number of DOF, the (7) energy, (8) width, (9) equivalent width, and (10) flux of the Gaussian line.

Table H2
Spectral Parameters Obtained for the 19 Time Intervals of the XMM-Newton 2018 December Observation (See Middle Panel of Figure 5)

(1) Interval	(2) $L_{0.3-2}$ (10^{43} erg s^{-1})	(3) N_H (10^{20} cm^{-2})	(4) kT (eV)	(5) Γ	(6) C-stat/DOF	(7) Energy (keV)	(8) σ (eV)	(9) EW (eV)	(10) Flux line (10^{-4} ph cm^{-2} s^{-1})
1	$3.85^{+0.09}_{-0.10}$	$\leqslant 6$	125^{+12}_{-13}	$3.15^{+0.71}_{-1.03}$	337/361	$1.03^{+0.05}_{-0.10}$	158^{+63}_{-64}	221^{+89}_{-90}	33^{+42}_{-18}
2	$5.74^{+0.02}_{-0.07}$	3.8 ± 1.5	138^{+9}_{-14}	$3.36^{+0.19}_{-0.22}$	571/523	$1.03^{+0.06}_{-0.13}$	216^{+65}_{-48}	165^{+61}_{-77}	46^{+63}_{-22}
3	$3.65^{+0.03}_{-0.07}$	$3.8^{+2.6}_{-2.5}$	121^{+11}_{-13}	$3.74^{+0.41}_{-0.50}$	404/397	$0.99^{+0.05}_{-0.10}$	172^{+56}_{-49}	225^{+80}_{-85}	37^{+41}_{-17}
4	$5.93^{+0.02}_{-0.03}$	4.8 ± 1.2	155^{+4}_{-5}	$3.58^{+0.11}_{-0.10}$	738/688	$1.11^{+0.02}_{-0.03}$	126^{+27}_{-25}	69^{+12}_{-11}	18^{+7}_{-5}
5	$3.44^{+0.12}_{-0.03}$	$3.5^{+2.5}_{-2.3}$	117 ± 7	$3.52^{+0.55}_{-0.83}$	336/351	$1.02^{+0.04}_{-0.03}$	169^{+41}_{-32}	247^{+81}_{-79}	31^{+20}_{-11}
6	$5.63^{+0.03}_{-0.07}$	8.8 ± 2.1	132^{+10}_{-9}	$3.70^{+0.20}_{-0.22}$	459/509	$1.10^{+0.05}_{-0.07}$	145^{+49}_{-38}	102^{+33}_{-34}	26^{+22}_{-11}
7	$4.10^{+0.03}_{-0.13}$	$\leqslant 3.1$	129^{+7}_{-8}	$3.06^{+0.47}_{-0.59}$	363/437	$1.07^{+0.03}_{-0.05}$	142^{+43}_{-33}	181^{+57}_{-28}	25^{+16}_{-8}
8	$4.96^{+0.03}_{-0.08}$	$5.9^{+2.2}_{-2.1}$	130^{+10}_{-13}	$3.73^{+0.23}_{-0.26}$	413/465	$1.03^{+0.07}_{-0.12}$	180^{+64}_{-51}	133^{+58}_{-77}	33^{+45}_{-17}
9	3.49 ± 0.02	$2.5^{+1.4}_{-1.3}$	129^{+6}_{-7}	$3.46^{+0.19}_{-0.21}$	505/541	$1.00^{+0.03}_{-0.05}$	175^{+28}_{-24}	201^{+39}_{-41}	32^{+15}_{-9}
10	$5.69^{+0.04}_{-0.06}$	$4.8^{+2.6}_{-2.5}$	149^{+10}_{-8}	$3.42^{+0.22}_{-0.24}$	553/504	$1.06^{+0.04}_{-0.06}$	113^{+45}_{-32}	67^{+23}_{-22}	20^{+15}_{-8}
11	5.65 ± 0.02	3.5 ± 1.3	152^{+4}_{-5}	3.34 ± 0.13	566/526	1.11 ± 0.03	119^{+34}_{-32}	46^{+11}_{-12}	11^{+5}_{-4}
12	4.46 ± 0.04	2.6 ± 2.3	140 ± 7	$3.62^{+0.28}_{-0.34}$	425/447	$1.10^{+0.03}_{-0.04}$	115^{+39}_{-32}	116 ± 27	18^{+10}_{-6}
13	$6.47^{+0.03}_{-0.05}$	$6.6^{+2.0}_{-1.9}$	157^{+6}_{-7}	$3.70^{+0.15}_{-0.16}$	536/562	$1.16^{+0.03}_{-0.04}$	72^{+47}_{-37}	34^{+10}_{-11}	9^{+6}_{-4}
14	$3.62^{+0.05}_{-0.06}$	$2.6^{+2.6}_{-2.3}$	120^{+9}_{-11}	$3.66^{+0.49}_{-0.71}$	342/378	$1.01^{+0.06}_{-0.10}$	184^{+55}_{-43}	257^{+85}_{-99}	35^{+37}_{-15}
15	$5.52^{+0.03}_{-0.06}$	$7.0^{+2.4}_{-2.3}$	142^{+7}_{-9}	$3.81^{+0.22}_{-0.21}$	417/489	$1.09^{+0.05}_{-0.07}$	131^{+55}_{-39}	61^{+24}_{-27}	16^{+16}_{-8}
16	8.16 ± 0.05	$6.3^{+2.0}_{-1.9}$	177 ± 5	3.57 ± 0.15	506/557	$\cdots$	$\cdots$	$\cdots$	$\cdots$
17	$5.99^{+0.03}_{-0.04}$	3.7 ± 2.1	159^{+7}_{-8}	$3.37^{+0.18}_{-0.20}$	553/554	1.12 ± 0.04	88^{+61}_{-50}	36^{+11}_{-13}	9^{+8}_{-5}
18	$3.80^{+0.03}_{-0.07}$	$\leqslant 2.9$	128^{+6}_{-7}	$3.05^{+0.48}_{-0.63}$	363/386	$1.02^{+0.03}_{-0.05}$	151^{+33}_{-29}	181^{+38}_{-39}	27^{+15}_{-9}
19	7.42 ± 0.04	4.0 ± 1.5	175 ± 4	$3.28^{+0.13}_{-0.14}$	465/477	$\cdots$	$\cdots$	$\cdots$	$\cdots$

Note. The spectral model includes a blackbody component, a power law and a Gaussian line [TBABS×ZTBABS×(ZPO+ZBB+ZGAUSS)]. The columns report (1) the interval used for the spectral analysis, (2) the 0.3–2 keV luminosity of the source, (3) the column density of the cold absorber, (4) the temperature of the blackbody component, (5) the photon index of the power-law component, (6) the value of C-stat and the number of DOF, the (7) energy, (8) width, (9) equivalent width, and (10) flux of the Gaussian line.

Table H3
Spectral Parameters Obtained for the 13 Time Intervals of the XMM-Newton 2019 May Observation (See Bottom Panel of Figure 5)

(1) Interval	(2) $L_{0.3-2}$ (10^{43} erg s^{-1})	(3) N_H (10^{20} cm^{-2})	(4) kT (eV)	(5) Γ	(6) C-stat/DOF	(7) Energy (keV)	(8) σ (eV)	(9) EW (eV)	(10) Flux line (10^{-4} ph cm^{-2} s^{-1})
1	$5.45^{+0.04}_{-0.07}$	$5.7^{+3.2}_{-3.1}$	158^{+10}_{-14}	$3.65^{+0.23}_{-0.25}$	423/495	$1.04^{+0.09}_{-0.06}$	149^{+60}_{-51}	83^{+36}_{-40}	25^{+29}_{-13}
2	$2.72^{+0.01}_{-0.08}$	$3.1^{+2.8}_{-2.6}$	118 ± 8	$3.32^{+0.49}_{-0.51}$	350/384	1.00 ± 0.03	137^{+24}_{-21}	332^{+70}_{-59}	34^{+13}_{-9}
3	$4.51^{+0.02}_{-0.04}$	4.8 ± 1.8	148 ± 8	3.58 ± 0.15	674/605	$1.04^{+0.04}_{-0.05}$	154^{+33}_{-29}	126 ± 30	28^{+15}_{-9}

Table H3
(Continued)

(1) Interval	(2) $L_{0.3-2}$ $(10^{43}\,\mathrm{erg\,s^{-1}})$	(3) N_H $(10^{20}\,\mathrm{cm^{-2}})$	(4) kT (eV)	(5) Γ	(6) C-stat/DOF	(7) Energy (keV)	(8) σ (eV)	(9) EW (eV)	(10) Flux line $(10^{-4}\,\mathrm{ph\,cm^{-2}\,s^{-1}})$
4	$2.52^{+0.01}_{-0.11}$	$\leqslant 4.7$	121^{+10}_{-14}	$3.35^{+0.46}_{-0.25}$	427/386	$0.96^{+0.05}_{-0.08}$	164^{+47}_{-35}	285^{+85}_{-89}	32^{+30}_{-12}
5	$5.26^{+0.02}_{-0.07}$	6.8 ± 2.2	136^{+11}_{-13}	$3.67^{+0.17}_{-0.18}$	537/548	$1.01^{+0.03}_{-0.05}$	151^{+27}_{-32}	161^{+44}_{-42}	47^{+26}_{-15}
6	$3.54^{+0.02}_{-0.03}$	5.3 ± 1.7	127^{+7}_{-8}	$3.77^{+0.18}_{-0.19}$	533/538	$1.01^{+0.03}_{-0.04}$	152^{+25}_{-22}	213^{+25}_{-35}	35^{+14}_{-9}
7	$7.80^{+0.09}_{-0.06}$	6.8 ± 2.3	173^{+7}_{-8}	$3.58^{+0.16}_{-0.17}$	543/603	$1.17^{+0.07}_{-0.11}$	$\leqslant 143$	15^{+7}_{-6}	5^{+8}_{-3}
8	$4.54^{+0.03}_{-0.08}$	$4.6^{+2.4}_{-2.3}$	134^{+13}_{-22}	$3.67^{+0.21}_{-0.22}$	482/490	$0.96^{+0.06}_{-0.14}$	185^{+72}_{-49}	159^{+58}_{-86}	42^{+76}_{-21}
9	$7.78^{+0.04}_{-0.07}$	$10.0^{+2.7}_{-2.6}$	150^{+11}_{-18}	$3.68^{+0.17}_{-0.18}$	524/573	$1.00^{+0.07}_{-0.13}$	143^{+84}_{-55}	51^{+26}_{-30}	30^{+59}_{-17}
10	$9.63^{+0.04}_{-0.05}$	$6.8^{+1.3}_{-1.2}$	183^{+4}_{-3}	3.56 ± 0.09	826/784	$\leqslant 1.29$	NC	$\leqslant 9$	$\leqslant 6.3$
11	$7.28^{+0.03}_{-0.07}$	$5.6^{+2.1}_{-2.2}$	158^{+8}_{-11}	$3.48^{+0.18}_{-0.19}$	493/502	$1.09^{+0.06}_{-0.10}$	143^{+69}_{-57}	54^{+27}_{-28}	18^{+25}_{-10}
12	8.18 ± 0.08	4.5 ± 1.8	155^{+10}_{-18}	$3.27^{+0.17}_{-0.16}$	543/524	$\leqslant 1.05$	$\geqslant 142$	$\leqslant 130$	55^{+70}_{-41}
13	$9.86^{+0.14}_{-0.27}$	4.0 ± 1.6	167^{+13}_{-11}	$3.10^{+0.15}_{-0.16}$	555/534	$\geqslant 1.00$	$\geqslant 124$	$\leqslant 111$	31^{+48}_{-26}

Note. The spectral model includes a blackbody component, a power law and a Gaussian line [TBABS×ZTBABS×(ZPO+ZBB+ZGAUSS)]. The columns report (1) the interval used for the spectral analysis, (2) the 0.3–2 keV luminosity of the source, (3) the column density of the cold absorber, (4) the temperature of the blackbody component, (5) the photon index of the power-law component, (6) the value of C-stat and the number of DOF, the (7) energy, (8) width, (9) equivalent width, and (10) flux of the Gaussian line.
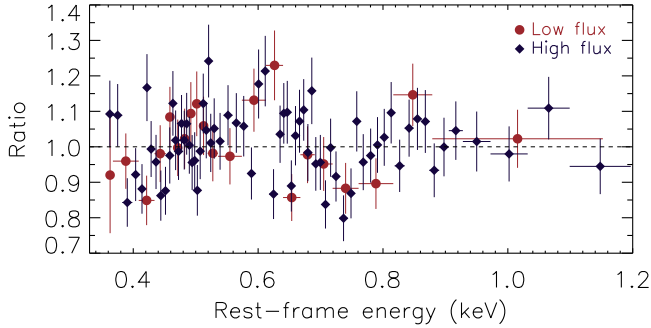

Figure H1. Ratio between the XMM-Newton/RGS spectra for the low- (red circles) and high- flux (black diamonds) intervals of the 2018 June observation and a model that considers a blackbody and power law (see Section 3.5.1). For visual clarity, both spectra have been rebinned to 12σ.

Figure I1. Hardness ratio of NICER observations, showing the same harder-when-brighter behavior observed in the XMM-Newton observations.

Appendix I
Hardness Ratio of NICER Observations

In Figure I1, we illustrate the ratio between the 0.5–1 keV and the 1–2 keV flux versus the 0.5–2 keV luminosity. The figure shows a well-defined harder-when-brighter behavior.
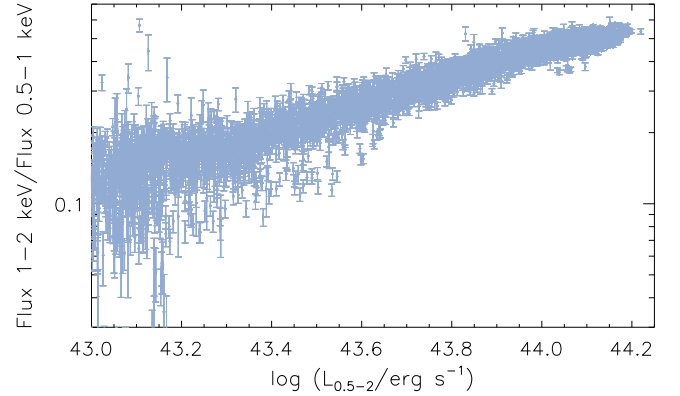
Appendix J
Stacked NICER Spectra

The spectral parameters obtained by fitting the 16 stacked NICER spectra are reported in Table J1. The fits include either only a blackbody (*bb*), a blackbody plus a cutoff power-law component (*cut* in the table) or a blackbody plus a thermally

Table J1
Spectral Parameters Obtained by Fitting the Stacked NICER Spectra

(1) Interval	(2) Dates (YY/MM/DD)	(3) Model	(4) N_H (10^{20} cm^{-2})	(5) kT (eV)	(6) Γ	(7) E_{cut} keV	(8) kT_e keV	(9) Energy (keV)	(10) σ (eV)	(11) $L_{0.3-2}$ (10^{43} erg s^{-1})	(12) χ^2/DOF
1	18/5/22–18/6/7	bb	$0.6^{+0.2}_{-0.3}$	99^{+3}_{-2}	...	...	...	$0.95^{+0.01}_{-0.02}$	157^{+8}_{-6}	0.9	113/92
2	18/6/9–18/7/1	bb	$0.8^{+0.6}_{-0.5}$	97 ± 2	...	...	...	0.99 ± 0.03	83^{+36}_{-38}	0.11	97/82
3	18/7/4–18/7/2	bb	$11.1^{+9.3}_{-7.4}$	64^{+12}_{-11}	...	...	...	...	...	0.05	127/116
4	18/8/3–18/8/20	bb	$1.0^{+0.8}_{-0.9}$	91^{+3}_{-3}	...	...	...	0.98 ± 0.15	NC	0.12	118/104
5	18/9/7–18/10/8	po	$\leqslant 2.3$	111 ± 3	2.1 ± 0.7	...	...	0.97 ± 0.01	148^{+9}_{-8}	1.1	180/141
		nth	$\leqslant 2.8$	111 ± 3	$2^{+0.8}_{-0.4}$	...	NC	0.97 ± 0.01	148^{+9}_{-8}	1.1	180/140
6	18/10/10–18/10/31	po	0.8 ± 0.7	134 ± 2	3.25 ± 0.07	...	...	1.01 ± 0.01	155 ± 6	2.7	287/191
		nth	1.3 ± 0.7	119 ± 2	$3.17^{+0.10}_{-0.08}$	...	NC	0.98 ± 0.01	172 ± 6	2.7	239/190
7	18/11/1–18/11/29	po	$\leqslant 1.3$	116 ± 2	2.50 ± 0.12	...	...	0.97 ± 0.01	175 ± 5	1.7	225/191
		nth	$0.6^{+0.8}_{-0.4}$	115 ± 2	$2.54^{+0.11}_{-0.19}$	...	NC	0.97 ± 0.1	176^{+3}_{-4}	1.7	225/190
8	18/12/1–18/12/31	po	$0.7^{+0.7}_{-0.6}$	135 ± 2	3.22 ± 0.05	...	...	1.00 ± 0.01	158^{+6}_{-5}	2.7	226/161
		nth	$0.8^{+0.7}_{-0.5}$	118 ± 2	$3.51^{+0.30}_{-0.04}$	...	NC	0.98 ± 0.01	173 ± 5	2.7	214/160
9	19/1/4–19/1/30	cut	$\leqslant 1.6$	122^{+7}_{-5}	$2.4^{+0.6}_{-0.7}$	$1.8^{+2.5}_{-0.7}$	...	0.97 ± 0.02	183^{+12}_{-13}	2.5	262/240
		nth	$1.0^{+1.0}_{-0.9}$	114^{+1}_{-1}	$3.22^{+0.4}_{-0.03}$	...	NC	$0.96^{+0.01}_{-0.01}$	187^{+8}_{-8}	2.5	260/240
10	19/2/1–19/2/26	cut	0.8 ± 0.4	136^{+2}_{-2}	1.54 ± 0.11	0.88 ± 0.04	...	1.00 ± 0.01	206^{+9}_{-6}	6.2	391/340
		nth	1.4 ± 0.4	121 ± 1	$3.44^{+0.2}_{-0.08}$	...	NC	0.99 ± 0.01	199^{+45}_{-4}	6.2	486/340
11	19/3/5–19/3/30	cut	$\leqslant 1.5$	126 ± 2	$0.8^{+0.5}_{-0.3}$	$0.72^{+0.13}_{-0.07}$	...	0.95 ± 0.02	227^{+9}_{-11}	5.3	455/340
		nth	1.2 ± 0.8	121^{+3}_{-2}	$3.26^{+0.03}_{-0.04}$	...	NC	0.96 ± 0.01	209 ± 7	5.3	513/340
12	19/4/3–19/4/30	cut	$0.9^{+0.9}_{-0.8}$	131^{+7}_{-4}	$1.1^{+0.4}_{-0.3}$	$0.68^{+0.09}_{-0.06}$	...	0.98 ± 0.02	216^{+13}_{-16}	6.9	352/340
		nth	$1.3^{+0.9}_{-0.8}$	117 ± 4	$3.67^{+0.04}_{-0.11}$	...	NC	1.00 ± 0.01	190^{+10}_{-9}	6.9	405/340
13	19/5/2–19/5/31	cut	1.5 ± 0.5	132^{+2}_{-4}	$1.27^{+0.21}_{-0.14}$	$0.79^{+0.07}_{-0.04}$	...	0.98 ± 0.01	221^{+7}_{-9}	6.8	500/440
		nth	2.1 ± 0.5	119 ± 2	$3.47^{+0.12}_{-0.09}$	...	NC	0.99 ± 0.01	202 ± 5	6.8	669/440
14	19/6/01–2019/6/29	cut	$\leqslant 0.8$	156^{+4}_{-5}	$1.52^{+0.09}_{-0.10}$	0.88 ± 0.04	...	1.00 ± 0.02	206^{+13}_{-12}	9.1	446/440
		nth	$0.9^{+0.5}_{-0.4}$	120^{+2}_{-3}	$3.56^{+0.12}_{-0.2}$	...	NC	0.99 ± 0.01	200 ± 7	9.1	514/440
15	19/7/1–19/7/29	cut	$\leqslant 0.8$	167 ± 3	1.58 ± 0.07	0.91 ± 0.03	...	1.03 ± 0.01	184^{+12}_{-11}	9.8	500/440
		nth	1.0 ± 0.5	126^{+2}_{-2}	3.56 ± 0.01	...	NC	1.02 ± 0.01	185^{+6}_{-7}	9.8	601/440
16	19/8/1–19/8/5	cut	$\leqslant 1.0$	182^{+4}_{-5}	$1.71^{+0.12}_{-0.06}$	$1.02^{+0.07}_{-0.05}$	...	1.06 ± 0.03	156^{+30}_{-24}	11.6	452/440
		nth	$\leqslant 1.0$	133^{+2}_{-5}	3.50 ± 0.03	...	NC	$1.05^{+0.01}_{-0.02}$	186^{+19}_{-16}	11.6	501/440

Note. The columns report (1) the interval number; (2) the range of dates for which the NICER spectra were stacked; (3) the model applied, which include only a blackbody component plus a Gaussian line (*bb*), a blackbody, a Gaussian line, and either a power law [*po*; TBABS×ZTBABS×(ZPO+ZBB+ZGAUSS)], a cutoff power law [*cut*; TBABS×ZTBABS×(ZCUT+ZBB+ZGAUSS)], or a thermally Comptonized plasma [*nth*; TBABS×ZTBABS×(NTHCOMP+ZBB+ZGAUSS)]. In the latter model, the temperature of the seed photons was fixed to the temperature of the blackbody component; (4) the column density of the cold absorber; (5) the temperature of the blackbody component; (6) the photon index of the power-law or thermally Comptonized continuum; (7) the cutoff energy; (8) the temperature of the electrons; the (9) energy and (10) width of the Gaussian line; (11) the 0.3–2 keV luminosity of the source; and (12) the chi-squared and the number of degrees of freedom. NC: not constrained.

Comptonized continuum (*nth*). For the latter model, we fixed the temperature of the seed photons to that of the blackbody component.

Appendix K
The 2011 May XMM-Newton Observation of 1ES 1927+654

The XMM-Newton EPIC/PN data of the 2011 May observation were reduced following the same guidelines outlined in Section 2.1. The spectrum was fitted with a model that included a power law, a blackbody, and neutral absorption, which yields a good fit (χ^2/DOF = 1727/1674, see top panel of Figure K1). The source is highly variable (see the bottom panel of Figure K1), and we divided the observation into 14 intervals, with exposures between ~1 ks and 4 ks, similarly to what we did for the 2018 and 2019 observations. We fitted all of the exposures using the same model adopted for the complete X-ray observation and report the results in Table K1. No clear relation was found between the temperature of the blackbody and the luminosity of the source. The relation between the hardness ratios and the total flux is shown in Figure K2.
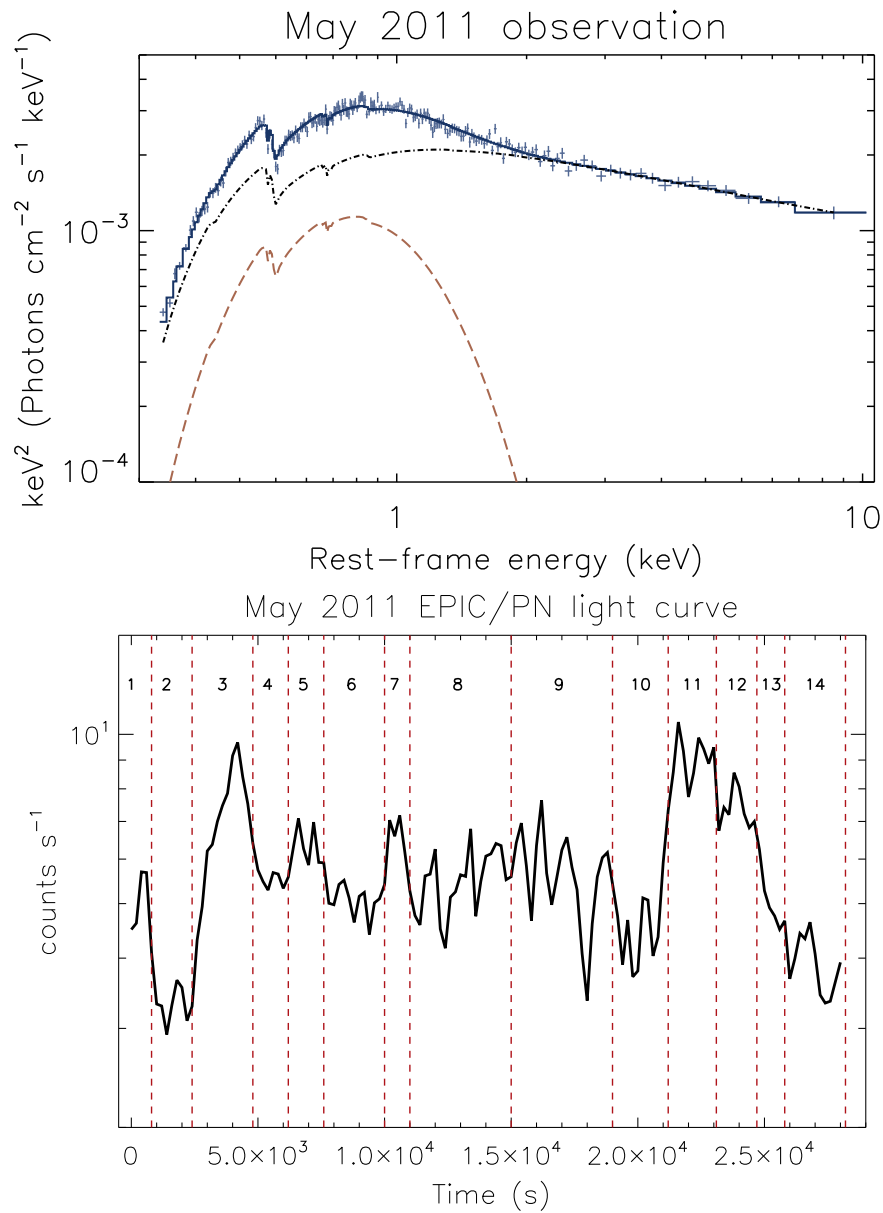
Figure K1. Top panel: 2011 May XMM-Newton EPIC/PN spectrum of 1ES 1927+654. The continuous lines show the best-fitting model, which includes a blackbody (dashed red line), and a power law (black dotted–dashed line), absorbed by low-column-density neutral gas. Bottom panel: 2011 May XMM-Newton EPIC/PN light curve of 1ES 1927+654. The figure also shows the intervals used for the time-resolved spectroscopy, which are denoted by the vertical red dashed lines. The results of the spectral analysis of these intervals are reported in Table K1.

2011 *XMM-Newton* observation
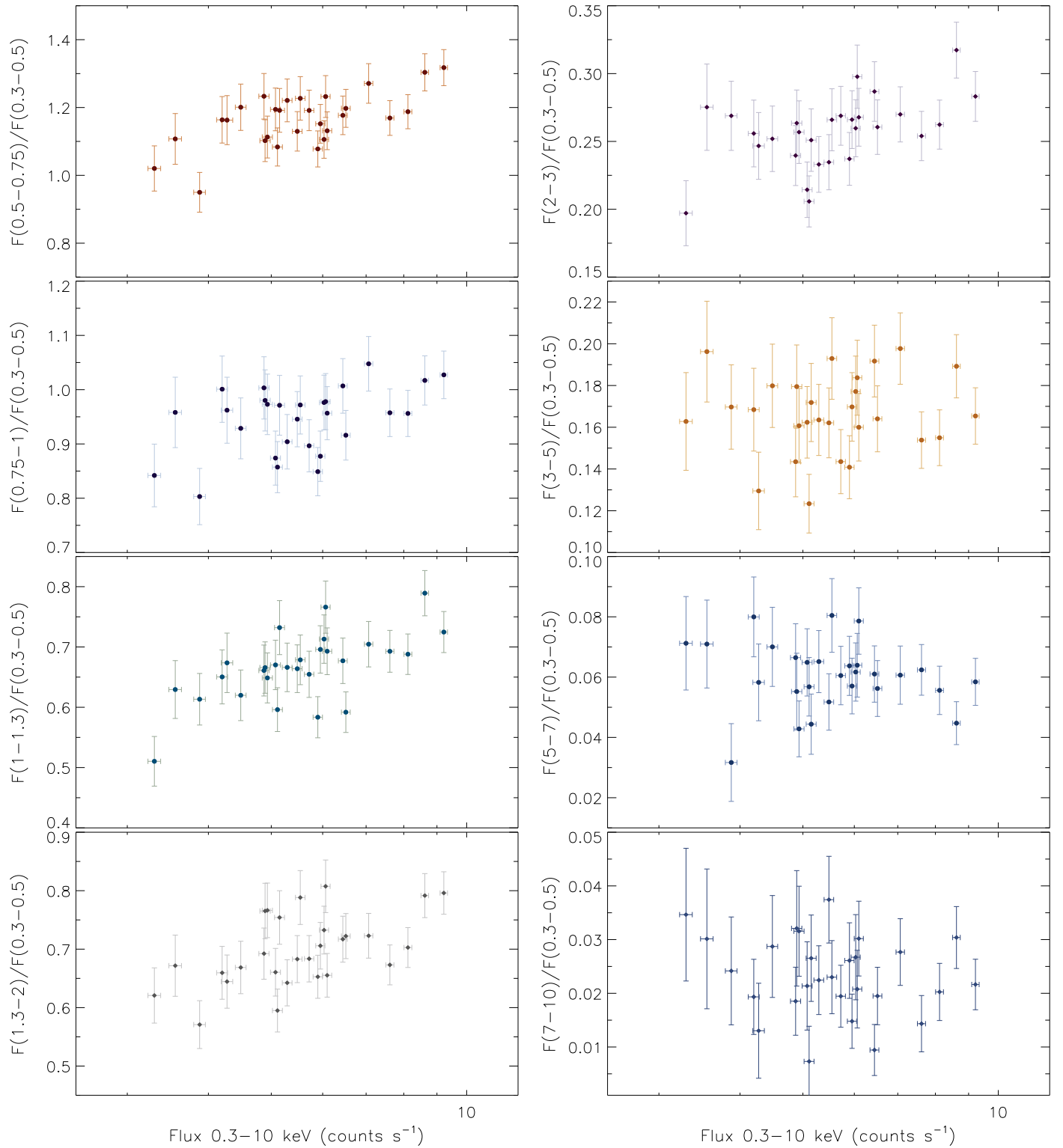
Figure K2. EPIC/PN flux ratios in different energy bands vs. the total 0.3–10 keV flux for the 2011 XMM-Newton observation of 1ES 1927+654. The fluxes were obtained integrating over intervals of 1 ks.

Table K1
Spectral Parameters Obtained for the 14 Time Intervals of the XMM-Newton 2011 May Observation (See Bottom Panel of Figure K1)

(1) Interval	(2) $L_{0.3-2}$ (10^{42} erg s^{-1})	(3) N_{H} (10^{20} cm^{-2})	(4) kT (eV)	(5) Γ	(6) C-stat/DOF
1	$5.25^{+0.08}_{-0.35}$	$\leqslant 6.7$	208^{+43}_{-55}	$2.43^{+0.30}_{-0.16}$	535/582
2	$3.48^{+0.06}_{-0.08}$	$\leqslant 1.8$	171^{+26}_{-17}	$2.35^{+0.13}_{-0.15}$	573/659
3	$7.00^{+0.06}_{-0.11}$	2.6 ± 2.2	182 ± 20	2.42 ± 0.14	808/924
4	$5.66^{+0.05}_{-0.27}$	$7.1^{+4.4}_{-3.6}$	141^{+27}_{-22}	2.52 ± 0.17	629/716
5	$6.36^{+0.06}_{-0.17}$	$\leqslant 6.3$	171^{+32}_{-31}	$2.43^{+0.19}_{-0.21}$	667/750
6	$5.30^{+0.05}_{-0.14}$	$\leqslant 3.9$	180^{+22}_{-25}	$2.46^{+0.17}_{-0.12}$	688/797
7	$6.53^{+0.06}_{-0.22}$	$7.5^{+4.3}_{-3.7}$	147^{+33}_{-28}	$2.65^{+0.20}_{-0.21}$	511/631
8	$5.61^{+0.04}_{-0.07}$	$3.7^{+2.0}_{-1.9}$	170 ± 19	$2.49^{+0.11}_{-0.12}$	831/998
9	$5.80^{+0.04}_{-0.07}$	3.9 ± 2.0	180 ± 22	2.51 ± 0.12	864/987
10	$4.74^{+0.04}_{-0.13}$	$\leqslant 4.4$	181^{+23}_{-24}	$2.40^{+0.17}_{-0.14}$	645/764
11	$9.08^{+0.07}_{-0.17}$	6.3 ± 2.3	156^{+23}_{-20}	2.58 ± 0.12	725/897
12	$7.62^{+0.06}_{-0.20}$	$7.1^{+3.0}_{-2.7}$	144^{+23}_{-20}	2.62 ± 0.14	600/785
13	$5.42^{+0.02}_{-0.56}$	$\leqslant 3.5$	182^{+19}_{-31}	$2.30^{+0.22}_{-0.08}$	601/650
14	$4.00^{+0.04}_{-0.11}$	$\leqslant 5.5$	170^{+22}_{-23}	2.36 ± 0.18	704/782

Note. The spectral model includes a blackbody component and a power law, both absorbed by neutral gas [TBABS×ZTBABS×(ZPO+ZBB)]. The columns report (1) the interval used for the spectral analysis, (2) the 0.3–2 keV luminosity of the source, (3) the column density of the cold absorber, (4) the temperature of the blackbody component, (5) the photon index of the power-law component, and (6) the value of C-stat and the number of DOF.

Appendix L
NICER Spectra

All of the NICER spectra used in our analysis are reported in Figure L1. The shaded area in the top panels represent the background, while the bottom panels illustrate the ratio between the best-fitting model (continuous lines in the middle panel) and the data. During the low-luminosity periods, no power-law component is needed to reproduce the spectra, which is well fit by a blackbody component (dashed line) and a Gaussian line (dotted–dashed line). In the high-luminosity intervals, the power-law component (dotted–dotted–dashed line) can be observed again.
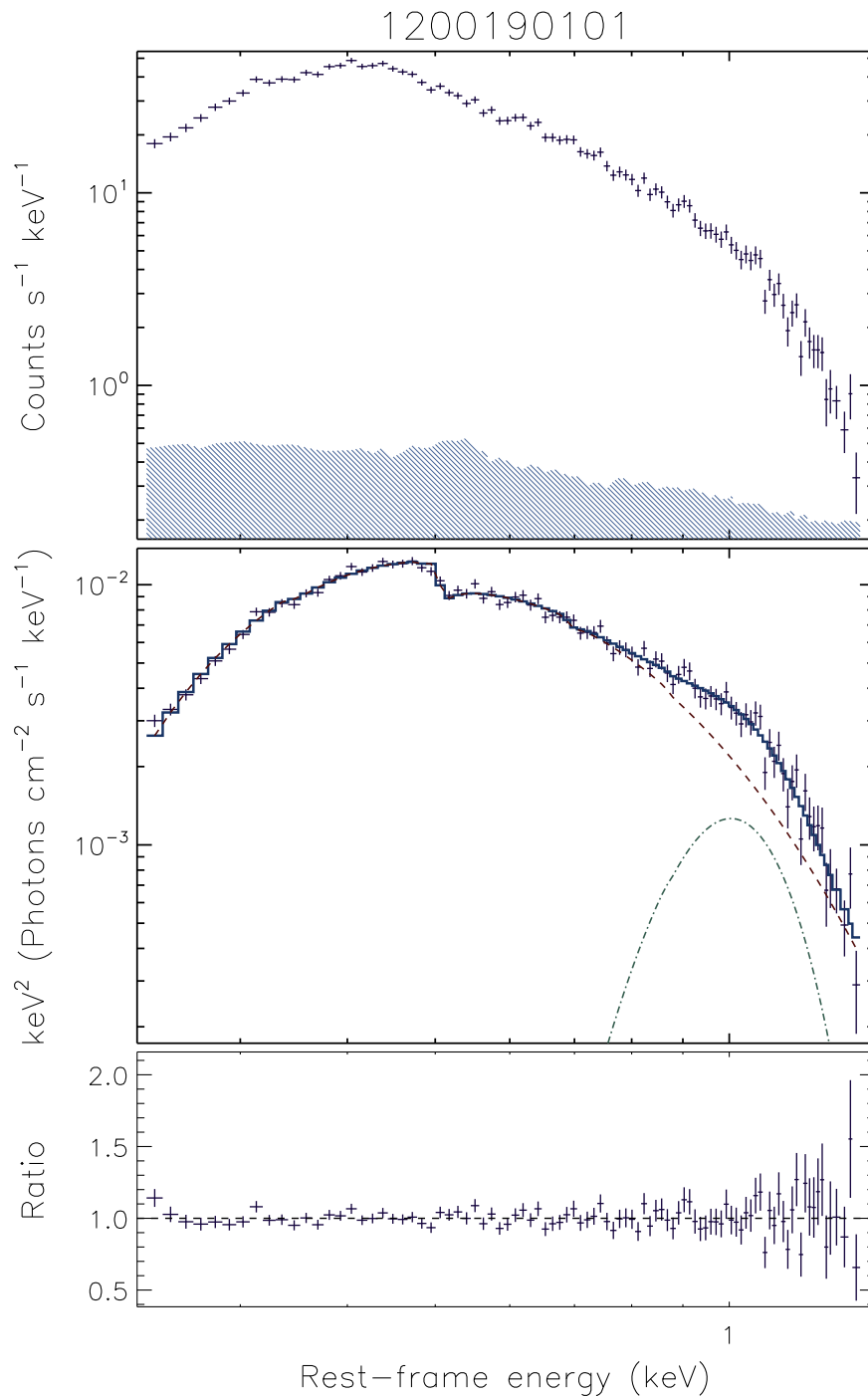
Figure L1. NICER spectrum of 1ES 1927+654 (ObsID 1200190101).

(The complete figure set (232 images) is available.)

ORCID iDs

C. Ricci ⓘ https://orcid.org/0000-0001-5231-2645
R. Remillard ⓘ https://orcid.org/0000-0003-4815-0481
B. Trakhtenbrot ⓘ https://orcid.org/0000-0002-3683-7297
I. Arcavi ⓘ https://orcid.org/0000-0001-7090-4898
K. C. Gendreau ⓘ https://orcid.org/0000-0001-7115-2819
A. C. Fabian ⓘ https://orcid.org/0000-0002-9378-4072
L. C. Ho ⓘ https://orcid.org/0000-0001-6947-5846
E. Cackett ⓘ https://orcid.org/0000-0002-8294-9281
D. Altamirano ⓘ https://orcid.org/0000-0002-3422-0074

P. Gandhi ⓘ https://orcid.org/0000-0003-3105-2615
J. Steiner ⓘ https://orcid.org/0000-0002-5872-6061
C.-H. Chan ⓘ https://orcid.org/0000-0001-5949-6109

References

Abramowicz, M. A., Czerny, B., Lasota, J. P., & Szuszkiewicz, E. 1988, ApJ, 332, 646
Ai, Y., Dou, L., Yang, C., et al. 2020, ApJ, 890, L29
Alexander, D. M., & Hickox, R. C. 2012, NewAR, 56, 93
Antonucci, R. 1993, ARA&A, 31, 473

Arnaud, K. A. 1996, in ASP Conf. Ser. 101, Astronomical Data Analysis Software and Systems V, ed. G. H. Jacoby & J. Barnes (San Francisco, CA: ASP), 17

Arzoumanian, Z., Gendreau, K. C., Baker, C. L., et al. 2014, Proc. SPIE, 9144, 914420

Baloković, M., Harrison, F. A., Madejski, G., et al. 2020, ApJ, 905, 41

Bauer, F. E., Condon, J. J., Thuan, T. X., & Broderick, J. J. 2000, ApJS, 129, 547

Bautista, M. A., & Kallman, T. R. 2001, ApJS, 134, 139

Bianchi, S., Antonucci, R., Capetti, A., et al. 2019, MNRAS, 488, L1

Bianchi, S., Guainazzi, M., Matt, G., & Fonseca Bonilla, N. 2007, A&A, 467, L19

Bianchi, S., Maiolino, R., & Risaliti, G. 2012a, AdAst, 2012, 782030

Bianchi, S., Marinucci, A., Matt, G., et al. 2017, MNRAS, 468, 2740

Bianchi, S., Panessa, F., Barcons, X., et al. 2012b, MNRAS, 426, 3225

Bisnovatyi-Kogan, G. S., Zel'dovich, Y. B., & Syunyaev, R. A. 1971, SvA, 15, 17

Blackburn, J. K. 1995, in ASP Conf. Ser. 77, Astronomical Data Analysis Software and Systems IV, ed. R. A. Shaw, H. E. Payne, & J. J. E. Hayes (San Francisco, CA: ASP), 367

Blanchard, P. K., Nicholl, M., Berger, E., et al. 2017, ApJ, 843, 106

Boissay-Malaquin, R., Danehkar, A., Marshall, H. L., & Nowak, M. A. 2019, ApJ, 873, 29

Boissay, R., Ricci, C., & Paltani, S. 2016, A&A, 588, A70

Boller, T., Tanaka, Y., Fabian, A., et al. 2003a, MNRAS, 343, L89

Boller, T., Voges, W., Dennefeld, M., et al. 2003b, A&A, 397, 557

Bonning, E. W., Cheng, L., Shields, G. A., Salviander, S., & Gebhardt, K. 2007, ApJ, 659, 211

Boorman, P. G., Gandhi, P., Baloković, M., et al. 2018, MNRAS, 477, 3775

Brightman, M., & Nandra, K. 2008, MNRAS, 390, 1241

Brightman, M., Silverman, J. D., Mainieri, V., et al. 2013, MNRAS, 433, 2485

Buchner, J., Brightman, M., Nandra, K., Nikutta, R., & Bauer, F. E. 2019, A&A, 629, A16

Burrows, D. N., Hill, J. E., Nousek, J. A., et al. 2005, SSRv, 120, 165

Cash, W. 1979, ApJ, 228, 939

Chan, C.-H., Piran, T., & Krolik, J. H. 2020, ApJ, 903, 17

Chan, C.-H., Piran, T., & Krolik, J. H. 2021, arXiv:2101.02290

Chan, C.-H., Piran, T., Krolik, J. H., & Saban, D. 2019, ApJ, 881, 113

Chiang, C.-Y., Walton, D. J., Fabian, A. C., Wilkins, D. R., & Gallo, L. C. 2015, MNRAS, 446, 759

Connolly, S. D., McHardy, I. M., Skipper, C. J., & Emmanoulopoulos, D. 2016, MNRAS, 459, 3963

Constantin, A., Green, P., Aldcroft, T., et al. 2009, ApJ, 705, 1336

Costantini, E., Kaastra, J. S., Arav, N., et al. 2007, A&A, 461, 121

Crummy, J., Fabian, A. C., Gallo, L., & Ross, R. R. 2006, MNRAS, 365, 1067

Dadina, M. 2007, A&A, 461, 1209

Dadina, M. 2008, A&A, 485, 417

Dauser, T., Garcia, J., Wilms, J., et al. 2013, MNRAS, 430, 1694

Dauser, T., Wilms, J., Reynolds, C. S., & Brenneman, L. W. 2010, MNRAS, 409, 1534

den Herder, J. W., Brinkman, A. C., Kahn, S. M., et al. 2001, A&A, 365, L7

Denney, K. D., De Rosa, G., Croxall, K., et al. 2014, ApJ, 796, 134

Dexter, J., Xin, S., Shen, Y., et al. 2019, ApJ, 885, 44

Done, C., Davis, S. W., Jin, C., Blaes, O., & Ward, M. 2012, MNRAS, 420, 1848

Edelson, R. A., Krolik, J. H., & Pike, G. F. 1990, ApJ, 359, 86

Elitzur, M., & Ho, L. C. 2009, ApJ, 701, L91

Elitzur, M., Ho, L. C., & Trump, J. R. 2014, MNRAS, 438, 3340

Elitzur, M., & Netzer, H. 2016, MNRAS, 459, 585

Elvis, M., Plummer, D., Schachter, J., & Fabbiano, G. 1992, ApJS, 80, 257

Emmanoulopoulos, D., Papadakis, I. E., McHardy, I. M., et al. 2012, MNRAS, 424, 1327

Evans, P. A., Beardmore, A. P., Page, K. L., et al. 2009, MNRAS, 397, 1177

Fabian, A. C., Iwasawa, K., Reynolds, C. S., & Young, A. J. 2000, PASP, 112, 1145

Fabian, A. C., Kara, E., Walton, D. J., et al. 2013, MNRAS, 429, 2917

Fabian, A. C., Lohfink, A., Belmont, R., Malzac, J., & Coppi, P. 2017, MNRAS, 467, 2566

Fabian, A. C., Lohfink, A., Kara, E., et al. 2015, MNRAS, 451, 4375

Fabian, A. C., Miniutti, G., Gallo, L., et al. 2004, MNRAS, 353, 1071

Fabian, A. C., Zoghbi, A., Ross, R. R., et al. 2009, Natur, 459, 540

Frederick, S., Gezari, S., Graham, M. J., et al. 2019, ApJ, 883, 31

Gabriel, C., Denby, M., Fyfe, D. J., et al. 2004, in ASP Conf. Ser. 314, Astronomical Data Analysis Software and Systems XIII, ed. F. Ochsenbein, M. G. Allen, & D. Egret (San Francisco, CA: ASP), 759

Gallo, L. C., MacMackin, C., Vasudevan, R., et al. 2013, MNRAS, 433, 421

Gallo, L. C., Tanaka, Y., Boller, T., et al. 2004, MNRAS, 353, 1064

García, J., Dauser, T., Lohfink, A., et al. 2014, ApJ, 782, 76

García, J., Dauser, T., Reynolds, C. S., et al. 2013, ApJ, 768, 146

García, J., & Kallman, T. R. 2010, ApJ, 718, 695

García, J. A., Kara, E., Walton, D., et al. 2019, ApJ, 871, 88

Gehrels, N., Chincarini, G., Giommi, P., et al. 2004, ApJ, 611, 1005

Gendreau, K. C., Arzoumanian, Z., Adkins, P. W., et al. 2016, Proc. SPIE, 9905, 99051H

Gendreau, K. C., Arzoumanian, Z., & Okajima, T. 2012, Proc. SPIE, 8443, 844313

Ghisellini, G., Maraschi, L., & Tavecchio, F. 2009, MNRAS, 396, L105

Gierliński, M., & Done, C. 2004, MNRAS, 349, L7

Gierliński, M., & Done, C. 2006, MNRAS, 371, L16

Giustini, M., Miniutti, G., & Saxton, R. D. 2020, A&A, 636, L2

Gu, M., & Cao, X. 2009, MNRAS, 399, 349

Guo, H., Peng, J., Zhang, K., et al. 2020, ApJ, 905, 52

Guo, H., Sun, M., Liu, X., et al. 2019, ApJ, 883, L44

Haardt, F., & Maraschi, L. 1991, ApJ, 380, L51

Harrison, F. A., Craig, W. W., Christensen, F. E., et al. 2013, ApJ, 770, 103

Hickox, R. C., & Alexander, D. M. 2018, ARA&A, 56, 625

Ho, L. C. 2008, ARA&A, 46, 475

Ho, L. C., Kim, M., & Terashima, Y. 2012, ApJ, 759, L16

Hon, W. J., Webster, R., & Wolf, C. 2020, MNRAS, 497, 192

Husemann, B., Urrutia, T., Tremblay, G. R., et al. 2016, A&A, 593, L9

Ichimaru, S. 1977, ApJ, 214, 840

Iwasawa, K., & Taniguchi, Y. 1993, ApJ, 413, L15

Jansen, F., Lumb, D., Altieri, B., et al. 2001, A&A, 365, L1

Kaastra, J. S. 2017, A&A, 605, A51

Kaastra, J. S., Kriss, G. A., Cappi, M., et al. 2014, Sci, 345, 64

Kaastra, J. S., Mehdipour, M., Behar, E., et al. 2018, A&A, 619, A112

Kalberla, P. M. W., Burton, W. B., Hartmann, D., et al. 2005, A&A, 440, 775

Kalemci, E., Tomsick, J. A., Rothschild, R. E., Pottschmidt, K., & Kaaret, P. 2004, ApJ, 603, 231

Kallman, T., & Bautista, M. 2001, ApJS, 133, 221

Kamraj, N., Harrison, F. A., Baloković, M., Lohfink, A., & Brightman, M. 2018, ApJ, 866, 124

Kara, E., Alston, W. N., Fabian, A. C., et al. 2016, MNRAS, 462, 511

Kara, E., García, J. A., Lohfink, A., et al. 2017, MNRAS, 468, 3489

Kara, E., Loewenstein, M., Remillard, R. A., et al. 2018, ATel, 12169

Kaspi, S., Maoz, D., Netzer, H., et al. 2005, ApJ, 629, 61

Kaspi, S., Smith, P. S., Netzer, H., et al. 2000, ApJ, 533, 631

Katebi, R., Chornock, R., Berger, E., et al. 2019, MNRAS, 487, 4057

Kawaguchi, T., Mineshige, S., Umemura, M., & Turner, E. L. 1998, ApJ, 504, 671

King, A. 2003, ApJ, 596, L27

King, A. 2020, MNRAS, 493, L120

Komossa, S. 2015, JHEAp, 7, 148

Kormendy, J., & Ho, L. C. 2013, ARA&A, 51, 511

Kosec, P., Buisson, D. J. K., Parker, M. L., et al. 2018, MNRAS, 481, 947

Koss, M., Trakhtenbrot, B., Ricci, C., et al. 2017, ApJ, 850, 74

Krawczynski, H., Hughes, S. B., Horan, D., et al. 2004, ApJ, 601, 151

Krumpe, M., Husemann, B., Tremblay, G. R., et al. 2017, A&A, 607, L9

LaMassa, S. M., Cales, S., Moran, E. C., et al. 2015, ApJ, 800, 144

Lawrence, A. 2018, NatAs, 2, 102

Lin, D., Godet, O., Ho, L. C., et al. 2017a, MNRAS, 468, 783

Lin, D., Guillochon, J., Komossa, S., et al. 2017b, NatAs, 1, 0033

Liu, Z., Li, D., Liu, H.-Y., et al. 2020, ApJ, 894, 93

Lubiński, P., Beckmann, V., Gibaud, L., et al. 2016, MNRAS, 458, 2454

MacLeod, C. L., Green, P. J., Anderson, S. F., et al. 2019, ApJ, 874, 8

MacLeod, C. L., Ivezić, Ž., Kochanek, C. S., et al. 2010, ApJ, 721, 1014

Madsen, K. K., Harrison, F. A., Markwardt, C. B., et al. 2015, ApJS, 220, 8

Magorrian, J., Tremaine, S., Richstone, D., et al. 1998, AJ, 115, 2285

Maiolino, R., Risaliti, G., Salvati, M., et al. 2010, A&A, 517, A47

Makishima, K., Maejima, Y., Mitsuda, K., et al. 1986, ApJ, 308, 635

Marinucci, A., Bianchi, S., Matt, G., et al. 2016, MNRAS, 456, L94

Marinucci, A., Bianchi, S., Nicastro, F., Matt, G., & Goulding, A. D. 2012, ApJ, 748, 130

Markowitz, A. G., Krumpe, M., & Nikutta, R. 2014, MNRAS, 439, 1403

Mason, K. O., Breeveld, A., Much, R., et al. 2001, A&A, 365, L36

Matt, G., Baloković, M., Marinucci, A., et al. 2015, MNRAS, 447, 3029

Matt, G., & Iwasawa, K. 2019, MNRAS, 482, 151

McElroy, R. E., Husemann, B., Croom, S. M., et al. 2016, A&A, 593, L8

McHardy, I. M., Cameron, D. T., Dwelly, T., et al. 2014, MNRAS, 444, 1469

Merloni, A., Dwelly, T., Salvato, M., et al. 2015, MNRAS, 452, 69

Merloni, A., & Fabian, A. C. 2001, MNRAS, 321, 549

Merloni, A., Predehl, P., Becker, W., et al. 2012, arXiv:1209.3114

Miniutti, G., Saxton, R. D., Giustini, M., et al. 2019, Natur, 573, 381
Miniutti, G., Saxton, R. D., Rodríguez-Pascual, P. M., et al. 2013, MNRAS, 433, 1764
Mitsuda, K., Inoue, H., Koyama, K., et al. 1984, PASJ, 36, 741
Mushotzky, R. F., Done, C., & Pounds, K. A. 1993, ARA&A, 31, 717
Nandra, K., & Pounds, K. A. 1994, MNRAS, 268, 405
Netzer, H. 2015, ARA&A, 53, 365
Nicastro, F. 2000, ApJ, 530, L65
Nicholls, B., Brimacombe, J., Kiyota, S., et al. 2018, ATel, 11391
Noda, H., & Done, C. 2018, MNRAS, 480, 3898
Oknyansky, V. L., Winkler, H., Tsygankov, S. S., et al. 2019, MNRAS, 483, 558
Panessa, F., & Bassani, L. 2002, A&A, 394, 435
Panessa, F., Carrera, F. J., Bianchi, S., et al. 2009, MNRAS, 398, 1951
Parker, M. L., Komossa, S., Kollatschny, W., et al. 2016, MNRAS, 461, 1927
Parker, M. L., Schartel, N., Grupe, D., et al. 2019, MNRAS, 483, L88
Perlman, E. S., Stocke, J. T., Schachter, J. F., et al. 1996, ApJS, 104, 251
Piconcelli, E., Jimenez-Bailón, E., Guainazzi, M., et al. 2005, A&A, 432, 15
Pinto, C., Middleton, M. J., & Fabian, A. C. 2016, Natur, 533, 64
Pounds, K. A., & Vaughan, S. 2011, MNRAS, 413, 1251
Ramos Almeida, C., Martínez González, M. J., Asensio Ramos, A., et al. 2016, MNRAS, 461, 1387
Ramos Almeida, C., & Ricci, C. 2017, NatAs, 1, 679
Ricci, C., Bauer, F. E., Arevalo, P., et al. 2016, ApJ, 820, 5
Ricci, C., Ho, L. C., Fabian, A. C., et al. 2018, MNRAS, 480, 1819
Ricci, C., Kara, E., Loewenstein, M., et al. 2020, ApJ, 898, L1
Ricci, C., Paltani, S., Awaki, H., et al. 2013a, A&A, 553, A29
Ricci, C., Paltani, S., Ueda, Y., & Awaki, H. 2013b, MNRAS, 435, 1840
Ricci, C., Trakhtenbrot, B., Koss, M. J., et al. 2017, ApJS, 233, 17
Ricci, C., Ueda, Y., Paltani, S., et al. 2014, MNRAS, 441, 3622
Ricci, C., Walter, R., Courvoisier, T. J. L., & Paltani, S. 2011, A&A, 532, A102
Risaliti, G., Salvati, M., Elvis, M., et al. 2009, MNRAS, 393, L1
Roming, P. W. A., Kennedy, T. E., Mason, K. O., et al. 2005, SSRv, 120, 95
Ross, N. P., Ford, K. E. S., Graham, M., et al. 2018, MNRAS, 480, 4468
Ruan, J. J., Anderson, S. F., Cales, S. L., et al. 2016, ApJ, 826, 188
Ruan, J. J., Anderson, S. F., Eracleous, M., et al. 2019a, ApJ, 883, 76
Ruan, J. J., Anderson, S. F., Eracleous, M., et al. 2019b, arXiv:1909.04676
Rumbaugh, N., Shen, Y., Morganson, E., et al. 2018, ApJ, 854, 160
Sartori, L. F., Schawinski, K., Trakhtenbrot, B., et al. 2018, MNRAS, 476, L34
Scepi, N., Begelman, M. C., & Dexter, J. 2021, MNRAS, arXiv:2011.01954
Shakura, N. I., & Sunyaev, R. A. 1973, A&A, 24, 337
Shappee, B. J., Prieto, J. L., Grupe, D., et al. 2014, ApJ, 788, 48
Shemmer, O., Brandt, W. N., Netzer, H., Maiolino, R., & Kaspi, S. 2006, ApJL, 646, L29
Sheng, Z., Wang, T., Jiang, N., et al. 2020, ApJ, 889, 46
Shi, Y., Rieke, G. H., Smith, P., et al. 2010, ApJ, 714, 115
Shu, X. W., Wang, S. S., Dou, L. M., et al. 2018, ApJ, 857, L16
Shu, X. W., Wang, T. G., Jiang, N., et al. 2017, ApJ, 837, 3
Shu, X. W., Yaqoob, T., & Wang, J. X. 2010, ApJS, 187, 581

Simcoe, R., McLeod, K. K., Schachter, J., & Elvis, M. 1997, ApJ, 489, 615
Sobolewska, M. A., & Papadakis, I. E. 2009, MNRAS, 399, 1597
Stanek, K. Z. 2018, Transient Name Server Discovery Report, 2018-287, 1
Stern, D., McKernan, B., Graham, M. J., et al. 2018, ApJ, 864, 27
Stern, J., & Laor, A. 2012, MNRAS, 423, 600
Strüder, L., Briel, U., Dennerl, K., et al. 2001, A&A, 365, L18
Sun, L., Shu, X., & Wang, T. 2013, ApJ, 768, 167
Svensson, R. 1984, MNRAS, 209, 175
Terashima, Y., Kamizasa, N., Awaki, H., Kubota, A., & Ueda, Y. 2012, ApJ, 752, 154
Timlin, J. D., Brandt, W. N., I., Zhu, S., et al. 2020, MNRAS, 498, 4033
Titarchuk, L. 1994, ApJ, 434, 570
Tombesi, F., Cappi, M., Reeves, J. N., et al. 2010, A&A, 521, A57
Tonry, J. L., Denneau, L., Heinze, A. N., et al. 2018, PASP, 130, 064505
Tortosa, A., Bianchi, S., Marinucci, A., Matt, G., & Petrucci, P. O. 2018, A&A, 614, A37
Tortosa, A., Marinucci, A., Matt, G., et al. 2017, MNRAS, 466, 4193
Trakhtenbrot, B., Arcavi, I., MacLeod, C. L., et al. 2019a, ApJ, 883, 94
Trakhtenbrot, B., Arcavi, I., Ricci, C., et al. 2019b, NatAs, 3, 242
Trakhtenbrot, B., Netzer, H., Lira, P., & Shemmer, O. 2011, ApJ, 730, 7
Trakhtenbrot, B., Ricci, C., Koss, M. J., et al. 2017, MNRAS, 470, 800
Tran, H. D. 2001, ApJ, 554, L19
Tran, H. D. 2003, ApJ, 583, 632
Tran, H. D., Lyke, J. E., & Mader, J. A. 2011, ApJ, 726, L21
Turner, M. J. L., Abbey, A., Arnaud, M., et al. 2001, A&A, 365, L27
Urry, C. M., & Padovani, P. 1995, PASP, 107, 803
Vasudevan, R. V., & Fabian, A. C. 2007, MNRAS, 381, 1235
Vasudevan, R. V., & Fabian, A. C. 2009, MNRAS, 392, 1124
Vaughan, S., Edelson, R., Warwick, R. S., & Uttley, P. 2003, MNRAS, 345, 1271
Voges, W., Aschenbach, B., Boller, T., et al. 1999, A&A, 349, 389
Volonteri, M. 2012, Sci, 337, 544
Walton, D. J., Middleton, M. J., Pinto, C., et al. 2016, ApJ, 826, L26
Walton, D. J., Nardini, E., Fabian, A. C., Gallo, L. C., & Reis, R. C. 2013, MNRAS, 428, 2901
Walton, D. J., Nardini, E., Gallo, L. C., et al. 2019, MNRAS, 484, 2544
Wang, J., Xu, D. W., & Wei, J. Y. 2020, ApJ, 901, 1
Wilms, J., Allen, A., & McCray, R. 2000, ApJ, 542, 914
Winter, L. M., Mushotzky, R. F., Reynolds, C. S., & Tueller, J. 2009, ApJ, 690, 1322
Wu, Q., & Gu, M. 2008, ApJ, 682, 212
Yamaoka, K., Uzawa, M., Arai, M., Yamazaki, T., & Yoshida, A. 2005, ChJAS, 5, 273
Yan, L., Wang, T., Jiang, N., et al. 2019, ApJ, 874, 44
Yang, Q., Wu, X.-B., Fan, X., et al. 2018, ApJ, 862, 109
Younes, G., Porquet, D., Sabra, B., & Reeves, J. N. 2011, A&A, 530, A149
Yuan, F., & Narayan, R. 2014, ARA&A, 52, 529
Yuan, F., Taam, R. E., Misra, R., Wu, X.-B., & Xue, Y. 2007, ApJ, 658, 282
Yuan, W., Zhang, C., Feng, H., et al. 2015, arXiv:1506.07735
Zdziarski, A. A., Johnson, W. N., & Magdziarz, P. 1996, MNRAS, 283, 193
Życki, P. T., Done, C., & Smith, D. A. 1999, MNRAS, 309, 561